

Structural and Surface Modifications of Nanomaterials for Energy Applications

Filip Ambroz

Department of Chemistry

University College London

Thesis submitted for the degree of Engineering Doctorate

2021

Declaration

I, Filip Ambroz, confirm that the work presented in this thesis is my own. Where information has been derived from other sources, I confirm that this has been indicated in the thesis.

Abstract

While renewable energy systems are currently on the rise, there are many projections stating that fossil fuels will still remain the dominant energy source for the next few decades. In order for the energy transition to take place promptly, the cost of generating energy from renewable sources has to be in line or lower compared to fossil fuels. Of the renewable energy alternatives that are available, solar energy is by far the most abundant and widely distributed source of energy generation. However, this type of energy is intermittent and has to be combined with energy storage technology, which has, in the last decade, developed significantly.

In this thesis, research has focused on materials modification, synthesis, and utilization for solar cells. At first, TiO₂ 1D (one-dimensional) nanomaterials were synthesized, which are n-type materials, typically used for charge transportation (electron extraction) in a solar device configuration. Properties of these nanomaterials were modified by the addition of <12 nm gold nanoparticles (NPs), which can further improve energy conversion efficiency. The choice of using NPs for TiO₂ modification was additionally expanded towards lanthanum and lithium metal ions, which were separately combined for the creation of a composite material. Characterisation was then performed using techniques that are widely employed for materials science research. In addition, nanomaterials were implemented for solar devices, and two different types were fabricated: dye-sensitized, and perovskite solar cells. Finally, research was expanded towards the synthesis of perovskite nanocrystals, which were produced using a novel, low energy, and scalable approach.

In this thesis, challenges in the field of photovoltaics are addressed by exploiting the field of nanotechnology, with the aim to improve the performance of solar cells.

Impact Statement

This thesis focuses on the synthesis and characterisation of different types of nanomaterials that can be implemented in various applications, particularly for photovoltaics and light display technology. In the former case, conversion efficiency of the solar energy into electricity, renders how viable the technology is for commercialisation. Therefore, research efforts have been devoted towards obtaining low cost and high performing solar devices. There are many projections claiming that in near future, solar technology will lead renewable surge and transition of the energy generation market. For that to occur, it is a prerequisite to develop more competitive photovoltaic cells that would enable low carbon economy. In this research, nanotechnology has been implemented to advance the development of solar cells with the aim to improve their light conversion efficiency. Consequently, various types of composite nanomaterials were synthesized and used within the solar cell configuration. Research was also expanded towards developing novel and sustainable synthesis pathways of nanomaterials, that find their application not only in solar cells, but also for light-emitting technology.

Acknowledgements

I would like to thank my primary supervisor Prof. Ivan Parkin for giving me the opportunity to join his research group at University College London as an engineering doctorate student. Ivan has been very supportive throughout my doctorate and has prepared me well for my future career. I am grateful for the guidance he has provided and the research freedom that was given to me.

In addition, I would like to thank my co-supervisor Dr. Thomas Macdonald for his support, dedication, and mentoring throughout this project. He has been a very important part of the research work and I appreciate everything he has taught me.

Surface Measurement Systems Ltd. have played a substantial role during my research and I am grateful for their funding, resources, and expertise.

Finally, I must thank my family and my partner Ingrid for their support during these four years of incredible experience in London.

List of Symbols and Abbreviations

1D – One-Dimensional

AM – Air Mass

ATR – Attenuated Total Reflection

BET – Brunauer–Emmett–Teller

CB – Conduction Band

CIE – Commission on Illumination

CIGS – Copper Indium Gallium Selenide

CNTs – Carbon Nanotubes

Con-CsPbBr₃ – Control Caesium Lead Tribromide

Con-FAPbBr₃ – Control Formamidinium Lead Tribromide

DiOPA – Diisooctylphosphinic Acid

DSSCs – Dye-Sensitized Solar Cells

DMF – Dimethylformamide

DMPII – 1-propyl-2,3-dimethylimidazolium iodide

E_a – Solvent - Toluene (fluorescence emission data)

E_c – QDNC Solution (scattering data)

E_F – Fermi Level

EQE – External Quantum Efficiency

FA – Formamidinium (CH(NH₂)₂⁺) ion

FF – Fill Factor

FTIR – Fourier-Transform Infrared Spectroscopy

FTO – Fluorine Doped Tin Oxide

FWHM – Full Width at Half Maximum

HR – High-Resolution

ICSD – Inorganic Crystal Structure Database

IPCE – Incident Photon-to-Electron Conversion Efficiency

ITU – International Telecommunication Union

I-V – Current-Voltage

JPCDS – Joint Committee on Powder Diffraction Standards

J_{sc} – Short-Circuit Current Density

J-V – Current Density-Voltage

LARP – Ligand-Assisted Reprecipitation Approach

Li-TFSI – Lithium bis(trifluoromethanesulfonyl)imide

L_b – Solvent - Toluene (scattering data)

L_c – QDNC Solution (scattering data)

LEDs – Light-Emitting Diodes

LSPR – Localized Surface Plasmon Resonance

MA – Methylammonium (CH₃NH₃⁺) ion

N719 – Di-tetrabutylammonium cis-bis(isothiocyanato)bis(2,2'-bipyridyl-4,4'
dicarboxylato)ruthenium(II)

NFs – Nanofibers

NPs – Nanoparticles

NREL – National Renewable Energy Laboratory

P25 – Titanium Dioxide Nanopowder

PCE – Power Conversion Efficiency

PLQY – Photoluminescence Quantum Yield

PSCs – Perovskite Solar Cells

PTAA – poly[bis(4-phenyl)(2,4,6-trimethylphenyl)amine]

PVP – 1-ethenylpyrrolidin-2-one

QDNCs – Quantum Dot Nanocrystals

Rec. 2020 – Recommendation

RPM – Rotations per Minute

R_S – Series Resistance

R_{SH} – Shunt Resistance

RT – Room Temperature

RT-CsPbBr₃ – Room Temperature Caesium Lead Tribromide

RT-FAPbBr₃ – Room Temperature Formamidinium Lead Tribromide

SAED – Selected Area Electron Diffraction

SEM – Scanning Electron Microscope

STP – Standard Temperature and Pressure

TBP – 4-tert-Butylpyridine

TEM – Transmission Electron Microscope

TGA – Thermogravimetric Analysis

TOPO – Trioctylphosphine Oxide

UK – United Kingdom

V_{FB} – Flat-Band Potential

V_{OC} – Open-Circuit Voltage

XPS – X-ray Photoelectron Spectroscopy

XRD – X-ray Powder Diffraction

γ – Out-of-Plane Deformation

δ – In-Plane Deformation

λ – Wavelength

ν – Stretching

ν_{as} – Asymmetric Stretching

ν_s – Symmetric Stretching

σ – Size Deviation

Publications

Portnoi, M.; Haigh, P. A.; Macdonald, T. J.; Ambroz, F.; Parkin, I. P.; Darwazeh, I.; Papakonstantinou, I. Bandwidth Limits of Luminescent Solar Concentrators as Detectors in Free-Space Optical Communication Systems. *Light Sci. Appl.* **2021**, *10*, 3.

Zhang, Y.; Kirs, A.; Ambroz, F.; Lin, C.-T.; Bati, A. S. R.; Parkin, I. P.; Shapter, J. G.; Batmunkh, M.; Macdonald, T. J. Ambient Fabrication of Organic–Inorganic Hybrid Perovskite Solar Cells. *Small Methods* **2021**, *5*, 2000744.

Ambroz, F.; Xu, W.; Gadipelli, S.; Brett, D. J. L.; Lin, C.-T.; Contini, C.; McLachlan, M. A.; Durrant, J. R.; Parkin, I. P.; Macdonald, T. J. Room Temperature Synthesis of Phosphine-Capped Lead Bromide Perovskite Nanocrystals without Coordinating Solvents. *Part. Part. Syst. Charact.* **2020**, *37*, 1900391.

Macdonald, T. J.; Batmunkh, M.; Lin, C.-T.; Kim, J.; Tune, D. D.; Ambroz, F.; Li, X.; Xu, S.; Sol, C.; Papakonstantinou, I.; McLachlan, M. A.; Parkin, I. P.; Shapter, J. G.; Durrant, J. R. Origin of Performance Enhancement in TiO₂-Carbon Nanotube Composite Perovskite Solar Cells. *Small Methods* **2019**, *3*, 1900164.

Ambroz, F.; Donnelly, J. L.; Wilden, J. D.; Macdonald, T. J.; Parkin, I. P. Carboxylic Acid Functionalization at the Meso-Position of the Bodipy Core and Its Influence on Photovoltaic Performance. *Nanomaterials* **2019**, *9*, 1346.

Ambroz, F.; Sathasivam, S.; Lee, R.; Gadipelli, S.; Lin, C.-T.; Xu, S.; Poduval, R. K.; McLachlan, M. A.; Papakonstantinou, I.; Parkin, I. P.; Macdonald, T. J. Influence of Lithium and Lanthanum Treatment on TiO₂ Nanofibers and Their Application in N-i-p Solar Cells. *ChemElectroChem* **2019**, *6*, 3590–3598.

Ambroz, F.; Macdonald, T. J.; Martis, V.; Parkin, I. P. Evaluation of the BET Theory for the Characterization of Meso and Microporous MOFs. *Small Methods* **2018**, *2*, 1800173.

Macdonald, T. J.; Ambroz, F.; Batmunkh, M.; Li, Y.; Kim, D.; Contini, C.; Poduval, R.; Liu, H.; Shapter, J. G.; Papakonstantinou, I.; Parkin, I. P. TiO₂ Nanofiber Photoelectrochemical Cells Loaded with Sub-12 Nm AuNPs: Size Dependent Performance Evaluation. *Mater. Today Energy* **2018**, *9*, 254–263.

Contents

1. Introduction.....	20
1.1 Opening Remarks	20
1.2 Energy transition from fossil fuels to renewables	20
1.3 Solar Energy Conversion	25
1.3.1 Overcoming the Challenges.....	29
1.4 Nanomaterials for Solar Cells Applications	32
1.4.1 Nanoarchitectures.....	33
1.4.2 Quantum dot nanocrystals	34
1.5 Nanomaterials and Solar Cell Characterisation.....	35
1.6 Aim of this work.....	39
2. The influence of different-sized gold NPs on dye-sensitized solar cells....	42
2.1 Introduction	42
2.2 Experimental Section	47
2.2.1 Synthesis and growth of gold NPs	47
2.2.2 Preparation of TiO ₂ NFs.....	48
2.2.3 Preparation of TiO ₂ NF photoelectrodes	48
2.2.4 Fabrication of dye-sensitized solar cells	50
2.2.5 Details of instrumentation used.....	50
2.2.6 Photovoltaic characterisation	51

2.3	Results and Discussion	52
2.3.1	Materials characterisation	52
2.3.2	Photovoltaic characterisation	60
2.4	Conclusion	68
3.	The influence of lithium and lanthanum on the performance of n-i-p solar cells	70
3.1	Introduction	70
3.2	Experimental section.....	73
3.2.1	Preparation of TiO ₂ NF precursor solutions	74
3.2.2	Preparation of TiO ₂ NF photoelectrodes	74
3.2.3	Fabrication of perovskite solar cells.....	75
3.2.4	Details of instrumentation used.....	76
3.3	Results and discussion	77
3.3.1	Materials characterisation.....	77
3.3.2	Photovoltaic characterisation	89
3.4	Conclusion	102
4.	Room temperature synthesis of perovskite nanocrystals via phosphine-based chemistry	105
4.1	Introduction	105
4.2	Experimental section.....	108
4.2.1	Synthesis of RT-FAPbBr ₃ quantum dot nanocrystals	109
4.2.2	Synthesis of Con-FAPbBr ₃ quantum dot nanocrystals.....	109

4.2.3	Synthesis of RT-CsPbBr ₃ quantum dot nanocrystals.....	110
4.2.4	Synthesis of Con-CsPbBr ₃ quantum dot nanocrystals.....	111
4.2.5	Details of instrumentation used	112
4.3	Results and discussion	114
4.3.1	Synthesis of quantum dot nanocrystals and their characteristics	114
4.3.2	Optical characteristics of quantum dot nanocrystals.....	118
4.3.3	Composition and ligand binding of quantum dot nanocrystals.....	125
4.3.4	Interactions between quantum dot nanocrystals and their ligands	130
4.4	Conclusion	140
5.	Conclusion.....	142
5.1	Summary of results	142
5.2	Novel findings	147
5.3	Future outlooks	149
6.	Bibliography	151
7.	Supporting Information	157

List of Figures

1.1. Total energy consumption (as percentage) for types of energy sources.	23
1.2. Total energy consumption (in exajoules) for types of energy sources.....	24
1.3. NREL chart of the highest performing solar cells	26
1.4. The electromagnetic spectrum showing all classes of frequencies.	28
1.5. The comparison in terms of charge transport ability of NPs and NFs.....	34
1.6. Six typical BET isotherms.....	38
2.1. (a) UV/Vis spectrum of solutions of gold NPs together with a N719 dye. (b) HR-TEM images of gold NPs.....	53
2.2. TEM images used for the size analysis of gold NPs.....	53
2.3. (a) Cross-sectional SEM image of a photoelectrode. (b) HR-SEM image of TiO ₂ NFs with added gold NPs. (c) TEM image of a TiO ₂ photoelectrode.....	55
2.4. XPS spectra for (a) Ti 2p and (b) Au 4f. (c) XRD patterns for photoelectrodes..	58
2.5. (a) UV/Vis spectra for photoelectrodes. (b) Tauc plot together with band gap values. (c) Raman spectra for photoelectrodes.....	60
2.6. (a) J-V results for control and gold NPs containing DSSCs. (b) EQE spectra of control and gold NPs containing DSSCs.	63
2.7. The values for (a) J _{sc} , (b) V _{oc} , (c) FF and (d) PCE of fabricated DSSCs.	64
3.1. Top-view SEM of (a) control, (c) lanthanum treated and (e) lithium treated TiO ₂ NFs. HR-SEM of (b) control, (d) lanthanum treated and (f) lithium treated TiO ₂ NFs with HR-TEM insets.....	78
3.2. A SAED pattern for TiO ₂ NFs.	79

3.3. Ti 2p XPS spectra for (a) control, (b) lanthanum and (c) lithium treated TiO ₂ NFs. (d) lanthanum 3d spectrum for lanthanum treated TiO ₂ NFs. (e) lithium 1s spectra for lithium treated TiO ₂ NFs.	81
3.4. (a) XRD patterns for lithium, lanthanum and control TiO ₂ NFs. (b) Raman spectra for lithium, lanthanum and control TiO ₂ NFs.....	85
3.5. Graph showing the UV/Vis spectrum of (a) control, lanthanum and lithium treated TiO ₂ NF photoelectrodes together with Tauc plots as inset. (b) The same results as under (a) for TiO ₂ NF powders.....	86
3.6. Nitrogen adsorption isotherms for control, lanthanum and lithium treated TiO ₂ NFs.....	88
3.7. An illustration of a DSSC.....	89
3.8. Cross-section SEM images of (a) a DSSC and (b) a PSC.....	90
3.9. Control, lithium treated and lanthanum treated TiO ₂ NF based DSSCs.....	94
3.10. SEM images showing surface characteristics for control TiO ₂ NFs.....	96
3.11. SEM image of control TiO ₂ NFs.....	96
3.12. Control, lithium treated and lanthanum treated TiO ₂ NF based PSC.....	98
3.13. A TiO ₂ NP based PSC.....	100
3.14. Structural formula of a TFSI anion.....	101
4.1. TEM images of RT-CsPbBr ₃ QDNCs. (a, b) Top-view. (c) HR-TEM image showing the separation between lattice planes in a cube structure.....	116
4.2. TEM images of RT-FAPbBr ₃ QDNCs. (a, b) Top-view. (c) HR-TEM image showing the separation between lattice planes in a cube structure.....	117
4.3. XRD patterns for (a) RT-FAPbBr ₃ and RT-CsPbBr ₃ QDNCs. (b) con-FAPbBr ₃ and con-CsPbBr ₃ QDNCs.....	118
4.4. UV/Vis and PL characteristics of (a) RT-FAPbBr ₃ and (b) CsPbBr ₃ QDNCs...	119

4.5. PL spectra for (a) FAPbBr ₃ and (b) CsPbBr ₃ QDNCs.....	120
4.6. Trends in PLQYs as a function of the synthesis temperatures for (a) FAPbBr ₃ and (b) CsPbBr ₃ QDNCs.....	121
4.7. Photographs of (a, c) FAPbBr ₃ and (b, d) CsPbBr ₃ QDNCs synthesized at different reaction temperatures.....	122
4.8. PLQYs as a function of the concentration of the formamidinium acetate precursor solution for FAPbBr ₃ QDNCs.....	123
4.9. PL emission lifetimes for solutions of (a) FAPbBr ₃ and (b) CsPbBr ₃ QDNCs...	124
4.10. High-resolution XPS spectra of elements (a) N 1s, (b) C 1s, (c) Pb 4f and (d) Br 3rd that were identified on the surface of RT-FAPbBr ₃ QDNCs.	126
4.11. High-resolution XPS spectra of elements (a) Cs 3d, (b) C 1s, (c) Pb 4f and (d) Br 3rd that were identified on the surface of RT-CsPbBr ₃ QDNCs.	126
4.12. High-resolution XPS spectra of elements (a) P 2p, (b) O 1s for RT-FAPbBr ₃ and (c) P 2p, (d) O 1s for RT-CsPbBr ₃ QDNCs.....	128
4.13. Atomic ratios of (a) N/Pb and (b) Br/Pb for RT-FAPbBr ₃ QDNCs.....	129
4.14. Br:Pb atomic ratios for RT-CsPbBr ₃ QDNCs.....	129
4.15. Structures of (a) DiOPA and (b) TOPO molecules.	130
4.16. FTIR spectra for TOPO.....	131
4.17. FTIR spectra for DiOPA	131
4.18. FTIR spectra for RT-CsPbBr ₃ and RT-FAPbBr ₃ QDNCs in the wavelength range between 4000 – 500 cm ⁻¹	133
4.19.46 FTIR spectra for RT-CsPbBr ₃ and RT-FAPbBr ₃ QDNCs in the wavelength range between 3000 – 2800 cm ⁻¹	135
4.20. A structural formula for the formamidinium cation.	136

4.21. FTIR spectra for RT-CsPbBr ₃ and RT-FAPbBr ₃ QDNCs in the wavelength range between 4000 – 500 cm ⁻¹ after the purification treatment	137
4.22. FTIR spectra for RT-CsPbBr ₃ QDNCs that were not subject to purification and the spectra of QDNCs that were purified.....	138
4.23. TGA graphs for purified (a) con-FAPbBr ₃ and RT-FAPbBr ₃ QDNCs, together with (b) con-CsPbBr ₃ and RT-CsPbBr ₃ QDNCs.	139
SI1. Inset of the Raman spectra between 390 - 520 cm ⁻¹ for lithium and control TiO ₂ NFs.....	157

List of Tables

2.1 Photovoltaic parameters for the highest performing DSSCs..	63
2.2 Average R _{SH} and R _S for different types of DSSCs.....	66
3.1 The values of lattice parameters and volumes for control, lanthanum and lithium treated TiO ₂ NFs.	84
3.2. Band gap for control, lanthanum and lithium treated TiO ₂ NF photoelectrodes and powders.....	87
3.3. The BET surface area and porosity for different types of TiO ₂ NFs.....	89
3.4. Dye absorption results for control, lanthanum and lithium treated TiO ₂ NFs....	91
3.5. Photovoltaic parameters for the highest performing DSSCs	93
3.6. Average solar cell parameters for 5 separate batches of DSSCs.	93
3.7. Mean R _{SH} and R _S for control, lanthanum treated, and lithium treated TiO ₂ NF based DSSCs.....	95
3.8. Photovoltaic parameters for the highest performing PSCs.....	98
3.9. Average solar cell parameters for 5 separate batches of PSCs	98

3.10. Average R_{SH} and R_S for control, lanthanum treated, and lithium treated TiO_2 NF based PSCs.....	99
4.1. Time-resolved PL results for colloids of RT QDNCs.....	125
4.2. Time-resolved PL results for colloids of control QDNCs.....	125
4.3. FTIR characteristic absorption peaks from the spectrum of TOPO	132
4.4. FTIR characteristic absorption peaks from the spectrum of DiOPA..	132

List of Schemes

Scheme 1. Schematic depiction of a TiO_2 photoelectrode used for DSSCs.	46
---	----

Chapter 1

Introduction

1. Introduction

1.1 Opening Remarks

In the last decade, research on solar energy generation has grown significantly. This was mainly as a result of the discovery of a new light absorbing material (perovskite), which has revolutionized the field. Following the implementation of a perovskite material for solar cells, the variety of applications that use it successfully, has expanded tremendously. In light of their unique characteristics, perovskites have become a focal point in nanotechnology, and research is mostly targeted at their nanocrystal (quantum dot) form. While they exhibit outstanding performance metrics, there are still issues that need to be addressed before the technology can play a major role on the market.

This thesis presents research work on improving the efficiency of solar cells, followed by materials synthesis that can be used for optoelectronic applications. Solar devices and materials characterization are discussed, and a range of different techniques implemented.

1.2 Energy transition from fossil fuels to renewables

During the past century, energy systems were built on generating energy from fossil fuels. While renewables are becoming increasingly more important, there are projections that until 2050, the majority of energy will still be obtained by fossil fuel combustion.^[1] These type of fuels are non-renewable and the cost of extraction is increasing; consequently, their price is predicted to rise.^[2] The established

infrastructure worldwide is based on fossil fuels, which makes it challenging for other technologies to compete or to replace them. Since it is a prerequisite to decrease the greenhouse gas emissions in order to meet with the targets of the Paris agreement,^[3] policy makers must provide their support in accelerating the transition of society into more sustainable future. Approaches such as the elimination of import tariffs, on the technical components that are required for power generation of renewables, will help alternative technologies to be more competitive.

When price analysis between fossil fuels and renewables is being performed, the comparisons are typically misleading. Calculations involving the cost of the energy generated from fossil fuels, do not include factors such as environmental pollution and their negative effects (including the cost perspective), which results in deceptive conclusions and a wrong impression regarding how cheap such energy is.^[4] Therefore, to have fair comparisons in the pricing scheme, all factors should be accounted for.

Other elements that make the competition unfair, are government subsidies for fossil fuels; for instance, in the United Kingdom (UK) where subsidies are one of the highest in Europe.^[5] Consequently, this results in measures that deter investments in improving energy efficiency and renewables. Hence, fossil fuel subsidies should be eliminated, and environmental effects considered in the pricing scheme, in order for renewable energy sources to be more competitive. Unfortunately, as the current global economy relies too much on fossil fuels, a strong political determination is necessary for changes to take place. Many countries have changed their approaches to solve the issue by providing financial support to renewable energy companies.^[4] Consequently, green technology has exhibited growth in the last few decades; however integrating the technology into the electrical grid and replacing fossil fuels is more challenging.

In recent years, there have been reports released about the transition from fossil fuels,^[6] but these reports may be misleading: although there was a decline in coal consumption and the greenhouse emissions did not increase, this does not necessarily imply an energy transition to renewables is taking place. The transformation in energy production occurs when energy generation from a new energy source replaces the previous methods. If a new source is simply added to the whole production to cover the expansion in energy consumption, this does not constitute a transition. Over the last decade, energy generated from renewables did not replace fossil fuel combustion, but instead served as an energy addition to the total increase in energy consumption.^[6] The production of energy from non-renewable established sources did not decrease, but remained stable (Figure 1.1). It should be noted that in Figure 1.1, energy generated from solar or wind sources are not illustrated, since the combined share was so low, i.e. 2% (in year 2017).^[6] Despite recent expansion of the solar and wind energy sectors, the total energy contribution worldwide is almost negligible.

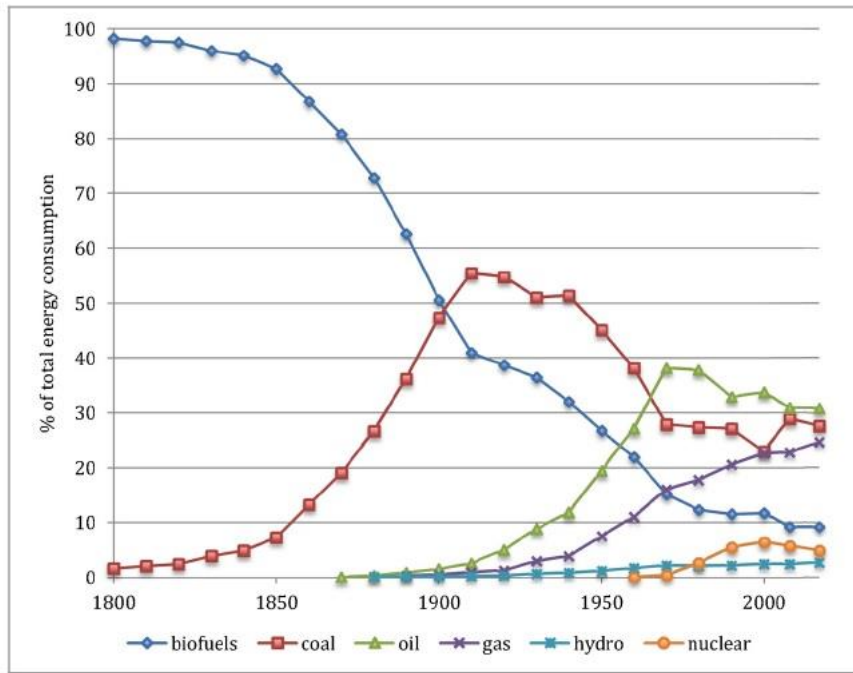


Figure 1.1. Total energy consumption (as percentage) for various types of energy sources. Reproduced with permission.^[6] Copyright 2019, Elsevier.

Figure 1.2 shows energy consumption as a quantity per source. It can be seen that none of the fossil fuel sources underwent any decrease in consumption, despite the appearance of the new ones (nuclear). In fact, all sources both fossil fuel and renewable have steadily grown over years and can therefore be considered as additions (rather than transitions), from the established technologies. Hence, new energy sources have enabled a higher total energy consumption without in any way replacing the non-renewable sources. While there can be many reasons why different energy sources struggle to compete with each other, the evident constant growth can be mostly explained by our current system, which is driven by everlasting economic expansion and the pursuit of profit, and where environmental issues are of a secondary nature.

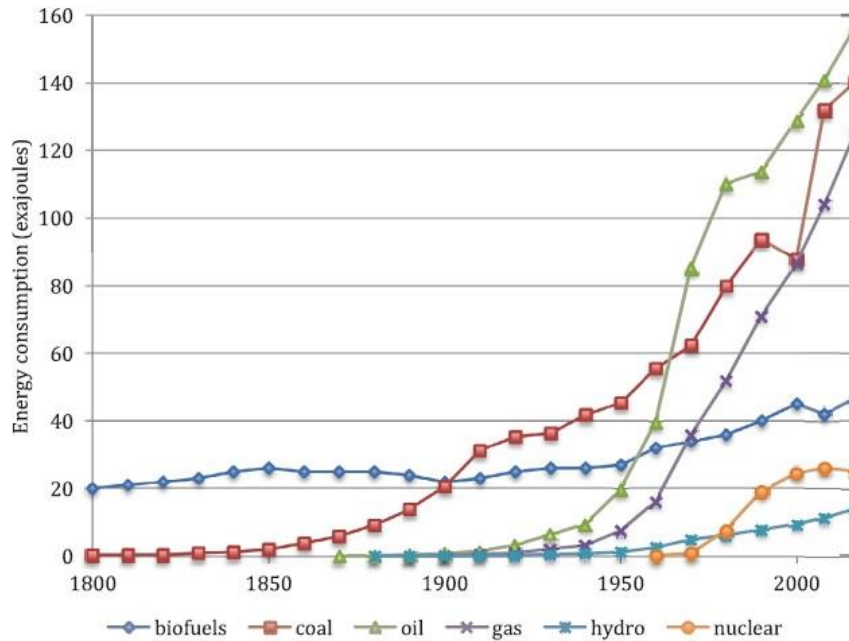


Figure 1.2. Total energy consumption (in exajoules) for various types of energy sources. Reproduced with permission.^[6] Copyright 2019, Elsevier.

Reports claiming the existence of energy transition are not only deceptive but can be harmful, since they provide the false impression that fossil fuels are in decline and we are moving towards a sustainable future. This is incorrect.

There are many studies on how the dominance of fossil fuels can be threatened. For example, an effective approach can be the reduction of tariffs on renewables, as reported by Zeidan et al.^[7] Specifically, the elimination of tariffs on technological components such as cylindrical roller bearings in wind turbines can be essential for the wind industry to compete with fossil fuels. If such approaches can expand towards all types of renewable technologies, a significant price reduction could result, which is a requirement for a potential shift in energy production. Nevertheless, reducing the price of renewables does not necessarily mean that green energy technologies will automatically replace the current technologies. There can be side effects that are difficult to predict, because the global economy is based on oil consumption and trade

where disruptions can result in economic crisis or recession. Furthermore, many economies were established on trading crude oil, and such countries will fight against any transitions as this could notably influence their economic power. Transitions should therefore start with the countries that have the biggest influence on the global economy. Strategies should include a combination of tariff reductions, elimination of fossil fuel subsidies, and research investments into the areas that could make the biggest impact worldwide. Overall, the long-term cost of climate change will be higher than the current transition into the sustainable future.

1.3 Solar Energy Conversion

Sunlight can be converted into electricity with the use of solar cells. During the last few decades, this technology has exhibited major growth as a potential replacement for the use of fossil fuels. However, compared to other alternative technologies, sunlight electricity conversion is relatively novel and was first demonstrated around 60 years ago.^[8] Initially, the technology was used for space applications, as the industry required an independent energy source for satellites. These first solar cells were very expensive, and as such, only suitable for a niche market of space investigations. The first turning point for the technology occurred in the 1970s with the oil crisis, which fueled research into alternative energy sources. Consequently, solar energy conversion became focus of investigations for terrestrial energy generation. The advantages for the implementation of solar cells, for instance, power generation in remote areas, were quickly recognized and the photovoltaic industry became increasingly more popular.

Next, came the emergence of applications where solar cells were commercially used, for example, in calculators and watches, followed by interest in large-scale power generation. In the 1980's, the industry exhibited significant advances as silicon solar cell efficiencies increased rapidly, up to 20%.^[9] While such values were demonstrated for laboratory scale devices, larger active areas were less efficient. Over the next few decades, research was aimed towards improving the efficiencies of larger panels and eventually large-scale devices were brought to the market with efficiencies ranging between 15 – 20%. Over time, other types of solar cells were also subject to technological advances, as illustrated in Figure 1.3.

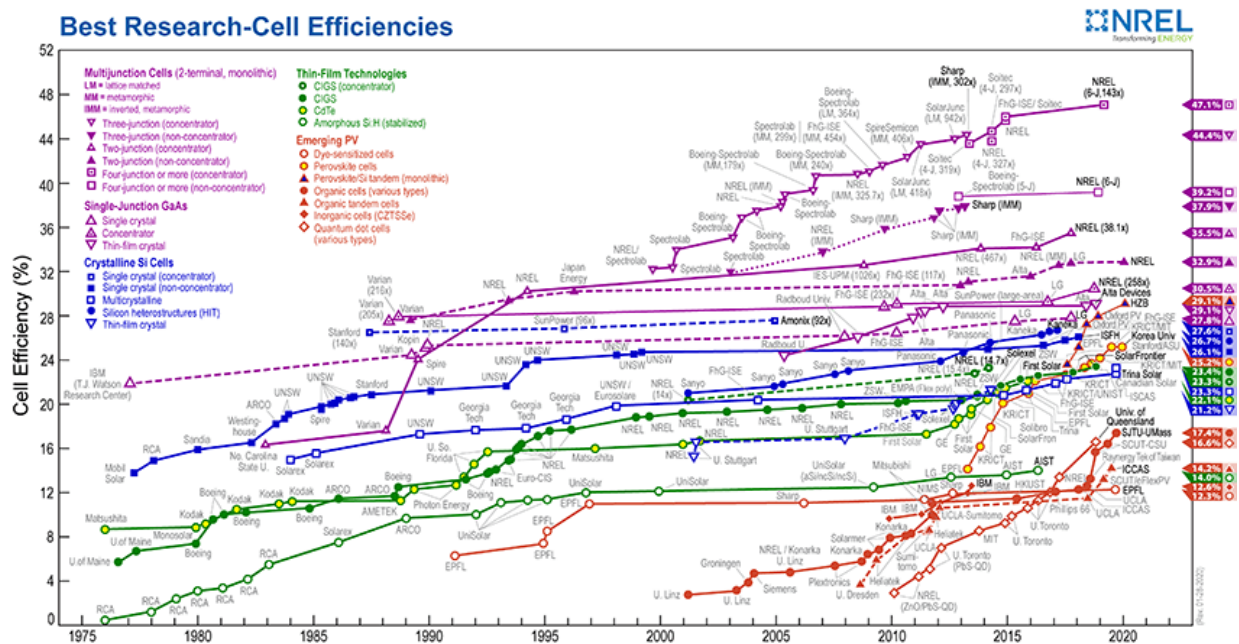


Figure 1.3. NREL chart of the highest performing solar cells between 1975 and 2020 for different types of photovoltaic technologies. Figure courtesy of NREL, Colorado, USA.

Technological advances in the photovoltaic industry made the technology feasible for commercialisation, and new markets emerged, resulting in more applications that are powered by the sunlight than ever before.^[10] The range of applications powered by

solar cells is vast, from low energy solar calculators to solar power stations that can produce several megawatts of energy.

Energy from the sun is the largest energy source available on Earth and could cover a whole year's energy consumption in one hour.^[11] While the total reserves of oil on Earth total 1.7×10^{22} Joules of energy, the sun supplies the same quantity of energy in less than a week.^[12] The majority of this energy cannot be harnessed, and the amount that can be used is only relevant if it is converted into electricity or usable heat. For this, the most critical parameters are the efficiency of a solar cell and the ability to supply the energy at low cost.

There are many factors that influence the efficiency of a solar cell, however one of the most important parameters is related to the ability of a material to absorb light. The electromagnetic spectrum (Figure 1.4) consists of three main regions of radiation, namely:

- Ultraviolet ($10 \text{ nm} < \lambda < 400 \text{ nm}$)
- Visible ($400 \text{ nm} < \lambda < 700 \text{ nm}$)
- Infrared ($700 \text{ nm} < \lambda < 1 \text{ mm}$).

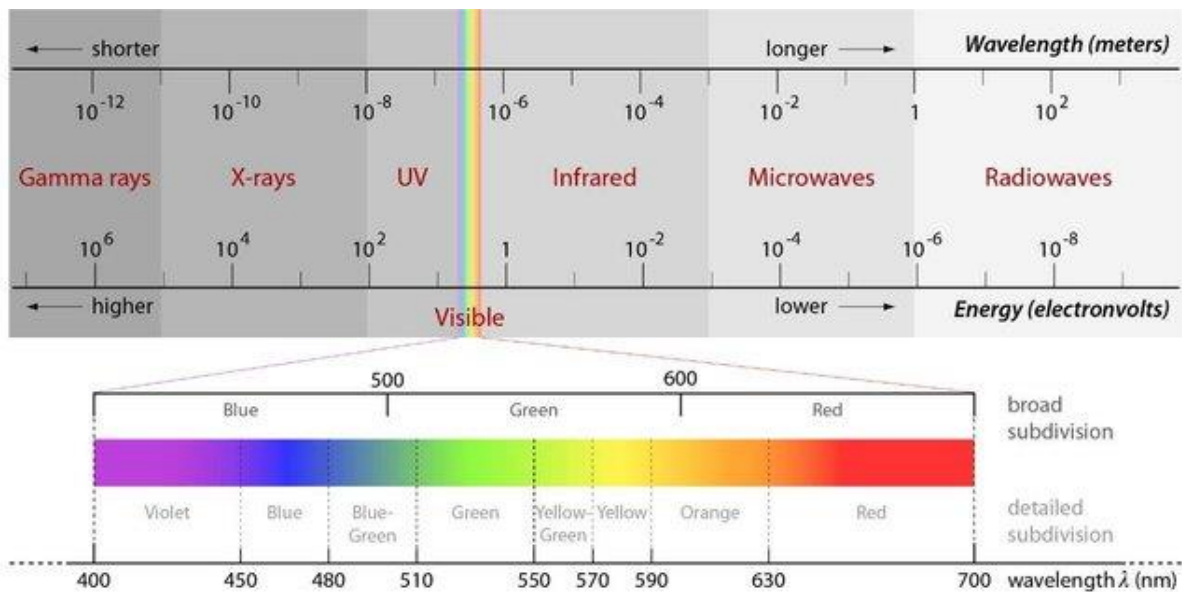


Figure 1.4. The electromagnetic spectrum showing all classes of frequencies. Reproduced from.^[13]

The electromagnetic spectrum in Figure 1.4 shows all classes of radiation, however not every frequency range reaches the Earth's surface. In general, solar radiation received by the surface consists mostly of infrared (52 – 55%), visible (42 – 43%), and ultraviolet (3 – 5%) wavelength regions, which extend from approximately 290 nm to 2.5 μm .^[14] Electromagnetic radiation can be exploited to yield useful work via three main physical mechanisms:

- Conversion to electricity (solar cells).
- Conversion to heat (thermal collectors).
- Conversion to fuel (photosynthesis).

Conversion to electricity occurs when sunlight hits the surface of a solar cell, and photons are absorbed by the light-absorbing material. Consequently, an electron-hole pair is generated by the internal electric field. An electron is excited and separated from the ground state. The excited electrons must remain at the higher energy longer

than the thermal relaxation time so they can be collected. Negative carriers (electrons) are then collected at one contact and positive carriers (holes) in the ground state at another. Subsequently, they both separately travel to the external circuit to do electrical work until they recombine.

1.3.1 Overcoming the Challenges

As illustrated in Figure 1.3, many types of solar devices exist where the competition between the technologies in terms of efficiency and stability is fierce. While particular types, for example, silicon or copper indium gallium selenide (CIGS) solar cells, have undergone successful commercialisation, other alternatives have not yet been so prosperous. For this thesis, research and discussion is focused on two types: dye-sensitized solar cells (DSSCs) and perovskite solar cells (PSCs).

DSSCs have not yet been so successful in terms of commercialization, as there are many drawbacks that have to be solved before the technology can become competitive on the market. As previously noted, in the field of solar energy conversion, efficiency is the key. Therefore, solar technologies have to be high performing. DSSCs were first reported by Gratzel et al.^[15] in 1991. During the last three decades, there have been more than one thousand publications in the field; however, the highest reported efficiency of cells is still at $\approx 13\%$, which was obtained under laboratory conditions.^[16] When large area devices were fabricated (DSSC modules), the efficiency decreased to $\approx 8\%$.^[17] Compared with silicon modules, which can achieve a minimum of 10% efficiency and be stable for 25 years, current DSSCs cannot compete with them. Moreover, the cost of electrical energy that is produced by silicon modules is ≈ 0.66 \$ per watt.^[18] For DSSCs to be comparable to such a price range, the

efficiency of a module would need to be between 13.6 – 17.6%.^[18] In addition, DSSCs suffer from stability issues, whereby the maximum reported outdoor stability was ≈ 2.5 years.^[19,20]

Typically, an iodine-based liquid electrolyte is employed as a hole transport material. This has several disadvantages that lead to the decrease in solar cell efficiency; for instance, electrolyte degradation occurs in the course of the operation, which results in an open-circuit voltage (V_{OC}) decrease. This phenomenon is predominantly induced by the TiO_2 interface or a platinum (Pt) counter electrode. Consequently, the device properties may change after long periods of operation, resulting in a performance decline. While alternatives exist, for instance, carbon-based counter electrodes, they are less favorable, and the efficiencies of non-platinum cells are even lower.^[21]

Preferably, the fabrication of DSSCs should be performed in a low humidity, and oxygen-free environment, since water vapors can degrade light absorbing dyes, affecting the performance and stability of devices. As iodine-based liquid electrolytes are volatile, there is a need for encapsulation. In the course of long-term operation (15-20 years), it can be challenging to prevent a liquid electrolyte from evaporating from the cell. Therefore, efforts were aimed towards replacing liquid-based electrolytes with solid-state or gel alternatives.^[22] While certain drawbacks can be solved by employing such approaches, the efficiencies that were obtained were notably lower. Compared with silicon or CIGS solar cells, DSSCs possess certain benefits (i.e. cost of fabrication), however, for them to be competitive on the market, major breakthroughs would still need to be achieved.

In contrast to DSSCs, PSCs can achieve high efficiencies ($< 20\%$ on a laboratory-scale and $< 15\%$ on large modules) together with low cost fabrication, which renders

this type more appropriate to compete with other technologies.^[23,24] However, they exhibit other drawbacks that impede their rapid commercialisation. One of the major concerns is related to the long-term stability.^[25] Silicon solar cells typically have an efficiency degradation rate of 0.5% per year.^[26] Therefore, for a new photovoltaic technology to be competitive, the degradation rate has to be at least similar or even lower. Currently, PSCs do not exhibit such stability levels, as the perovskite material is prone to degradation. There have been many studies investigating mechanisms for the degradation and one of the main reasons has been attributed to thermal heating.^[26] During operation, a solar cell device is heated as a result of solar illumination, which degrades the material. While certain perovskite structures are more thermally stable than the others, obtaining a perovskite material that sustains no degradation in the course of ≈ 15 years has proven to be a difficult task. There were reports that cation engineering (using double or triple cation structures, which are more stable), or the use of carbon electrodes instead of metal layers, can result in superior properties; however, none of these approaches yielded an acceptable performance.^[27]

In addition to temperature related concerns, other factors, such as UV light, moisture, and hysteresis, all present additional elements that negatively influence the long-term stability. While under dark conditions and low humidity, exposure to oxygen does not represent a significant issue, whereas the presence of illumination can cause the device to degrade.^[28] Excited electrons in the conduction band can react with oxygen, forming superoxide (O_2^-), which can react with organic species (e.g. $CH_3NH_3^+$), leading to the formation of undesirable products.^[29] The major source of oxygen is the atmosphere. However, as reported by Jung et al.^[30], oxygen ions can also come from the metal oxide layer (e.g. TiO_2). Upon illumination, they can diffuse through to the perovskite film and affect device's stability. Nevertheless, the ability to fabricate high

performing solar devices at such a low price presents a major advantage compared to the established photovoltaic technology and if the stability issues can be resolved, PSCs could significantly disrupt the solar market.

1.4 Nanomaterials for Solar Cells Applications

The performance of solar cells can be improved with the implementation of nanomaterials. The optoelectronic properties can be manipulated via nanometer scale engineering, which has led to a variety of different applications employing nanomaterials. They can be synthesized in various different forms, including nanoparticles (NPs), nanofibers (NFs), and nanocrystals (NCs).^[31] Due to the large surface area to volume ratios, they exhibit different characteristics compared to their bulky counterparts. If the radius of a nanomaterial is smaller than the exciton Bohr radius, quantum confinement can be observed, which means that the band gap can be modified as a function of size. This phenomenon has led to many practical uses, for example, gold NPs were shown to act as superior labelling agents in the healthcare industry.^[32] In the field of photovoltaics, the small sizes of nanomaterials can decrease the level of charge recombination.^[33] Therefore, such characteristics make them appealing for the use in solar devices with the aim to increase the efficiency. Their advantages also include increasing or extending optical absorption profiles. Since the control over the shape and dispersity of nanomaterials is related to synthetic approaches, novel methods of preparation are becoming increasingly more important. On the other hand, much work has been done on tuning TiO₂. Several approaches have been implemented, for instance doping TiO₂ with n-type dopants with the aim of increasing the number of free electrons and consequently improving the conductivity.

Alternatively, p-type dopants can be introduced to increase the number of holes. TiO_2 can be modified by altering synthesis approaches via the incorporation of other nanomaterials.^[34] Contrarily, its oxygen vacancy content can be modified by calcining precursors in different atmospheres.^[35] A lot of the prior research has focused on replacing the n-type layer of TiO_2 with other metal oxides, for example: SnO_2 , NiO (p-type DSSCs), Nb_2O_5 , and ZnO . While all these materials have similar band gap values and are non-toxic, the most popular and widely employed semiconductor is TiO_2 .

1.4.1 Nanoarchitectures

A semiconductor layer (typically n-type) has a very important role within a solar device configuration. For example, in DSSCs it provides a surface area for the attachment of dye molecules. A greater surface area allows more dye to be absorbed, which results in better performance. In contrast, the role of the n-type layer in PSCs is mainly related towards the charge transport of carriers. While many types of 1D structures exist, NFs will primarily be discussed in the course of this thesis, as this type was synthesized and used for solar devices. As opposed to NPs that consist of grain boundaries and traps (charge recombination centers), NFs can provide a direct pathway for charge carriers due to their 1D morphology (Figure 1.5).^[36] As there are many factors that have an influence on charge diffusion, including porosity, pore size, orientation, and crystallinity, it is essential to synthesize NFs with the right crystal structure and fewest defects possible. Furthermore, compared to NPs, they exhibit properties such as higher diffusion coefficients, longer electron diffusion length, and the ability to scatter light more efficiently, all of which are advantageous for DSSCs.^[37] NFs are generally known for low Brunauer-Emmett-Teller (BET) surface areas (a drawback in terms of

dye loading), however by combining them in a composite with NPs or with the implementation of doping, the BET surface area values can possibly be increased.^[38]

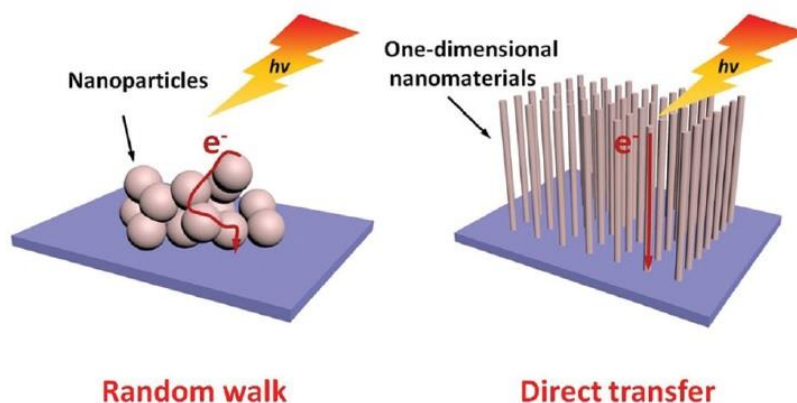


Figure 1.5. The comparison in terms of charge transport ability of NPs and NFs. Reproduced from^[36] with permission from The Royal Society of Chemistry.

1.4.2 Quantum dot nanocrystals

Quantum dots are crystalline semiconducting NPs that have, during the last few decades, attracted substantial research attention. There are many types, for instance binary type II-VI, IV-VI, III-V, ternary type, or the most recent class of perovskite quantum dots with a typical stoichiometry (not the only one) of ABX_3 (A = caesium, FA (formamidinium), MA (methylammonium), etc., B = lead, tin, etc. and X = chlorine, bromine, iodine). Compared to their bulk equivalents, quantum dots exhibit superior optoelectronic properties that are required for lighting applications, such as high color purity and high photoluminescence quantum yields (PLQYs).^[39] Therefore, their main applications include light-emitting diodes (LEDs), lasers, and photodetectors.^[40] Quantum dots are additionally a popular choice for use in solar cells for several reasons; for example, their band gap can be conveniently tuned via size effects or composition control, which in photovoltaics can be used to fabricate multijunction solar

cells. In addition to their high molar extinction coefficients, quantum dots exhibit non-conventional properties (the generation of multiple excitons) that can lead to overcoming the Shockley-Queisser efficiency limit for single-junction solar cells.^[41]

While lead or cadmium-based quantum dots have already been widely explored, perovskite quantum dot nanocrystals (QDNCs) only emerged a few years ago. Their characteristics were shown to be very different, whereby the main dissimilarity can be pointed towards the defect tolerance. Despite years of investigation, old classes of quantum dots were not successfully commercialized; however, the perovskite type has shown to be more promising and has become the center of research attention worldwide.^[42]

1.5 Nanomaterials and Solar Cell Characterisation

Many techniques exist that can be used for the characterisation of nanomaterials. However, the discussion presented in this work focuses on the ones that were employed in the experimental chapters of this thesis.

Absorption spectroscopy is used to evaluate the absorption characteristics of nanomaterials over a desired wavelength range. Since radiation varies as a function of wavelength, the differences in intensity can be recorded on the spectrum.

Fluorescence spectroscopy is employed to investigate fluorescence (emission of light) from a sample. This involves the use of a monochromatic light beam that excites the sample, causing an emission that is then recorded by the instrument.

Morphological features of nanomaterials are usually investigated using scanning electron microscope (SEM) or transmission electron microscope (TEM). One of the

main differences between these two techniques is the interaction of electrons with a sample. In TEM, electrons are transmitted through the sample to form an image, as opposed to SEM where electrons are scattered on the surface, where, based on their interactions with atoms of the sample, an image is produced. With TEM, more characteristics from a sample can be obtained, such as crystallization, stress, and morphology; with SEM, it is mostly morphological features that can be investigated.

The elemental composition of a sample can be analyzed using X-ray photoelectron spectroscopy (XPS). This is a surface-sensitive technique that generally provides information on elemental identification, quantification, and their chemical state.

For phase identification, X-ray diffraction (XRD) is used. This is a crystallographic technique that involves a monochromatic beam of X-rays that diffract from a crystalline sample into the detector. By measuring angles of the diffracted beams, an XRD pattern is produced as a function of their intensities.

Similarly to XRD, Raman spectroscopy is also a light-scattering technique. However, here, light interacts with chemical bonds within a material. Most of the scattered light is of the same wavelength as the laser, however a very small percentage of it is at a different wavelength, which is what is measured for a material's characterisation. Information that can be provided from this technique includes chemical structure, phase, molecular interactions, etc.

The nature of chemical bonds in nanomaterials can be characterised by employing Fourier-transform infrared (FTIR) spectroscopy. This is a technique whereby light absorption across a range of wavelengths is measured. A non-monochromatic beam interacts with a sample, and a machine measures how much of the light was absorbed

at a specific wavelength, producing a FTIR spectrum of either light emission or absorption over different wavelengths.

Information about physical or chemical phenomena, for instance, absorption, desorption, and thermal decomposition can be revealed using thermogravimetric analysis (TGA). In this technique, mass of a sample is measured as a function of the temperature range where time of exposure can be selected.

To determine the surface area of nanomaterials, the BET method is usually employed. This technique is based on the physical adsorption of gas molecules, which yields gas adsorption isotherms at the boiling point of a gas. Nitrogen is typically employed as a carrier gas, however other gases, for example argon or carbon dioxide, can also be used. The choice of carrier compounds is not restricted to gases only, since organic vapors are likewise used (dynamic vapor sorption). The process of adsorption is caused by Van der Waals forces that are created between the adsorbent (a substance that adsorbs others onto its surface) and adsorbate (a substance that is adsorbed on a surface of another substance). The latter process is termed as physical adsorption, as opposed to chemical adsorption that involves a chemical reaction between the two substances. From the number of adsorbed species at a constant temperature (BET isotherm), the BET surface area can be determined. There are six different types of BET isotherms that can be obtained during the adsorption process, which are illustrated in Figure 1.6.

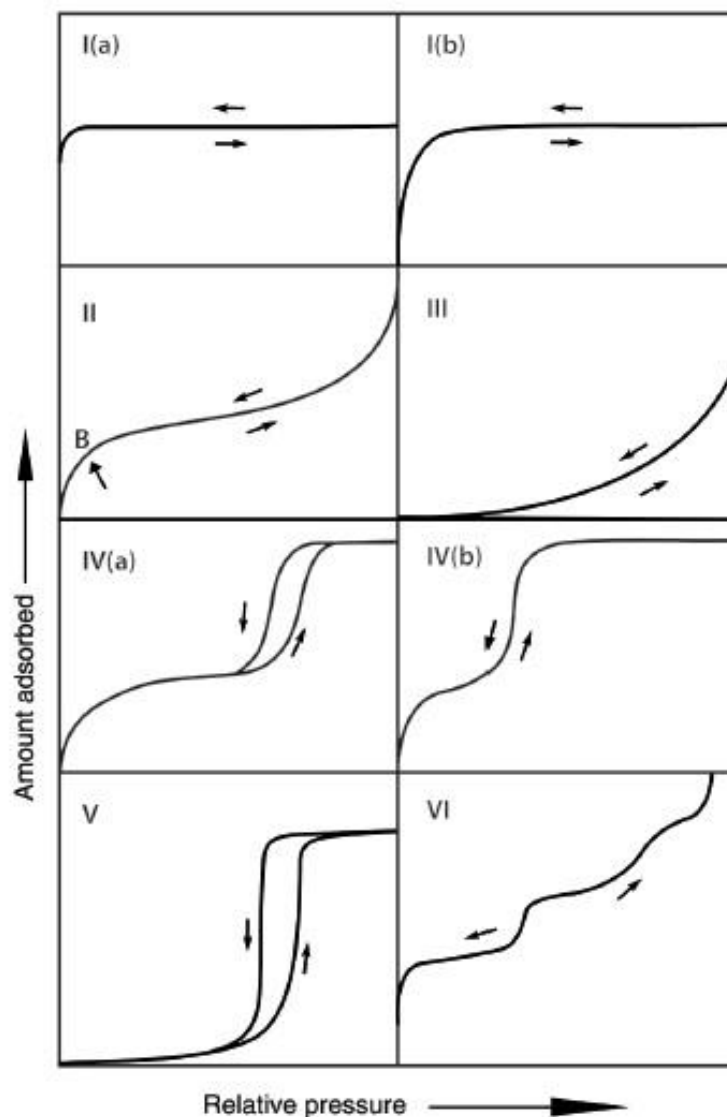


Figure 1.6. Six typical BET isotherms. Reproduced with permission.^[43] Copyright 2019, Wiley.

Photovoltaic performance of the solar cell device is evaluated by current-voltage (I-V) and incident photon conversion efficiency (IPCE) methods. The I-V curve is normally used to determine the power conversion efficiency (PCE) of the solar cell under light irradiation. From the latter curve, the main photovoltaic parameters are obtained. It is important to perform measurements under specified conditions to allow comparisons of the results from different researchers around the world. On the other hand, IPCE

correlates to the number of generated electrons divided by the number of incident photons. This measurement reveals information about the optical absorption spectra of the device and must align with the generated current as obtained from the I-V curves.

1.6 Aim of this work

The aim of this thesis is to focus on researching the drawbacks that prevent the commercialisation of solar energy technology. To address these issues, nanotechnology was employed. Synthesized nanomaterials were characterised and/or used in solar devices.

Chapter 2 focuses on the topic of DSSCs. The purpose of the work has been to enhance the efficiency of solar devices with the implementation of gold NPs that were separately added to the n-type layer. TiO₂ NFs (a type of 1D nanomaterial) were used in conjunction with the gold NPs. Their advantage of offering a direct pathway for light generating carriers was combined with using gold NPs, which exhibit a localised surface plasmon resonance (LSPR) effect. Since the former characteristic is not the same for all NP sizes, the influence of different sizes was studied. While studies investigating a range between 12 and 100 nm have already been performed, no one has explored the sub-12 nm size range. By implementing a novel synthesis method, the following sizes were produced: 5, 8, 10, and 12 nm gold NPs and separately combined with TiO₂ NFs with the purpose of using the material for DSSCs. The intention of using a composite nanomaterial was to decrease the charge recombination level, improve the reaction kinetics of oxidation and reduction (iodine electrolyte), and to make use of the scattering effect enabled by gold NPs.

In chapter 3, a similar composite nanomaterial was assembled, however, the gold NPs were replaced with lanthanum and lithium ions, which are known to exhibit favorable characteristics in the field of photovoltaics. The metal ions were (separately) directly added to the precursor solution to produce NFs, which is a cost-effective approach. The composite nanomaterial was then used to fabricate DSSCs and PSCs with the aim of increasing their efficiency, and to study the influence of lanthanum and lithium ions on the performance of different types of solar cells, when they are employed in a n-type layer.

Lastly, in chapter 4 the work was expanded towards nanomaterial synthesis: perovskite QDNCs were synthesized. With the use of novel ligands, the synthesis was performed at RT (room temperature) conditions, in non-polar solvents, and without the use of an inert atmosphere. This method yielded high-quality QDNCs with the performance metrics in line, compared to the hot-injection route. This novel approach is cost effective and can be used for upscaling.

At the end of the document, the results and discussion are summarized, together with the description of novel findings that emerged from this research project.

Chapter 2

The influence of different-sized gold NPs on dye-sensitized solar cells

2. The influence of different-sized gold NPs on dye-sensitized solar cells

2.1 Introduction

TiO₂ belongs to the group of metal oxides that have been widely investigated as semiconductors in the last few decades.^[44] As a result of its favourable characteristics, for instance durability, environmental friendliness, and low price, TiO₂ has been used in a range of different applications.^[45,46] It is known to be a n-type material because the majority of charge carriers are electrons. Therefore, in the field of photocatalysis, TiO₂ has the ability to oxidize oxygen or organic pollutants, and its use for artificial photosynthesis has been extensively investigated.^[47–49] However, one of the main discoveries for the application of this material is in photovoltaics.^[50] DSSCs were the first type to have TiO₂ implemented as an electron transport material, then followed by other related photovoltaic technologies.^[51,52] The morphology commonly used in such configurations are TiO₂ NPs. Despite the many advantages that NPs exhibit, they suffer from the following drawbacks, which can negatively influence the performance of solar devices, including: (i) limited charge transport due to the grain boundaries, (ii) low absorption of high-wavelength photons and (iii) high charge recombination that is related to the presence of grain boundaries.^[53] With the aim to resolve these drawbacks and consequently obtain higher efficiencies, a lot of research work has been devoted towards improving the semiconductor photoelectrodes via nanostructuring.^[54] To complement this, 1D nanostructures have been particularly popular since disadvantages related to the charge transport in NP based configurations can be reduced by replacing them with 1D nanomaterials.^[55] Such

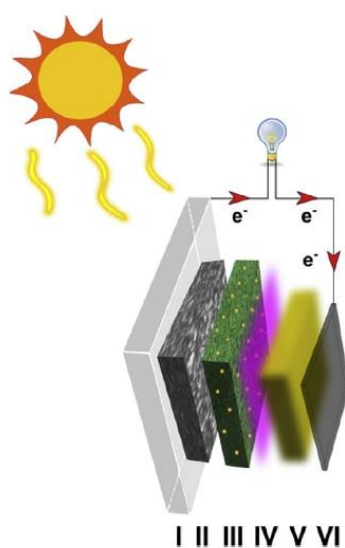
nanostructures (i.e. nanotubes, nanowires, and NFs) possess higher diffusion coefficients and longer electron diffusion lengths, which together with the light-scattering characteristics (improved light harvest), can improve the performance of solar cell devices. Moreover, 1D nanostructures can also offer a direct pathway for electrons travelling through the semiconductor layer to the conductive substrate.^[53] To synthesize NFs, electrospinning is typically employed, which is a cost-effective and straightforward method that allows the preparation of various types of nanomaterials. While NFs produced via this approach are typically randomly oriented, it is also possible to electrospin them in an aligned orientation.^[56] The latter configuration exhibited certain advantages. For instance, compared to randomly distributed NFs, it improved photoluminescence quenching, which was attributed to better charge separation efficiency leading to enhanced PCE. On the other hand, Du et al.^[57] investigated DSSCs with both TiO₂ and ZnO NFs and showed higher efficiency compared to single type NFs. Since a significant disadvantage of NFs is their low BET surface area, there were reports that utilised both, e.g. NPs and NFs. As shown by Wang et al.^[58], the combination improved the photovoltaic performance. It should be noted that during the electrospinning process, there is an effect of humidity on the properties of NFs, which was explored by Tikekar et al.^[59] It was reported that extreme conditions in terms of relative humidity (RH) are not favorable as this inhibits the fibre formation.

On the other hand, the addition of noble metal nanostructures to the semiconductor layer of DSSCs was also shown to be a successful approach for improving the performance of related devices.^[60] Noble metal NPs have various advantages and consequently they have been widely studied for implementation in different types of applications. Amongst several types of metal NPs, gold NPs have shown to be

particularly beneficial as a result of effects that include: light-scattering and emission, local field enhancement, and facilitation of the separation of charges and their transfer.^[61,62] However, such characteristics can only be achieved in DSSCs by modification of their constituent components. For instance, to enhance the performance of DSSCs, previous studies have noted methods such as; (i) the addition of gold NPs inside thin films (light-scattering effect), (ii) the inclusion of gold NPs to the light absorbing films to improve light harvest, and (iii) doping of n-type layers to enhance charge transport characteristics of films.^[62,63] The plasmonic properties of gold NPs are tunable, which enables their wide usage in photovoltaic devices. Therefore, in the field of DSSCs they have been incorporated into different layers of the device configuration.^[64] However, despite being incorporated into the transparent or a scattering layer, the improved characteristics commonly originated from the better photocurrent density.^[62] While previous studies have suggested that enhanced photocurrent density was a result of higher dye-uptake due to the improved surface area coverage, recently the phenomenon was attributed to their plasmonic effects.^[62,65] In addition, the amount of gold NP loading into the DSSC system, also plays an important role in the resulting performance. Specifically, an excess can act detrimentally, causing interactions with the electrolyte or leading to higher degree of charge recombination, which negatively influences the performance metrics. It was determined, that additions above 1 wt% lead to the increased probability of aggregation of NPs (gold or silver) and the semiconductor film.^[66] Despite the light absorbing characteristics of gold NPs, a light absorbing compound that can cover a large portion of the visible range is also needed for a sufficient light harvest of related photovoltaic technologies. For the application in DSSCs, a ruthenium-based dye (N719) with a strong absorption band at 530 nm is traditionally employed. It should be

noted that non-ruthenium-based alternatives also exist, however they are not as efficient.^[67] Gold NPs sized between 5 and 50 nm exhibit strong plasmonic resonance in the range 515-540 nm, which aligns well with the N719 dye. In addition to the amount added, the size of gold NPs also has an important impact on the DSSCs performance. As reported by Wang et al.^[62], the separate addition of 5, 45, and 110 nm gold NPs results in different efficiencies. Particularly, 45 nm sized gold NPs showed the highest values of photocurrent. Such a phenomenon was attributed to the absorbance characteristics of 45 nm gold NPs that had the best overlay with a N719 dye. Therefore, the LSPR effect was the strongest for this combination, resulting in enhanced light absorption and consequently high short-circuit current density (J_{sc}). Nevertheless, the overall PCE was shown to be the highest for DSSCs with 5 nm gold NPs.^[62] While smaller sized NPs exhibit a reduced scattering cross-section compared to a larger size, collectively, they can still scatter the same, or even more than a single large gold NP. On the other hand, they show higher light absorption (absorption cross-section). Such features can have a beneficial influence on electron collection and therefore on the overall values of PCE. Typically, the combination of gold NPs and TiO₂ for photovoltaic technologies includes larger sized NPs, where smaller sizes are considered to have photocatalytic properties.^[68] To synthesize < 12 nm gold NPs, the use of non-conductive capping ligands is usually required; for instance polyvidone,^[65] poly(oxyethylene),^[69] polymeric stabilizers,^[70] or thiol moieties.^[71] The use of such insulating ligands is typically limited in devices that require good charge transport characteristics. However, as reported by Puntès et al.,^[72] below 12 nm gold NPs can also be synthesized without the employment of the aforementioned ligands, making them suitable for use with TiO₂ photoelectrodes.

In this research, the beneficial properties of the two types of nanomaterials (TiO_2 NFs and gold NPs) were combined and used to fabricate TiO_2 photoelectrodes. In this configuration, the aim of TiO_2 NFs was to scatter light, and the purpose of the gold NPs was the LSPR effect, as seen in Scheme 1. The utilization of TiO_2 NFs and different sized < 12 nm gold NPs for the investigation of the performance of DSSC, has been monitored to discover the optimal size limit for efficiency improvement in DSSCs. A simple route to fabricate TiO_2 NFs and combine these nanomaterials with size controlled below 12 nm gold NPs is presented below, where the combination is used for a scattering layer in a DSSC film configuration.



Scheme 1. Schematic depiction of a TiO_2 photoelectrode used for DSSCs. The layers in a configuration are represented by: (I) FTO glass, (II) a transparent layer of TiO_2 NPs, (III) a light-scattering layer of gold NPs-NFs, (IV) a light-absorbing layer of N719 dye, (V) electrolyte and (VI) FTO/Pt counter electrode. Reproduced with permission.^[73] Copyright, 2018 Elsevier.

2.2 Experimental Section

All compounds for this study were obtained from Sigma Aldrich unless otherwise specified.

2.2.1 Synthesis and growth of gold NPs

The synthesis of gold NPs was achieved in accordance with the method previously published by Punter et al.^[72] In summary, a 150 mL water solution of trisodium citrate anhydrous (2.2 mmol/L), consisting of 0.1 mL of gallotannin (2.5 mmol/L) and 1 mL of carbonic acid dipotassium salt (K_2CO_3 , 150 mmol/L) was calcinated to 70 °C under magnetic stirring. After the solution was heated to 70 °C, 1 mL of hydrogen tetrachloroaurate ($HAuCl_4$, 25 mmol/L) was introduced and consequently the colour immediately turned from transparent, to black, to soft pink. This remained at 70 °C for an additional 10 minutes to achieve the total reduction of tetrachloroaurate. At this point, a small portion of the solution was separated and characterised, employing UV/Vis and TEM to confirm synthetization of 5 nm sized gold NPs (their size always refers to their diameter). Other sizes of gold NPs (8, 10, and 12 nm) were additionally obtained from the vial with 5 nm gold NPs. To achieve this nucleation, the vial was decreased in concentration by first removing and then adding 55 mL of the same amount of aqueous solution of sodium citrate as described previously. The diluted solution then underwent heating treatment to 70 °C, followed by two additions of 0.5 mL tetrachloroaurate solution (25 mmol/L) at 10-minute intervals. The same nucleation steps were also undertaken for other particles sizes. The concentration of synthesized

solutions was $\approx 7 \times 10^{13}$ NP mL⁻¹. Each size was determined by counting 100 different Au NPs from that specific batch in an image processing program (ImageJ).

2.2.2 Preparation of TiO₂ NFs

TiO₂ NFs were produced following the method by Macdonald et al.^[55] In a typical procedure, a sol-gel solution was prepared by combining tetrabutyl titanate (0.5g), a polymeric binder (1-ethenylpyrrolidin-2-one – PVP, 1g), and ethyl alcohol (10 mL). This sol-gel solution was then used to electrospin TiO₂ NFs. It is noteworthy, that first PVP has to be properly dissolved in ethyl alcohol by 24-hour vial stirring, before tetrabutyl titanate is added. If the latter compound is added before the complete dissolution of PVP, white agglomerates form in the solution, which cannot be used further. For electrospinning of the TiO₂ sol-gel precursor solution, a voltage of 10 kV with a flow rate of 1 mL h⁻¹ was used. The collection plate, consisting of an aluminium cover, was maintained in the range of 20 cm. After a sufficient amount of the product was produced, fibre mats underwent a pyrolysis treatment to remove a polymeric binder (PVP) at 500 °C for a few hours, resulting in a polymer-free TiO₂ NFs.

2.2.3 Preparation of TiO₂ NF photoelectrodes

To prepare control TiO₂ NF photoelectrodes, TiO₂ NFs (0.5 g) and ethanol (20 mL) were blended together, followed by sonication until no solid clusters of NFs were observed. This took approximately 2 hours, resulting in a homogeneous NF suspension. This solution was combined with 2 mL of terpene alcohol, followed by additional ≈ 15 min sonication. To prepare a slurry of TiO₂ NFs suitable for a

photoelectrode deposition, ethanol was removed by rotary evaporator. The resulting paste was subsequently used to deposit a second layer of DSSC architecture. The first layer had been deposited from a commercially available paste (Dyesol) of TiO₂ NPs on a conductive glass substrate (FTO). The glass substrates subsequently underwent calcination at 500 °C for the purpose of the suitable crystal phase formation, and the elimination of all organic compounds that were present in a paste of TiO₂ NPs. It should be noted that the heating to 500 °C was achieved via intervals of 10 min at 150 °C, 10 min at 325 °C and 30 min at 500 °C. Next, the photoelectrodes underwent treatment in tetrachlorotitanium (TiCl₄, 40 mmol/L) aqueous solution for 30 min at ≈80 °C. The glass substrates were later rinsed with deionized water, followed by pyrolysis at 500 °C as described before. Afterwards, the second layer of TiO₂ NFs (the paste described earlier) was deposited on top of the first layer of TiO₂ NPs using a doctor blading technique. Finally, the glass substrates were once more exposed to pyrolysis at 500 °C, resulting in TiO₂ layers with the appropriate crystal structures, but without the presence of any organic compounds. For the photoelectrodes that consisted of different-sized gold NPs (0.5 wt% - determined solely from the mass of TiO₂ NFs), every particle size (8, 10, and 12 nm) was added to the NF paste, followed by the same procedure as described earlier. It is noteworthy that gold NPs were added only to a light-scattering layer of TiO₂ NFs. As previously reported by Kim et al.^[66] the loading of 0.5 wt% of gold NPs was determined to be optimal for light conversion efficiency in similar systems. The amount of loading remained unchanged for all photoelectrodes fabricated in this study, and their total cell area was 0.125 cm².

2.2.4 Fabrication of dye-sensitized solar cells

Directly after sintering, when photoelectrodes were still warm, they were immersed in an ethanol solution of a Ru-based dye for 20 hours in a light insulated box. The dye solution was prepared by dissolving Di-tetrabutylammonium cis-bis(isothiocyanato)bis(2,2'-bipyridyl-4,4'-dicarboxylato)ruthenium(II) dye, also known as N719 (Solaronix, 0.5 mmol/L) in an ethanol solvent. After sensitisation, the area of the photoelectrodes covered with TiO₂ layers (0.125 cm²) changed colour from white to dark purple and was subsequently rigorously rinsed with ethanol to eliminate any solid dye aggregates from the sensitisation process. Afterwards, these photoelectrodes were pressed onto commercially available counter electrodes that consisted of a layer of a platinum metal (Dyesol) and were enclosed with a polymer adhesive (Dyesol, MS004610). They were placed in a hot furnace (≈110 °C) for ≈12 min to melt the adhesive polymer between the photo and counter electrodes. Finally, the electrolyte was introduced between the secured and tight electrodes using a desiccator connected to the vacuum. The electrolyte was pre-made and consisted of diiodine (I₂, 0.05 mol/L), lithium monoiodide (LiI, 0.1 mol/L), 1-propyl-2,3-dimethylimidazolium iodide (DMPII, 0.6 mol/L), and 4-tert-Butylpyridine (TBP, 0.5 mol/L) in cyanomethane solvent.

2.2.5 Details of instrumentation used

UV/Vis measurements were carried out with a Perkin Elmer Lambda 950 instrument (measurement interval was 1 nm). SEM was performed with a Carl Zeiss XB1540 Cross-Beam Focused-ion-beam microscope. For TEM, a JEOL 2010 TEM operating

at 200 kV was used, where images were compiled with Gatan Digital Micrograph software. Dimensions of NPs were determined using ImageJ software. For XRD measurements, a Bruker D8 Discover X-ray diffractometer with a single wavelength Cu K α_1 and Cu K α_2 emission (wavelengths of 1.54056 and 1.54439 Å) was implemented. For the XRD data analysis, CrystalDiffract software was used where the obtained data was compared to the ICSD standard dataset. XPS was executed on a Thermo Scientific K-alpha photoelectron spectrometer with a single wavelength Al-K α emission. The C 1s (285 eV) was the charge correction benchmark where the data was analysed in CasaXPS software. Measurements were performed by producing a monatomic depth profile of the sensitized areas, via an ion beam to etch the surface coverage. The process of etching took place for 400 sec resulting in 100 nm penetration of the top area.

2.2.6 Photovoltaic characterisation

DSSCs were characterised under AM 1.5 standard spectrum conditions where a LOT calibrated solar simulator was used with an integrated xenon lamp. DSSCs were attached to a Keithley 2400 source meter for data collection. I-V curves were obtained with a halogen lamp connected to a frequency of 188 hertz through a Newport monochromator; a 4-point probe in connection with a lock-in amplifier. The single wavelength laser was adjusted using a silicon (Si) photodiode, and the results were evaluated using Tracer 3.2 software to obtain the (IPCE) ratios.

2.3 Results and Discussion

2.3.1 Materials characterisation

To examine changes between different batches of gold NPs, they were characterised using UV/Vis and TEM, as can be seen in Figure 2.1. Batches corresponding to size increase of gold NPs, exhibited a bathochromic shift in absorbance (Figure 2.1a), which is in agreement with the literature.^[72] The LSPR peak for different sized (5 to 12 nm) gold NPs were located at 514, 515, 517, and 518 nm respectively, where all had similar values of full-width at half maximum (fwhm). The concentration of solutions of gold NPs was $\approx 7 \times 10^{13}$ NPs mL⁻¹. The LSPR peaks for gold NPs slightly overlap, compared to a solution of a N719 dye. Therefore, any increase in light harvesting capabilities of photoelectrodes containing gold NPs, can be a characteristic of their plasmonic effect. The size distribution of gold NPs in their related batches was determined using TEM, and different points on the TEM mesh were analysed. It was determined, that the average sizes of gold NPs, referred to here as 5, 8, 10, and 12 nm, were as follows, and the standard size deviations (σ) are shown in brackets: 5.3 nm ($\sigma \approx 10.3\%$), 8.8 nm ($\sigma \approx 8\%$), 10.4 nm ($\sigma \approx 7.5\%$), and 12.3 nm ($\sigma \approx 8.4\%$), respectively. Figure 2.2 illustrates TEM images of gold NPs that were taken from various areas of the TEM grid and used for the particle size analysis. Furthermore, TEM was also used to investigate shape and crystallinity of gold NPs (Figure 2.1b). It was determined that they exhibited a spherical shape with a separation between lattice planes of 0.23 nm, which corresponds to the {111} crystal plane of gold.^[74] The gold NPs also showed stability since they remained distributed in the solution for many weeks, and no signs of agglomeration or precipitation occurred.

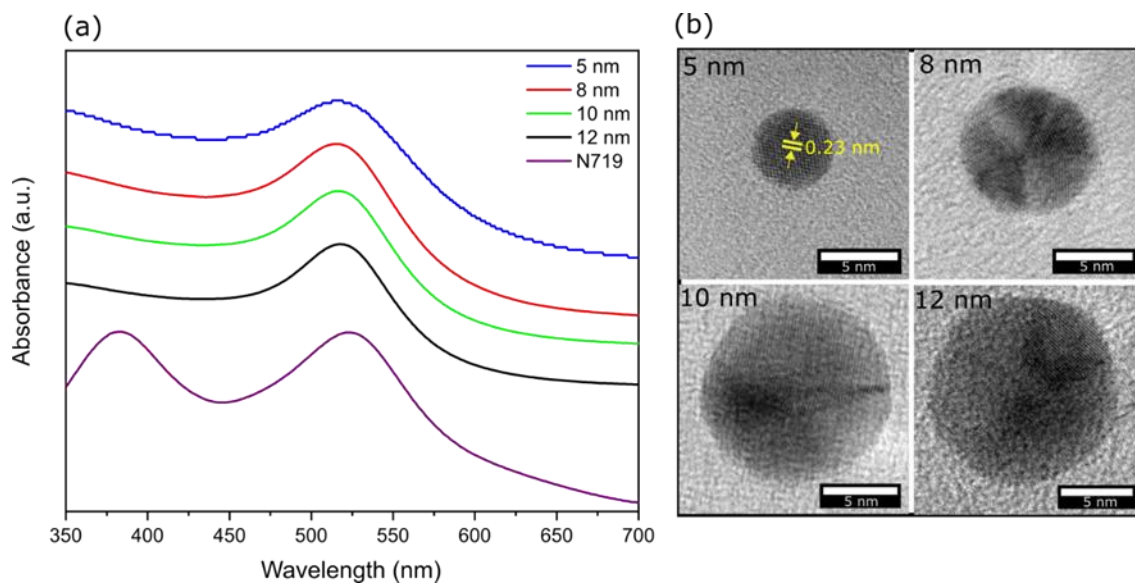


Figure 2.1. (a) UV/Vis absorption spectrum of aqueous solutions of gold NPs (5, 8, 10, and 12 nm size) together with a N719 dye. (b) HR-TEM images of gold NPs, validating their high degree of crystallinity.

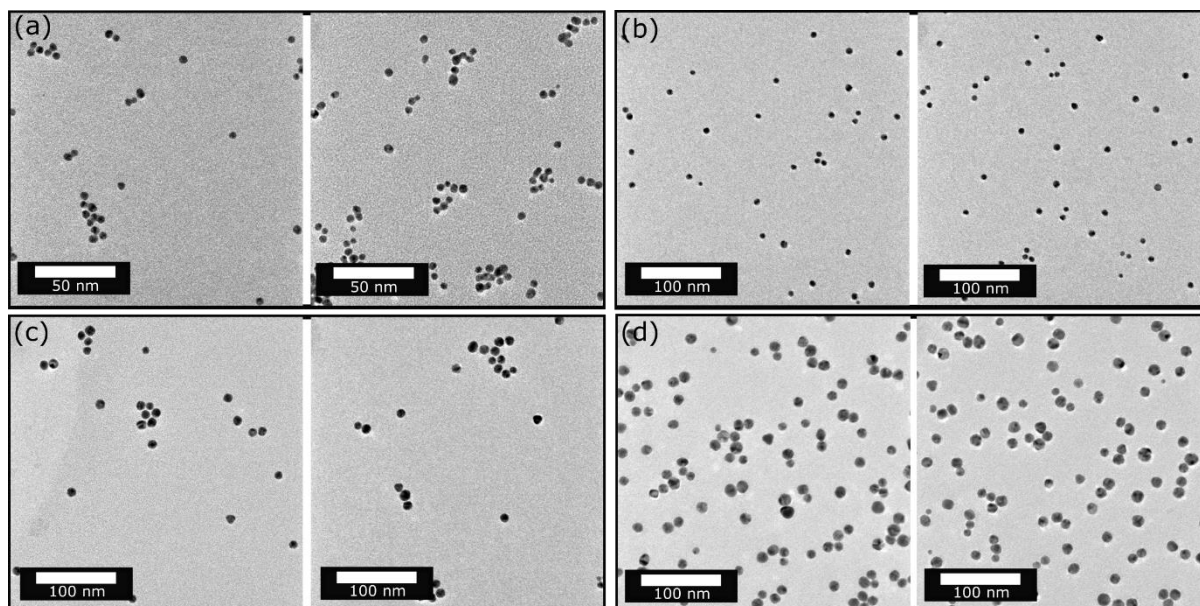


Figure 2.2. TEM images used for the size analysis of (a) 5 nm, (b) 8 nm, (c) 10 nm and (d) 12 nm gold NPs, respectively. Based on these images, an average size distribution for a particular batch was determined to be (a) 5.3 nm ($\sigma \approx 10.3\%$), (b) 8.8 nm ($\sigma \approx 8\%$), (c) 10.4 nm ($\sigma \approx 7.5\%$) and (d) 12.3 nm ($\sigma \approx 8.4\%$) with the corresponding standard size deviations in brackets.

To implement TiO₂ NFs for DSSCs, screen printable pastes were made as discussed previously. Different-sized gold NPs were separately incorporated into the pastes, which were then doctor bladed on top of an initial layer of TiO₂ NPs and labelled as a light-scattering layer. The layers were assembled on a conductive transparent substrate (FTO glass). A significant drawback related to the use of 1D nanomaterials, such as NFs in DSSCs, is their BET surface area, which is related to the diameter of NFs, where it decreases as a function of the diameter increase. However, compared to NPs it is notably lower. Therefore, the purpose of a transparent layer that consisted of smaller sized NPs was to provide sufficient area for the incorporation of dye molecules. Scheme 1 (see above) shows the DSSC configuration that was used in this study. Since the optimal thickness for both layers is critical to achieve high performance in DSSCs, a cross-section SEM image of the photoelectrode used for DSSCs was obtained and is illustrated in Figure 2.3a. It was determined that the total thickness of both layers was 13 μm, which is optimum for the production of efficient DSSCs. The photoelectrodes consisted of three main parts (labelled in Figure 2.3 as I, II, and III); I indicates FTO glass, II is related to the 8 μm thick transparent layer of TiO₂ NPs, and III represents the 5 μm light-scattering layer of TiO₂ NFs. The thicker layer provided the surface area for the dye attachment, while the thinner light-scattering layer improved sun harvesting via a light-scattering effect. To investigate the diameters of TiO₂ NFs, a high-resolution (HR) SEM image of a light-scattering layer is shown in Figure 2.3b. The diameters were determined to be between 200 and 700 nm, while the length was several μm long. Although efforts were focused on the detection of gold NPs, they were not found to be visible via SEM. This was associated with their quantity, since the amount added was only 0.5 wt%. However, in an attempt to identify them, HR-TEM images were investigated. Figure 2.3c shows the elemental

mapping of the photoelectrode. Although challenging, in order to reveal a single gold NP embedded in TiO₂ NFs, these gold NPs were undoubtedly confirmed, as illustrated with the corresponding colour of the mapped elements.

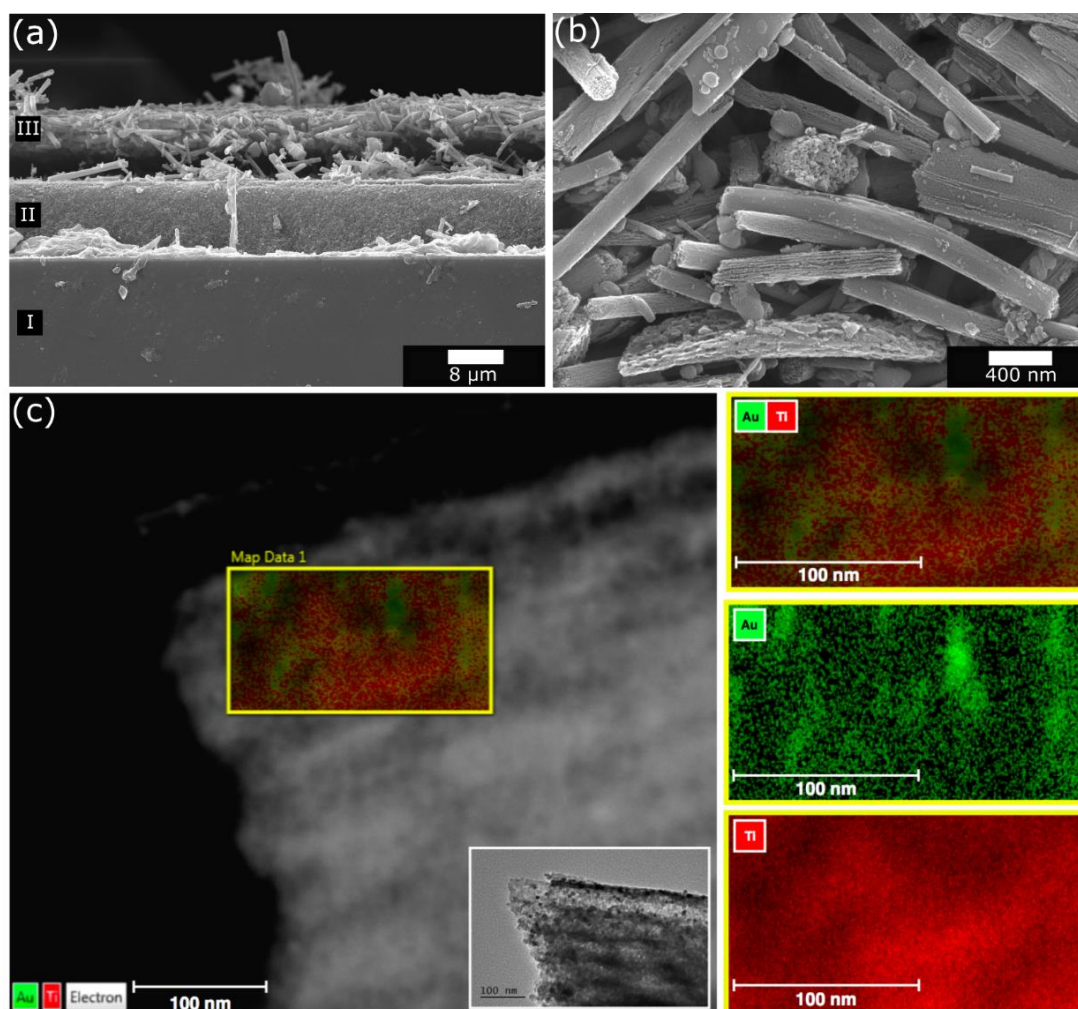


Figure 2.3. (a) Cross-sectional SEM image of a photoelectrode used for DSSCs. The numbers assigned to each layer present: I = FTO glass, II = transparent layer of TiO₂ NPs, III = light-scattering layer of TiO₂ NFs. (b) HR-SEM image of TiO₂ NFs with added gold NPs. (c) TEM image of a TiO₂ photoelectrode containing gold NPs with elemental mapping inset. The corresponding images present mapped elements - gold is represented by green, and titanium by red, respectively. Reproduced with permission.^[73] Copyright, 2018 Elsevier.

Further characterisation about the embedment of gold NPs within the TiO₂ NFs was carried out using XPS. The NPs were successfully detected, as illustrated in Figure 2.4. To confirm that they were also present inside the material, a monatomic depth profile of the photoelectrodes was performed. This included the etching of the surface layers of the photoelectrode with a calibrated ion beam for 400 sec, which resulted in penetration in the range of ≈ 100 nm. Such measurements revealed sub-surface information of the photoelectrodes, where gold NPs were added. Since NFs consisted of TiO₂, Ti 2p peaks were present at binding energies of 464.2 eV and 458.5 eV, corresponding to Ti 2p_{1/2} and Ti 2p_{3/2} spin-orbit components, respectively (Figure 2.4a). Moreover, gold NPs were successfully detected with binding energies present at 83.7 eV and 87.5 eV, corresponding to Au 4f_{7/2} and Au 4f_{5/2}, respectively (Figure 2.4b). Such spin-orbit splitting of 3.8 eV is typical for gold in 4f regions. Since the binding energies can reveal information about the oxidation states of elements, the positions of the peaks were compared with the reports in the literature. For gold NPs present on TiO₂, previous studies have reported that for Au⁺ 4f_{7/2} and Au³⁺ 4f_{7/2}, there is a notable shift in the direction of higher binding energies, namely 84.4 eV and 86.5 eV, respectively.^[75,76] Compared with the results of this study, only one species at 83.7 eV was present (Figure 2.4b). Since the metallic gold is commonly present at 84.0 eV, the peaks obtained from the photoelectrodes with added gold NPs can be attributed to the gold in zero oxidation state. While a negative shift of 0.3 eV is present for gold 4f_{7/2}, it can be associated with the strong interaction between the gold NPs and TiO₂ NFs.^[76] As can be observed from the XPS data (Figure 2.4b), the gold 4f spectrum showed to be rather noisy. However, this was attributed to the low amount of added gold NPs (0.5 wt%) and has already been reported elsewhere.^[63] TiO₂ material can exhibit various types of crystal structures (brookite, rutile, anatase).^[44] To gain insights

on what type was present in photoelectrodes, and whether the addition of gold NPs caused any alterations, XRD analysis was performed. The results revealed that the anatase crystal phase of TiO_2 was present, which was confirmed based on the standard XRD reference patterns (JPCDS card number 9852), as can be seen in Figure 2.4c. Additional signals, not identified as the same phase, can also be observed on the XRD pattern. Since TiO_2 layers were deposited on FTO glass (photoelectrodes were used for the measurements), these signals were assigned to the FTO layer. As noted by other researchers,^[77] peak shifting can occur if metal NPs are incorporated into the TiO_2 framework, however in analysing the XRD results of this study, no peak shifting was observed. Furthermore, due to the low concentration of gold NPs, no characteristic XRD diffraction peaks were detected. On the other hand, if the gold content was higher or if their particle sizes were larger, changes could potentially be observed.^[76]

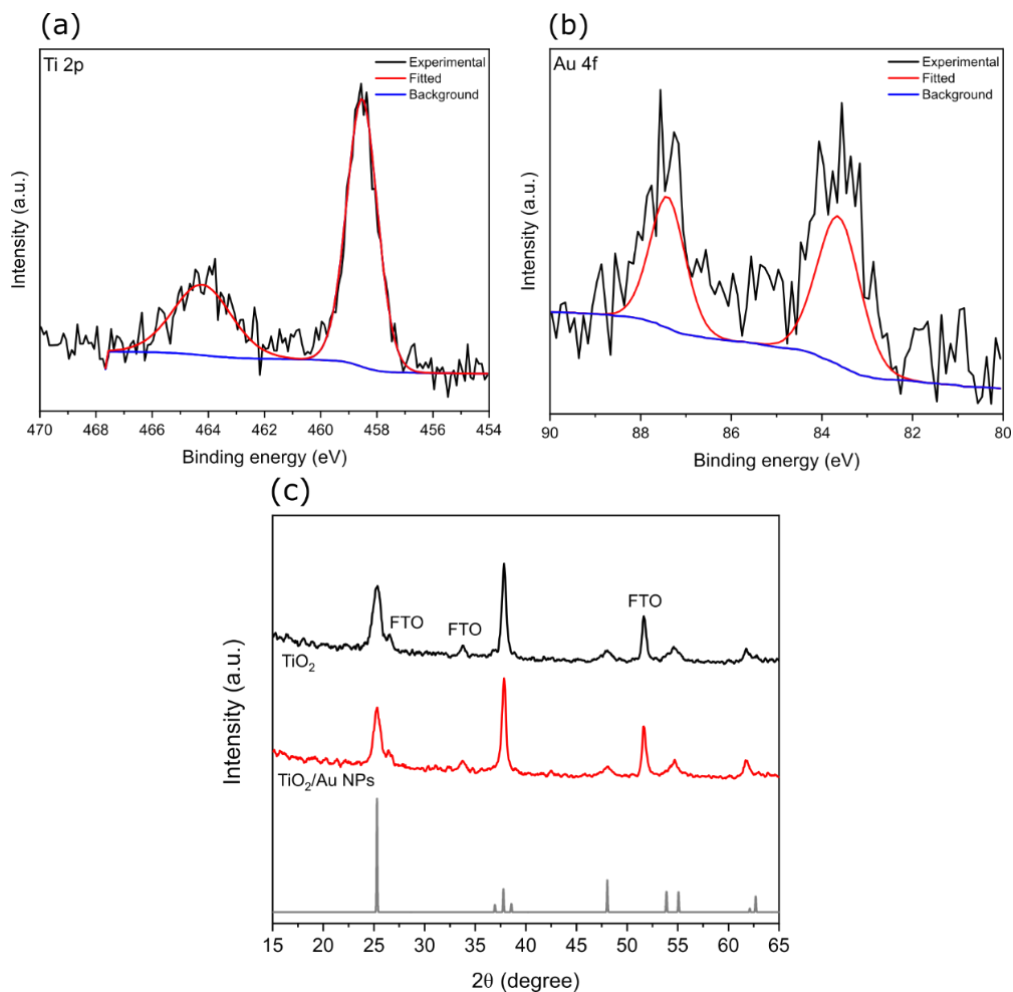


Figure 2.4. XPS spectra for (a) Ti 2p and (b) Au 4f of a photoelectrode containing gold NPs. (c) XRD patterns for photoelectrodes with and without gold NPs. Standard anatase TiO₂ phase is shown at the bottom in grey (JPCDS card number 9852).

XRD is usually implemented for studies of long-range structural arrangements, chemical composition, and physical characteristics of various types of materials.^[78] However, to acquire information about the absorbance properties of photoelectrodes, UV/Vis measurements were performed. As opposed to the UV/Vis absorption spectrum for solutions of gold NPs (Figure 2.1a), no LSPR peaks appeared for photoelectrodes with added gold NPs (Figure 2.5a). This was attributed to the low concentration present (0.5 wt%), which did not cause any significant changes. To

investigate if gold NPs had any influence on the band gap values of the photoelectrodes, a Tauc plot was employed (Figure 2.5b). It was determined that the addition of gold NPs did not alter the band gap values of the photoelectrodes, since the same value, i.e. ≈ 3.15 eV was obtained for both samples. Additionally, optical characterisation was also performed using Raman spectroscopy (Figure 2.5c). Independent of the sample, TiO₂ Raman active vibration modes E_g (143 cm⁻¹), A_{1g} (395 cm⁻¹), B₁ (514 cm⁻¹), and an overtone at E_g (639 cm⁻¹) were recorded. The same technique also confirmed the TiO₂ anatase phase for photoelectrodes with and without gold NPs, via the identification of the vibrational mode E_g (143 cm⁻¹). It is noteworthy that lower signal intensity and marginal peak expansion was observed for the photoelectrodes with gold NPs, which was attributed to their addition.^[79] To validate such interactions, measurements were conducted at various points on the surface of the photoelectrodes, with the result that all of them gave the same conclusions (the height for both samples was kept constant during all measurements). Therefore, the results indicated that gold NPs were responsible for a minor increase of crystal imperfections within the framework.^[76] As reported by Li et al.,^[76] these defects could be beneficial with regards to capturing photoelectrons and decreasing charge recombination. Furthermore, since gold is known to exhibit great conductivity properties, its presence in the framework can facilitate photoelectron transfer, which consequently reduces the level of charge recombination.

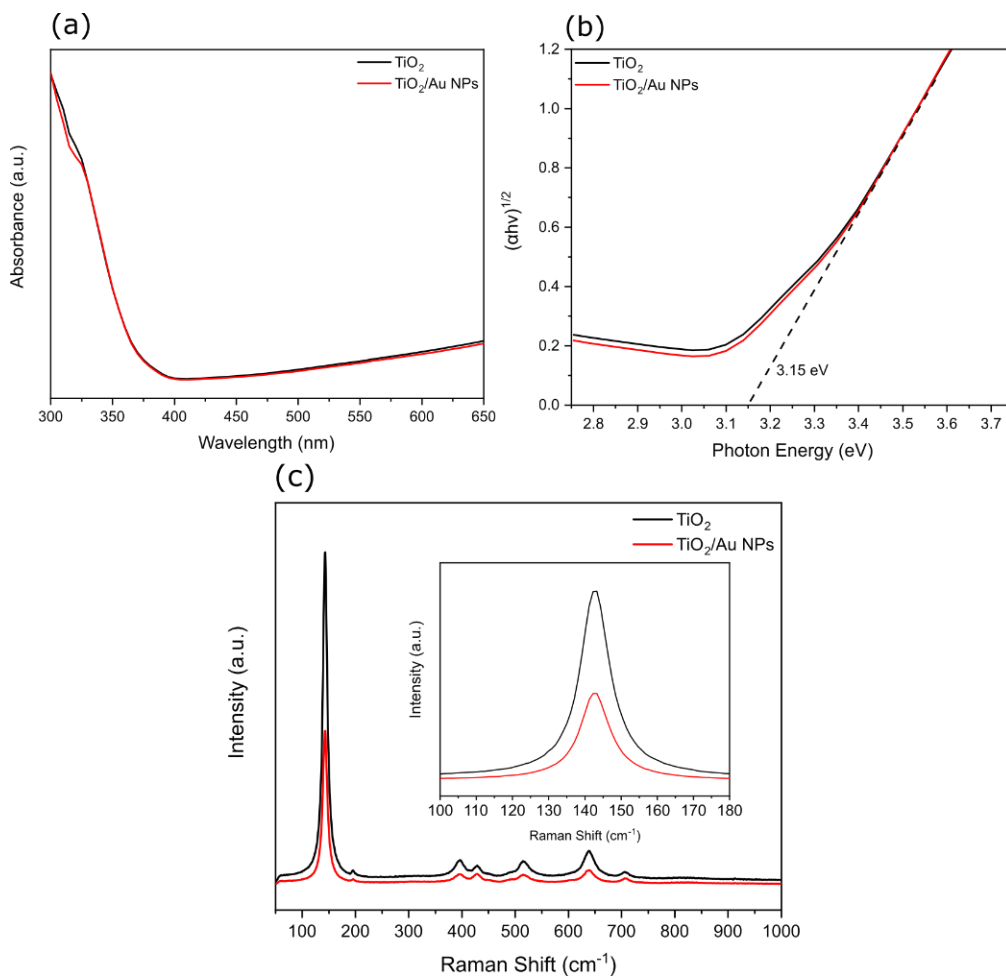


Figure 2.5. (a) UV/Vis absorption spectra for photoelectrodes with and without gold NPs. (b) Tauc plot as calculated from the UV/Vis absorption spectrum indicating their band gap values. (c) Raman spectra for photoelectrodes with and without gold NPs. The inset shows the Raman shift region between 100 and 180 cm^{-1} .

2.3.2 Photovoltaic characterisation

Photoelectrodes containing different sized gold NPs (5, 8, 10 and 12 nm), and a control without them, were assembled into DSSCs and evaluated for their photovoltaic operation under the AM 1.5 standard spectrum conditions. For every fabricated batch, a separate synthesis of Au NPs was performed, including size measurements via TEM. On the other hand, TiO_2 NFs were synthesized in one batch, which was then used for all device fabrications. All steps during repeated fabrications remained

identical. Together with current density-voltage (J-V) plots, external quantum efficiency (EQE) was also measured, which can be seen in Figure 2.6. The corresponding photovoltaic parameters that were obtained from the J-V plots are given in Table 2.1. EQE plots (the ratio of charge carriers accumulated by the solar cell to the number of monochromatic photons that strike the solar cell from outside, not considering photons that reflect) were obtained between the wavelengths of 400 – 800 nm. It is noteworthy that in Table 2.1, only the highest performing DSSCs are tabulated. As is illustrated, the highest performing control DSSCs (no addition of gold NPs) exhibited J_{sc} of 15.8 mA cm^{-2} , a V_{oc} of 757.9 mV, fill factor (FF) of 54.7%, and an overall PCE of 6.5%, respectively. In contrast, the addition of gold NPs improved the photovoltaic parameters of DSSCs, and the optimal size was resultant as 8 nm. The best performing device, containing 8 nm gold NPs, exhibited J_{sc} of 17.3 mA cm^{-2} , V_{oc} of 745.7 mV, FF of 61.8% and PCE of 8%. The enhancement of PCE compared to the control was approximately 18.7%, which was due to better J_{sc} and FF, and is in agreement with the previous studies.^[80,81] The value of J_{sc} improved by 8.7%, and FF improved by 11.5%. The presence of 5 nm sized gold NPs also appeared to have a beneficial effect on the same photovoltaic parameters (J_{sc} and FF). In contrast to this, DSSCs containing 10 and 12 nm gold NPs displayed lower J_{sc} values, while FF was still higher compared to the control devices. The advantage of photoelectrodes containing 5 and 8 nm gold NPs was associated with their favourable surface areas.^[68] As reported in the study of Wang et al.,^[62] the inclusion of gold NPs in the TiO_2 photoelectrodes, generates two features (light-scattering and the LSPR effect) that both have a beneficial impact on the performance of solar cells, resulting in the PCE increase. However, such characteristics are susceptible to the different sizes of gold NPs. Previous studies where gold NPs (0.2 wt%) were added to TiO_2 NPs, have

reported a V_{oc} increase with decreasing particle sizes.^[62] While the results illustrated in Table 2.1 do not show the same trends, the discrepancies were attributed to the different amount of gold NPs added, which influenced the fermi level (E_F) of TiO_2 differently.^[82] Since the band gap values were not influenced by the addition of gold NPs, as discussed previously (Figure 2.5b), such trends were also anticipated. In addition, it would be difficult to observe any influence of such small sized gold NPs, where in other studies bigger sizes were added.^[62]

When compared with DSSCs without gold NPs, their addition noticeably increased FF for all the added sizes. Such a phenomenon has already been reported, where it was attributed to the reduction in charge recombination.^[62,80] The presence of gold NPs leads to longer electron lifetimes (free electrons spend more time in the conduction band (CB)), which is beneficial for solar cells since this reduces the level of charge recombination. Nevertheless, bigger sized gold NPs decrease electron effective lifetime and the recombination resistance, which supports the trends in Table 2.1.^[62] Despite this, compared to the control DSSCs, the total PCE was higher for all gold NPs sizes. Specifically, for 5 and 8 nm sizes this was mainly due to the increase in J_{sc} and FF, while for 10 and 12 nm sizes it was generally due to the better FF. To gain additional information on the trends of J_{sc} , EQE measurements are presented in Figure 2.6b. As anticipated, the addition of 8 nm gold NPs resulted in the highest EQE value of 73%, which is a 13% increase compared to the control DSSCs. Therefore, this suggests an improvement in light harvesting, and results in the overall enhancement of PCE. Additionally, a minor bathochromic shift in the EQE peak maximum can be observed for DSSCs containing gold NPs. This red shift was attributed to the improved light absorption of the combination of gold NPs and dye molecules (N719), where gold NPs caused a slight shift towards the higher band gap

energy levels.^[65] The enhancement of light absorption towards the higher wavelength range has already been reported elsewhere, where gold nanostructures were added to the scattering layer of a solar cell configuration.^[83]

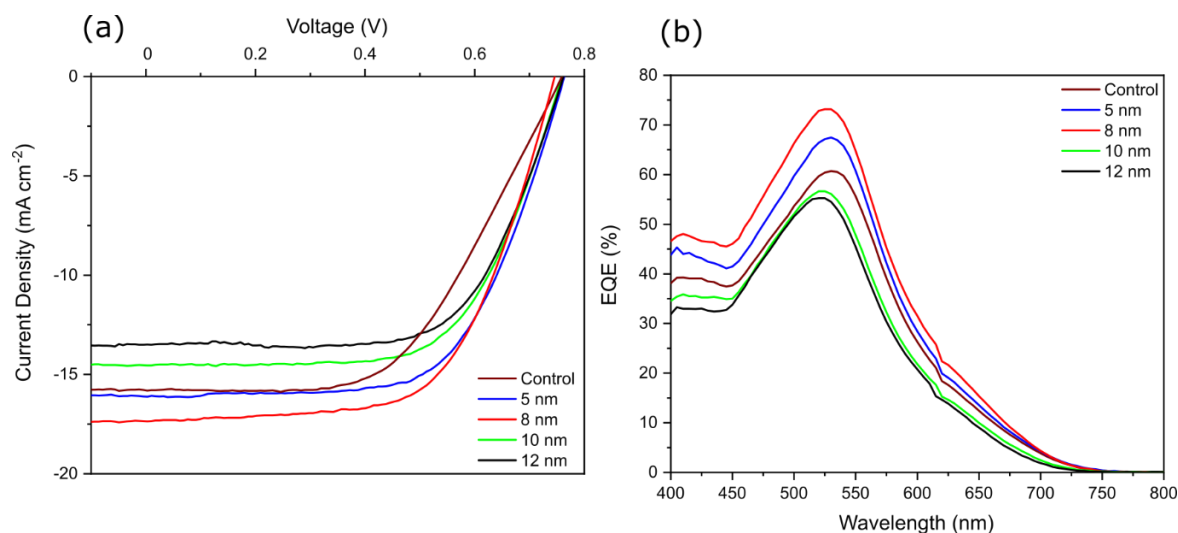


Figure 2.6. (a) J-V results for control and gold NPs containing DSSCs. The characterisation was undertaken under 1.5 AM (air mass) solar irradiation. The J-V curves were obtained by sweeping between 1.0 V and -0.2 V. (b) EQE spectra of control and gold NPs containing DSSCs.

Table 2.1 Photovoltaic parameters extracted from the J-V curves for the highest performing DSSCs. The table shows 5 different devices.

DSSC	J _{sc} (mA cm ⁻²)	V _{oc} (mV)	FF (%)	PCE (%)
Control	15.8	757.9	54.7	6.5
5 nm gold NPs	16.1	763.4	62.9	7.7
8 nm gold NPs	17.3	745.7	61.8	8.0
10 nm gold NPs	14.5	758.9	63.9	7.0
12 nm gold NPs	13.5	761.7	65.6	6.7

To justify the results discussed in this report, five separate batches of DSSCs were fabricated. The average photovoltaic performance, together with their standard errors,

are illustrated in Figure 2.7. Trends in photovoltaic parameters did not change compared to the best performing DSSCs in Table 2.1, indicating high reproducibility of results. The averages are depicted between their maximum and minimum values (J_{sc} , V_{oc} , FF, and PCE) and the standard error has been represented as error bars. While J_{sc} and FF exhibited reasonable low standard error, the values of V_{oc} resulted to slightly fluctuate for all types of DSSCs. This was associated with the nature of iodine-based electrolytes that are known to be evaporative and temperature susceptible. Due to the notable J_{sc} and FF increase, the average PCE for DSSCs with added 8 nm gold NPs was enhanced by 20%.

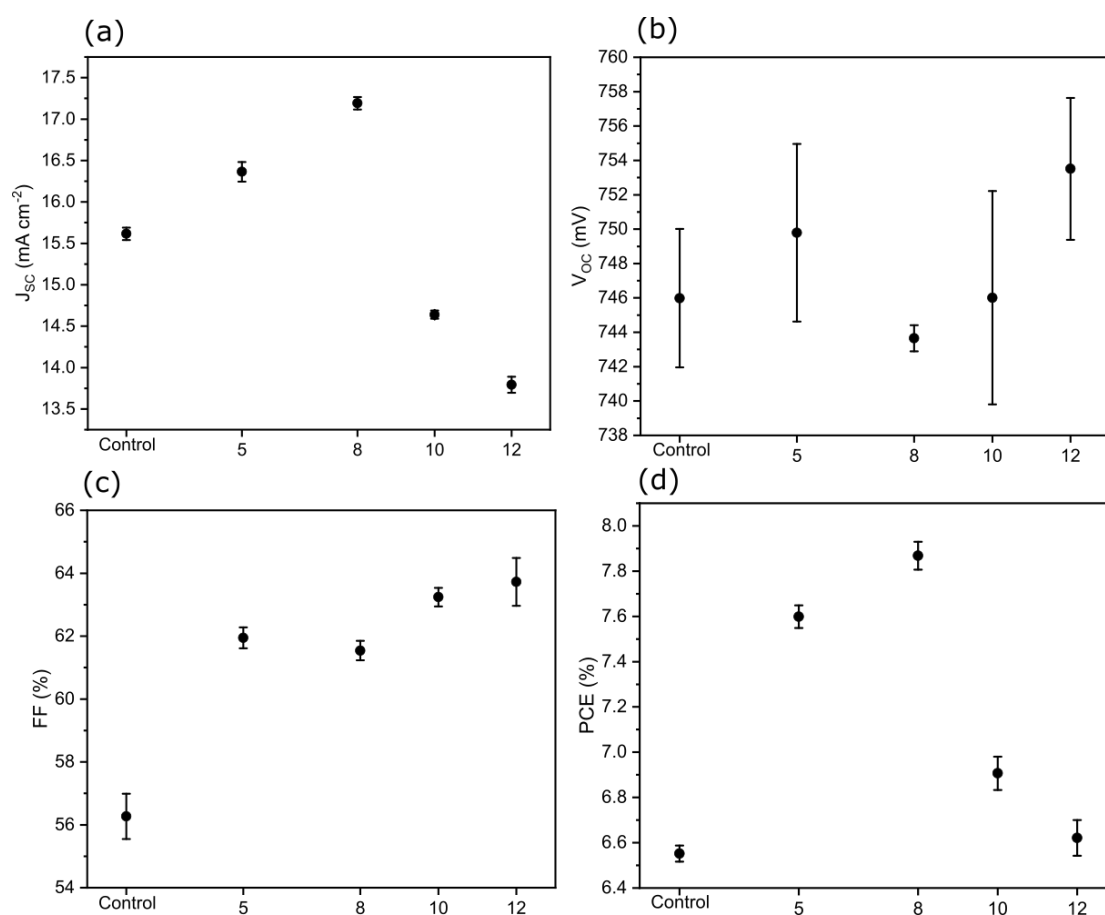


Figure 2.7. The average values for (a) J_{sc} , (b) V_{oc} , (c) FF, and (d) PCE of fabricated DSSCs. The averages were obtained over 5 individual batches of DSSCs and the standard error is illustrated as error bars.

To further investigate trends of photovoltaic parameters, average shunt (R_{SH}) and series (R_s) resistances determined from the J-V curves are presented in Table 2.2. R_s has the main influence on FF, where high values are not advantageous. If R_s is very high, this can also be detrimental to J_{SC} . It was found that for DSSCs containing 5, 8, and 10 nm gold NPs, R_s decreased compared to the control. Among them, the lowest value was determined for DSSCs with 8 nm gold NPs, which agrees well with its highest photovoltaic performance. In contradiction with this, DSSCs containing 12 nm sized gold NPs exhibited the highest R_s . While this did not result in low FF, such a high value influenced J_{SC} and was consequently the lowest. On the other hand, it was reported that gold NPs can display catalytic characteristics.^[84] Therefore, this can also have an influence on R_s , and the decrease may indicate that 5, 8, and 10 nm gold NPs were successful in catalysing the following oxidation reaction (occurs after dye molecules are oxidized and hence have to be reduced to prevent charge recombination).



As the catalytic characteristics of gold NPs are size dependent,^[85] 12 nm gold NPs could have resulted in being less effective. On the other hand, R_{SH} can influence J_{SC} and V_{OC} . Low values of R_{SH} increase power losses due to an alternate current path for the light-generated charge carriers. Therefore, current going through the solar cell is decreased together with voltage from the solar cell. The impact is particularly severe when the generated current of a solar cell is low. Nevertheless, the results illustrated in Table 2.2, did not show any trends in R_{SH} , as the values were scattered within an

order of magnitude. As the results indicate, V_{OC} for all types of DSSCs remained relatively coherent. For that reason, R_{SH} did not have notable influence on the performance, whereas the opposite applies for R_s . Therefore, trends in PCE for DSSCs containing gold NPs, can be together with other factors also attributed to the values of R_s . In addition, characterisation about the dye uptake properties of DSSCs containing different sized gold NPs was also undertaken, as can be seen in Table 2.2. However, results indicate that their addition did not have any influence on dye desorption, since the dye loading of photoelectrodes was within a similar range. These conclusions agree with other studies in the field, where it has been reported that the gold NP size or concentration have little impact on the dye uptake.^[62,80]

Table 2.2 Average R_{SH} and R_s that were determined from the J-V curves for different types of DSSCs.

DSSC	R_{SH} (Ω cm⁻²)	R_s (Ω cm⁻²)	Dye uptake (μg)
Control	365	12.6	135
5 nm gold NPs	765	10.3	130
8 nm gold NPs	433	9.6	132
10 nm gold NPs	530	9.8	131
12 nm gold NPs	826	13.5	132

The addition of below 12 nm gold NPs to the scattering layer of DSSCs was shown to be beneficial and progress was noted in various aspects. As a result, the performance increase for DSSCs was notable and the PCEs were some of the highest ever reported for a pristine TiO₂ NF-based scattering layer. Nevertheless, the performance did not exceed values reported in the study by Chuangchote et al.,^[86] where their highest PCE was 10.3% for a solar cell area of 0.05 cm⁻², and 8.14% for a solar cell area of 0.25 cm⁻². It should be noted that their DSSC configuration exhibited a thick 15 μ m layer of

TiO₂ NPs and a 1 μm thick layer of TiO₂ NFs, which is quite different compared with the thicknesses in this study. This suggests that their main performance enhancement was a result of a NP layer that provided huge surface area for the dye uptake. In addition, Naphade et al.,^[80] also added gold NPs to TiO₂ NFs, which resulted in a PCE of 7.8%, a 15% improvement compared to the control DSSCs (a similar range as reported in this study). However, compared with the work discussed here, they did not mention the gold NPs size-dependent relationship. In this study, an assessment was performed between the precisely controlled < 12 nm gold NP sizes and their impact on the performance of TiO₂ NF based DSSCs, in order to determine the upper and the lower size limits. The results indicate that every size of gold NPs influenced the performance of DSSCs individually. For instance, 5 and 8 nm gold NPs lead to better light harvesting and charge transport characteristics of DSSCs together with lower R_s, which altogether resulted in the increase of J_{sc} and FF. In contrast, DSSCs incorporating 10 and 12 nm gold NPs showed a decrease of J_{sc}, meaning that the light harvesting was not improved in this case. However, for all gold NP sizes, an increase in FF was observed, which points to a reduction in resistive losses. While all DSSCs that contained gold NPs exhibited better PCEs compared to the DSSCs without them, the highest performing varieties included 8 nm sizes. Reasons for this were attributed to the improvement in light harvesting due to the LSPR effect (sensitized photoelectrodes only),^[65] low R_s, better charge carrier dynamics, and improved injection rate.

2.4 Conclusion

In this chapter, the addition of below 12 nm gold NPs to the scattering layer of a DSSC photoelectrode has been presented. DSSCs containing different sizes of gold NPs showed improved overall PCEs. The best size of gold NPs for photovoltaics was determined to be 8 nm, since PCE increased as a result of higher J_{sc} and FF, which was ascribed to better light harvesting, lower R_s , and improved charge transport and generation rate. The highest PCE that was obtained was in the range of 8%, which, when compared with DSSCs that did not contain any gold NPs, is a 20% improvement. The results clearly indicate that the size control over gold NPs is essential for the performance improvement of DSSCs. It is believed that the same conclusions can be extended towards other types of photovoltaic cells, particularly perovskites, whereby the use of gold NPs has already been reported, however their size was not controlled. In addition, other classes of nanomaterials can also improve the performance of solar devices, and this is explored in chapter 3.

Chapter 3

The influence of lithium and lanthanum on the performance of n-i-p solar cells

3. The influence of lithium and lanthanum on the performance of n-i-p solar cells

3.1 Introduction

Regardless of the extensive employment of a TiO₂ semiconductor for various types of applications, for example, self-cleaning windows,^[87] supercapacitors,^[88] and battery electrodes,^[89] its optical properties are not ideal for use as a light absorbing material, where the high range of the solar spectrum has to be covered. Therefore, much investigation has been focused on materials modifications.^[90] Specifically, as a result of a wide band gap, TiO₂ can only absorb the UV region of the electromagnetic spectrum. Since only 4% of such high energy light reaches the surface of the Earth, this characteristic presents a considerable disadvantage for photocatalysis (water splitting and dye degradation, etc.).^[91,92] Despite the band gap change with different crystal structures of TiO₂, where the most common ones include metastable anatase (tetragonal), stable rutile (tetragonal), and brookite (orthorhombic), they all are active only in the UV region (<400 nm). Moreover, these phases are known to exhibit different charge transport characteristics, and the most relevant crystal phase for solar cells is the anatase phase.^[90]

To improve the charge transport properties of a TiO₂ layer, researchers have investigated different morphologies beyond the most widely used TiO₂ NPs. The most promising ones include 1D nanostructures (directionality), that have previously been shown to decrease the charge recombination levels, due to a decrease of material's defects, for instance grain boundaries.^[93–95] Therefore, the charge transport rate resulted in being more rapid when compared with NPs, which was mostly due to the

decreased free electron scattering. However, 1D nanostructures possess low BET surface areas, an attribute that is not favourable for DSSCs as the performance heavily relies on dye uptake. While in the literature there are many reports addressing this issue, for instance, the fabrication of photoelectrodes that consist of NPs and NFs, doping has also been a very popular approach.^[90] Doping of TiO₂ can be performed through the addition of cations or anions with the aim of modifying the electronic properties. Here, the type of ion that is added has a specific effect on the material's characteristics and should, therefore, be chosen based on the modifications that are required. For substitutional doping of TiO₂, Ti⁴⁺ has to be replaced with a cation of a similar radius; the same also applies for an anion (O²⁻), where a non-metal has to be used. Accordingly, different candidates have been used based on the modifications that were required for a particular application. For example, in the field of organic dye degradation, lanthanum compounds have been used to modify TiO₂ as they have been shown to improve its photocatalytic properties.^[96] Particularly, the absorption properties of TiO₂ were enhanced by lanthanum treatment, which was attributed to the formation of oxygen vacancies. This phenomenon was explained by the formation of La-O bonds, which compared to Ti-O bonds exhibit stronger chemical bonding.^[97] Additionally, the formation of oxygen vacancies also resulted in the improved charge transport ability of the material.^[97] Since 1D nanomaterials exhibit low BET surface areas, treating them with lanthanum compounds can result in a better dye uptake, which, together with an improved charge transport ability, can be beneficial for DSSCs. Previous studies have also shown that the addition of lithium to TiO₂ can improve conductivity and charge densities.^[90] Li⁺ ions have an influence on the CB edge of TiO₂, which results in improved electron injection and transport.^[98] Since TiO₂ NFs have not been yet treated with lanthanum or lithium cations (this was only reported for

TiO₂ NPs), such additions could show promise within 1D nanomaterials. Moreover, nanostructuring can show influence on the physical and optical characteristics of metal oxide semiconductors, therefore combining nanostructuring with cationic treatments is important to study. In the past decade, PSCs have been an important topic of interest because immense progress in photovoltaic performance has been demonstrated.^[99] Investigations of a n-type (electron transport) layer have mostly focused on NPs, but other nanostructures have not been so widely covered.^[100] One of the first reports of using TiO₂ NFs in a solar cell configuration was performed by Boix et al.,^[101] where research involved directly electrospinning them on a blocking TiO₂ layer. Doping TiO₂ NFs with other elements, (e.g. lead) was reported by Wu et al.^[102], while Hong et al.^[103] used gold instead. Carbon nanotubes (CNTs) in combination with TiO₂ NFs were also employed as a mesoporous layer in a PSC configuration, which resulted in a notable performance improvement.^[104,105] In contrast to this, lithium doping of TiO₂ NPs is well established within PSCs, as it reduces electronic trap states, resulting in enhanced charge transport characteristics.^[98] However, no reports exist in the literature where TiO₂ NFs treated with lanthanum or lithium were used as an electron transport layer.

In chapter 2, gold NPs were synthesized and separately added to TiO₂ NFs, which were then used for DSSCs. Since this procedure requires two steps, where already-formed gold NPs are added to produce TiO₂ NFs, increased production costs can be related to such a procedure, influencing the total price of DSSCs. To avoid this price increase while maintaining high solar cell efficiency, cationic dopants can be directly added to the TiO₂ sol-gel precursor solution for NF production, as has been explored here in chapter 3. Namely, lithium and lanthanum salts were added to the precursor solution for electrospinning, in order to treat formed TiO₂ NFs in one step, consequently decreasing the cost of their production. Therefore, such an approach

can result in more economically viable and industrially feasible production methods. 1D nanostructure materials were combined with metal dopants to exploit the advantages of both. The resulting materials, that are labelled herein as lanthanum or lithium treated TiO₂ NFs, were characterised with several techniques. Spectroscopy methods, such as XPS, XRD, UV/Vis absorbance spectroscopy, and Raman spectroscopy, were implemented to characterise elemental and optical properties, while surface area and porosity modifications were investigated with the BET method. Additionally, the morphology of TiO₂ NFs before and after the treatment was investigated by SEM and TEM. Solar cells (DSSCs and PSCs) were also fabricated, where for DSSCs, TiO₂ NFs were implemented as a light-scattering layer, as opposed to PSCs, for which they were used as a mesoporous layer. The employment of 1D nanomaterials treated with lanthanum or lithium for solar cells, is the first example of their use for such an application. Here, a procedure on how to treat TiO₂ NFs with cationic dopants in one step together with meticulous characterisation of their properties is presented. Finally, the performance of the two types of solar cells containing such materials, is investigated.

3.2 Experimental section

All chemicals that were used for this work were purchased from Sigma Aldrich (UK). No further purification was undertaken for the obtained chemicals.

3.2.1 Preparation of TiO₂ NF precursor solutions

The sol-gel precursor solution for control TiO₂ NFs (no addition of metals salts) was prepared as previously described in section 2.2.2. The lanthanum treated TiO₂ NFs were prepared by separately dissolving lanthanum trichloride heptahydrate (99.999% trace metals basis) in 1 mL of absolute ethanol by sonication. Following the complete solvation, the solution of lanthanum trichloride heptahydrate was added dropwise (while stirring) to the sol-gel precursor solution (PVP in ethanol) for control TiO₂ NFs, and was left stirring for 24 h. Afterwards, 2.5 mL of tetrabutyl titanate was added in moderation, with additional stirring. The precursor solution for lithium treated TiO₂ NFs was prepared by adding 1 mol% of lithium ethanate (>99% anhydrous) to the sol-gel solution of dissolved PVP in absolute ethanol, followed by 24 h stirring. Tetrabutyl titanate was then slowly added with an additional few hours stirring. The two prepared sol-gel precursor solutions were subsequently used for electrospinning, which was achieved via the parameters noted in chapter 2.2.2. Finally, the obtained TiO₂ NFs underwent a heating step at 500 °C for a few hours.

3.2.2 Preparation of TiO₂ NF photoelectrodes

The TiO₂ NF photoelectrodes used for DSSCs were prepared as previously described in section 2.2.3, and lanthanum or lithium treated TiO₂ NFs were implemented for a particular type of device. The fabrication procedure for DSSCs was carried out as described in section 2.2.4.

3.2.3 Fabrication of perovskite solar cells

To deposit a mesoporous layer, a NF paste was first made by mixing the appropriate type of TiO₂ NFs with ethanol (30 mg mL⁻¹). The mixture then underwent sonication until no solid agglomerates of TiO₂ NFs remained, which took approximately 2 h. However, the amount of time required to obtain a uniform solution depends on the sonication power. Subsequently, terpineol (4.9 g for each 1 g of TiO₂ NFs) was added to the mixture, followed by an additional 30 min sonication. To prepare photoanodes for PSCs, commercially available FTO glass slides were etched with 2 mol/L hydrochloric acid and zinc metal, followed by sonication in 5 different solvents for 10 min each, including: water solution of a detergent, deionized water, acetone, ethanol, and isopropanol. Cleaned substrates were then exposed to oxygen plasma for 10 min and immediately afterwards, a transparent layer of TiO₂ NPs was deposited from a 1-butanol 0.1 mol/L solution of diisopropoxytitanium bis(acetylacetonate) (75 wt% in 2-propanol). The spin coating parameters included 3000 RPM for 20 sec. After the deposition, the glass slides were transferred onto a hot plate (2 min), which was set to 150 °C and in air. To ensure, that the compact layer was without pinholes, the deposition was repeated two more times. Since the most favourable TiO₂ crystal structure for solar cells is the anatase phase, the glass slides underwent pyrolysis treatment at 500 °C (50 °C min⁻¹) for 25 min. A mesoporous layer was deposited from the previously described NF paste on top of a compact layer at 4000 RPM for 30 sec. The glass slides were then immediately transferred onto a hot plate and heated to 500 °C (50 °C min⁻¹) for 25 min. To deposit a perovskite layer, the glass slides were subsequently moved to a glovebox. The precursor solution was prepared as reported by Ahn et al;^[106] in summary, 461 mg of lead diiodide and 159 mg of methanamine hydriodide were mixed with 600 mg of dimethylformamide and 78 mg of dimethyl

sulfoxide solvents. These were stirred for 1 h at 65 °C until the solution became clear. To remove any agglomerates, the solution was filtered prior to the deposition. A methylammonium lead iodide layer was deposited via spin coating the filtered solution on a transparent layer of TiO₂ films at 5000 RPM for 30 sec. While the glass slide was spinning for 7 sec, 0.5 mL of ethoxyethane was slowly added. The glass slide was then placed on a hot plate at 65 °C for 2 min and 100 °C for 10 min, forming a solid and uniform layer of CH₃NH₃PbI₃. A p-type material was made by mixing PTAA and methyl benzene (10 mg mL⁻¹), followed by stirring until no solid traces remained (1 h at 65 °C). Other compounds were subsequently added to the same solution, namely 7.5 µL bis(trifluoromethylsulfonyl)amine lithium salt (Li-TFSI)/acetonitrile (170 mg mL⁻¹) and 4 µL of 4-(1,1-dimethylethyl)-heptane, which were left stirring for another few minutes. The metal counter electrode was added via thermal evaporation of gold (80 nm).

3.2.4 Details of instrumentation used

UV/Vis, TEM, XRD, XPS, and Raman spectroscopy characterisation was performed using the instruments and methods described in section 2.2.5. SEM characterisation was performed with a JEOL JSM-6301F instrument. Photovoltaic characterisation was performed using the equipment and methods described in section 2.2.6.

3.3 Results and discussion

3.3.1 Materials characterisation

Potential changes in materials characteristics of treated TiO₂ NFs compared with the control (untreated) were investigated using SEM, which is illustrated in Figure 3.1. Different types of TiO₂ NFs are presented after the heating step that took place at 500 °C. Their length results varied across sizes up to at least ≈20 μm. Longer length sizes were difficult to obtain due to breakages of NFs, which is a consequence of the heating step that is necessary for the removal of a polymer (in this work PVP was used).^[107] On their surfaces, no visible defects were noticed. Despite the addition of metal salts, no changes in morphology or diameter sizes were observed (Figures 3.1a, c, and e). It was determined that their diameter was in the range of ≈120 nm. Structural characteristics were further analysed with HR-TEM and all types of NFs were evaluated as illustrated in Figure 3.1b, d and f. TiO₂ NFs were assembled from many TiO₂ NPs that constituted a 1D nanostructure. In spite of the addition of metal salts to the precursor solution, no evidence of their metal oxides, for instance Li₂O (for lithium salt) or La₂O₃ (for lanthanum salt), was identified. This was attributed to their low concentration (1 mol%). Crystal phases of different types of TiO₂ NFs were characterised through the distance between the lattice planes, which were identified to be 0.35 nm (inset of Figures 3.1b, d, and f), where the distance did not change upon the presence of lanthanum or lithium salts. The highly crystallized areas of the three types of NFs also had a comparable outline. It was determined that such values were indicative of the (101) plane of the anatase TiO₂.^[108] Furthermore, selected area electron diffraction (SAED) was also implemented to further characterise their nature. Figure 3.2 shows the pattern that was obtained, with bright spots clearly visible and

indicating good crystallinity. The bright spots on a SAED pattern are a result of crystal diffraction, which is evidence of the material's crystallinity. The lattice spacing values (d-spacing) were measured and matched with the anatase phase of TiO_2 .

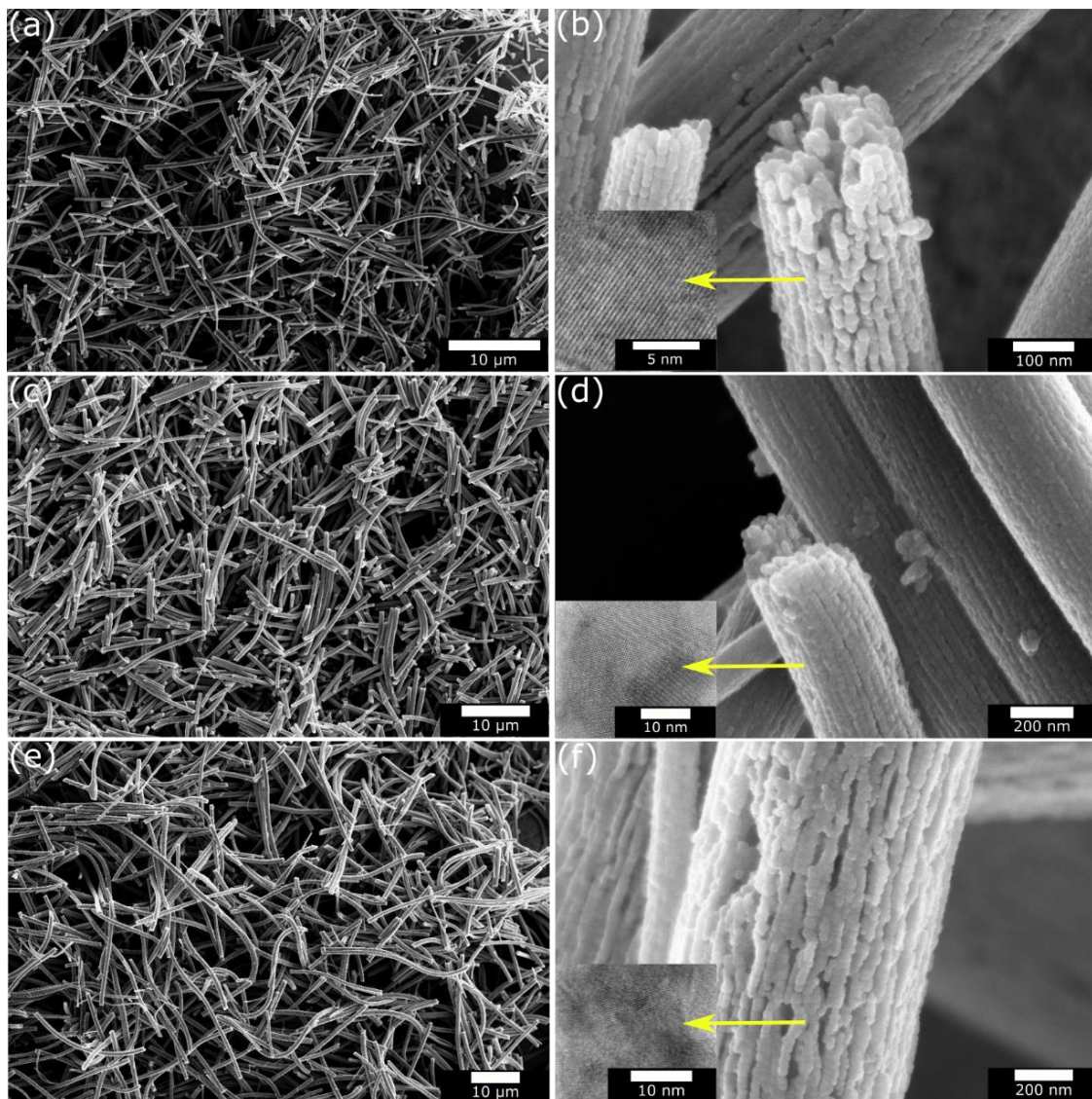


Figure 3.1. Top-view SEM of (a) control, (c) lanthanum treated, and (e) lithium treated TiO_2 NFs demonstrating their morphology characteristics. HR-SEM of (b) control, (d) lanthanum treated, and (f) lithium treated TiO_2 NFs with HR-TEM insets illustrating their lattice patterns with inter-planar spacing of 0.35 nm.

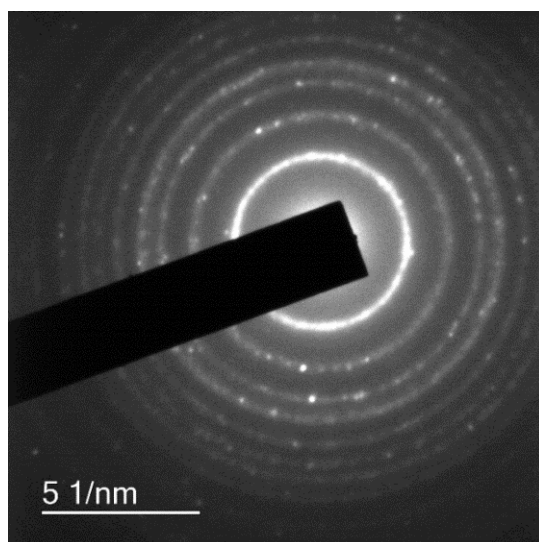


Figure 3.2. A SAED pattern for TiO₂ NFs.

Since neither SEM nor TEM were successful in detecting lithium or lanthanum in TiO₂ NFs, additional methods were implemented. Specifically, for elemental identification XPS, a characterisation technique known for its surface sensitivity was employed. Figures 3.3a, b, and c show the XPS spectra for a titanium element (control, and lanthanum or lithium treated TiO₂ NFs), which gave Ti2p peaks with notably split spin-orbit components. The Ti2p_{3/2} and Ti2p_{1/2} peaks were located at 458.4 eV and 464.1 eV, respectively. The position of the binding energies indicated that titanium was in the +4-oxidation state, which is consistent with TiO₂ for all types of NFs. The lanthanum element, where relevant, was additionally detected, due to the La3d region having significant split spin-orbit components that are further split by multiplet splitting. These are referred as satellite peaks. The main peaks were located at 834.6 eV, which is associated with La3d_{5/2}, and at 851.4 eV, associated with La3d_{3/2} (Figure 3.3d). From the position of these peaks, it was determined that lanthanum was in the oxidation state of +3, which indicates a La₂O₃ compound. Moreover, the XPS results indicated that the crystal structure of TiO₂ remained intact with almost no substitutional

or interstitial doping of La^{3+} , and that La_2O_3 was only dispersed on the NFs. This observation was further investigated via XRD, as discussed below (Figure 3.4a). Furthermore, for lithium treated TiO_2 NFs, lithium was detected on their surfaces, as seen in Figure 3.3e. Since the signal was very weak, the same binding energy region was compared to the control. While a weak signal for a $\text{Li}1s$ XPS region was observed for lithium treated TiO_2 NFs, nothing was present in that region for the control. Consequently, this indicates the existence of lithium on the surface of the NFs, where it was in the form of Li_2O . Since lithium is one of the lightest elements, it is considered challenging to detect using spectroscopy techniques. Therefore, the signal presented herein can be acknowledged as considerable, verifying that lithium was present. Moreover, compared with other reports, for instance, Giordano et al.,^[98] the detection range in Figure 3.3e is very clear. For all types of TiO_2 NFs, no peaks at binding energies that would be associated with Ti^{3+} surface states (linkage with oxygen vacancies), were detected, which concurs with that reported in the cited work.^[98] Despite this, they investigated the formation of oxygen vacancies from the interactions between lithium and oxygen based on the $\text{O}1s$ spectrum, and claimed that their results might suggest oxygen vacancy formation. It is noteworthy that using an $\text{O}1s$ spectra for the evaluation of interactions can be considered unreliable, since if samples are not treated with the appropriate equipment, there is a high chance of oxygen contamination. Based on the $\text{O}1s$ spectra in this study for lithium or lanthanum treated TiO_2 NFs, potential interactions could be noticed, however the outcomes were considered as uncertain, because lithium or lanthanum elements could be contaminated by the atmospheric oxygen.

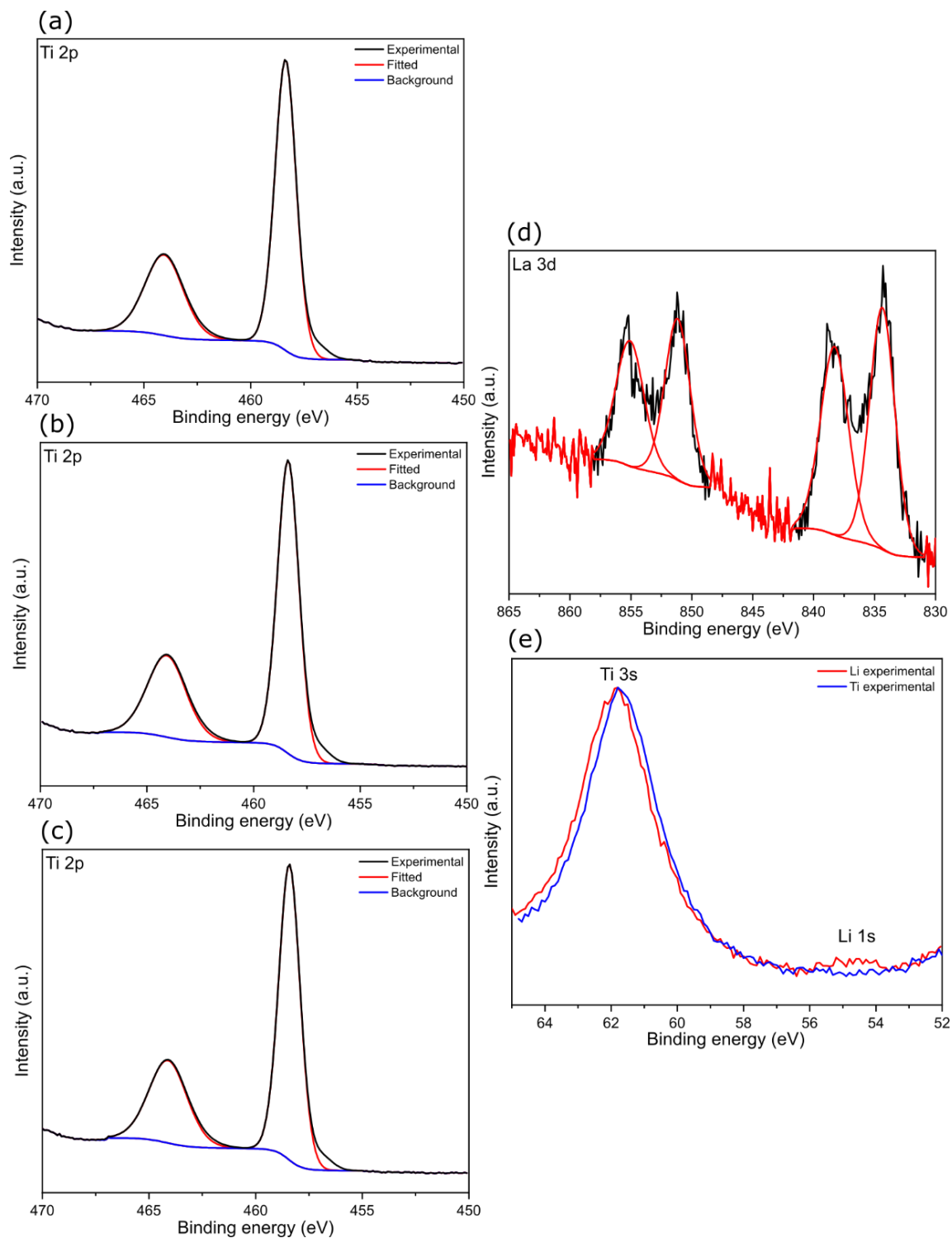


Figure 3.3. Ti 2p XPS spectra for (a) control, (b) lanthanum, and (c) lithium treated TiO₂ NFs. (d) Lanthanum 3d spectrum for lanthanum treated TiO₂ NFs confirming the detection of a lanthanum element. (e) Lithium 1s spectra for lithium treated TiO₂ NFs, compared with the identical region of control TiO₂ NFs, confirming the detection of a lithium element.

To evaluate the influence of lanthanum and lithium treatment on the crystal phase of TiO_2 , XRD characterisation was carried out. Figure 3.4a illustrates XRD patterns for individual TiO_2 NFs. Since the calcination step was performed at $500\text{ }^\circ\text{C}$, NFs showed the signals of the anatase phase of TiO_2 . The latter phase is as a result of the beneficial charge transport characteristics, ideal for use in photovoltaics.^[90] The addition of metal salts had an influence on crystallinity, and lanthanum treated TiO_2 NFs exhibited broader peaks, which is an indication of an inferior crystalline material. On the other hand, lithium treated TiO_2 NFs showed the opposite trend and were therefore considered as more crystalline (well-defined XRD peaks with lower fwhm values). As discussed previously, XPS results indicated that lanthanum (lanthanum treated TiO_2 NFs) was oxidized to La_2O_3 . However, the latter phase was not detected via XRD, which was attributed to its low concentration (1 mol% of lanthanum precursor was added). To further support the assumption from the XPS discussion that no lanthanum insertion/substitution occurred, the positions of the peaks were investigated from the corresponding control and lanthanum treated TiO_2 NF XRD patterns. The incorporation of dopants with larger ionic radii into a crystal structure results in a unit cell expansion. This then causes a shift of the peaks in an XRD pattern to lower 2θ angles.^[90] For the samples in this study, it was concluded that no shifts appeared upon lanthanum treatment, suggesting that the crystal lattice of TiO_2 remained unchanged and thus no La^{3+} substitution with Ti^{4+} occurred. Moreover, lattice parameters and volumes for all types of TiO_2 NFs were also determined, as illustrated in Table 3.1. Since discrepancies resulted to be within an error range and thus no expansion of a unit cell was recorded, this further suggested that no modification of the crystal structures occurred. This phenomenon can be explained by the difference in the ionic radius, where La^{3+} (0.103 nm) is considerably larger than Ti^{4+} (0.061 nm). Crystallite

sizes of TiO₂ NFs were determined using the Scherrer equation. For that purpose, (011) and (020) planes of the anatase phase located at 11.37 and 21.71 2 θ degrees respectively, were used. It was determined that compared with the control, lanthanum treated TiO₂ NFs exhibited 43% smaller crystallite sizes. This was attributed to La³⁺ ions, which were not present in the crystal lattice (as discussed earlier) and consequently, did not induce any defects, such as grain boundaries, that can hamper the growth of crystals.^[109] Contrary to this, for lithium treatment the crystallite sizes increased (16%) when compared to the control. However, the location of the TiO₂ anatase peaks remained the same as for lanthanum treatment, indicating that no structural modifications took place. While the XRD peaks for control and lanthanum treated TiO₂ NFs matched the standard anatase TiO₂ phase, additional peaks appeared for lithium treated TiO₂ NFs, which were not related to the same phase. It was determined that those signals corresponded to the rutile phase of TiO₂. Considering that all types of NFs were prepared in the same way, including the calcination step at 500 °C, the identification of the rutile phase for lithium treated TiO₂ NFs suggested that the presence of lithium salts promoted the development of the latter phase at lower temperatures (the rutile phase usually forms between 600-800 °C). While this has not yet been reported for TiO₂ NFs prepared via the procedure as described herein, there are reports of lithium doped TiO₂ NPs containing both phases.^[110] It should be noted that for all types of NFs, signals related to the anatase phase deviated to lower 2 θ angles in comparison to the peaks of a reference TiO₂ anatase phase (Figure 3.4). This can be explained by unit cell expansion, which occurred due to the nanostructuring of TiO₂ (NPs versus NFs).

Table 3.1 The values of lattice parameters and volumes for the control, lanthanum, and lithium treated TiO₂ NFs.

	Lattice parameter a (Å)	Lattice parameter c (Å)	Lattice volume (Å³)
Control	3.78	9.49	135.60
Lanthanum treated TiO₂ NFs	3.80	9.46	136.33
Lithium treated TiO₂ NFs	3.79	9.43	135.24

Optical properties of TiO₂ NFs upon metal salt treatment were investigated using Raman spectroscopy. The results for control and lanthanum or lithium treated TiO₂ NFs are presented in Figure 3.4b. The vibration modes assigned to the anatase phase of TiO₂ for control NFs, namely E_{1g}, E_{2g}, A_{1g}, B₁, and E_{3g} were identified at 142.4, 195.1, 394.7, 515.6, and 637.6 cm⁻¹.^[73] As revealed by the XRD measurements (Figure 3.4a), the same phase was also present for lanthanum treated TiO₂ NFs, which was also confirmed by the Raman spectra (Figure 3.4b). However, the vibration modes, for instance E_{1g} (143.5 cm⁻¹), B₁ (517.7 cm⁻¹), and A_{1g} (398.8 cm⁻¹) exhibited a slight shift compared to the control. These shifts for a particular vibration mode, revealed further information about the metal salt interactions. For example, the shift of the main anatase mode (E_{1g}) was a result of the crystallite size difference.^[109] Specifically, as already observed by XRD (the Scherrer equation), lanthanum treatment reduced crystallite sizes, which on the Raman spectra resulted in the shift to higher wavenumbers by ≈1.1 cm⁻¹, consistent with other reports.^[109] The same vibration mode (E_{1g}), also displayed higher fwhm (inset of Figure 3.4b) compared to the control, which is an additional characteristic of the crystal size contraction.^[111] As discussed by Tanyi et al.,^[109] such a feature can also be due to the increase of oxygen vacancies. Since this was detected only for lanthanum treated TiO₂ NFs, it can be associated with their formation. On the other hand, the results of the vibration modes

of the anatase phase for lithium treated TiO₂ NFs are comparable with the control. In spite of that, an additional signal appeared that was not detected for the control or lanthanum treated TiO₂ NFs (Figure SI1 in the Supporting Information). Specifically, a weak vibrational mode (E_g) at 445.3 cm⁻¹ appeared. This signal was assigned to the rutile phase of TiO₂,^[112] which corresponds to the XRD analysis from above.

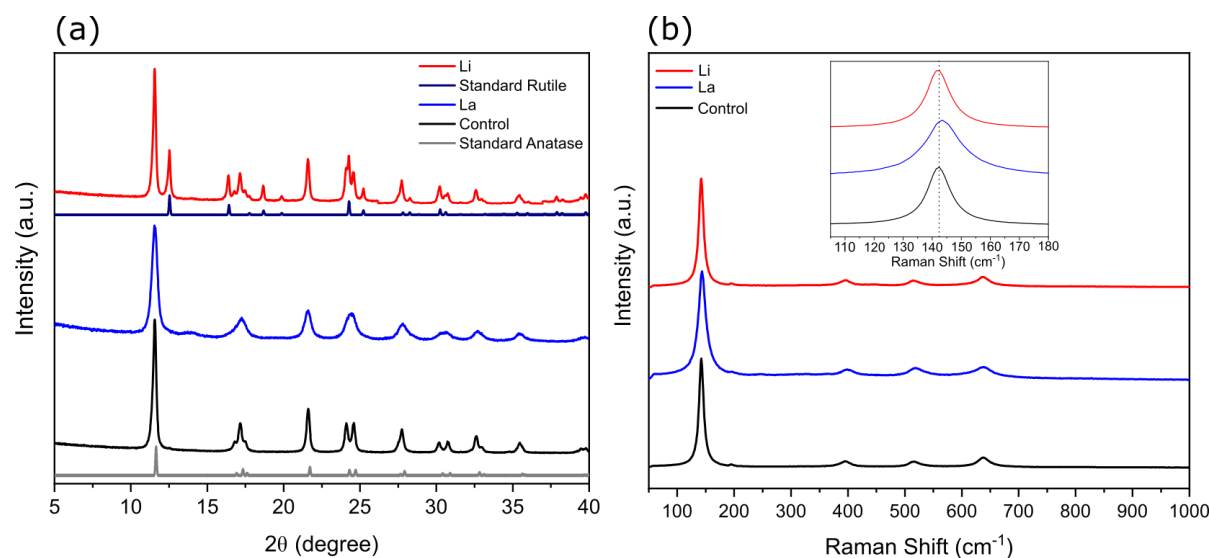


Figure 3.4. (a) XRD patterns for lithium (red), lanthanum (blue), and control (black) TiO₂ NFs. The standard rutile and anatase TiO₂ crystal phases are shown in dark blue and grey, respectively. (b) Raman spectra for lithium (red), lanthanum (blue), and control (black) TiO₂ NFs, together with the inset in the region between 110 – 180 cm⁻¹.

It was reported that the addition of metal salts to TiO₂ can influence the band gap of the material.^[113] Therefore, UV/Vis measurements were performed for TiO₂ NFs to investigate whether lanthanum or lithium treatment caused such changes (Figure 3.5). A typical method to determine a band gap is based on a Tauc plot, which is illustrated for all types of TiO₂ NF photoelectrodes in the inset of Figure 3.5a. It should be noted that data obtained from Figure 3.5 is presented in Table 3.2. By implementing this technique, a band gap of ≈3.1 eV was determined for both the control and lanthanum

treated TiO₂ NFs, implying that La³⁺ did not induce any changes. Contrary to this, for lithium treated TiO₂ NFs the determined band gap was ≈2.9 eV. Since this is an evident decrease compared with the control, Li⁺ ions were attributed as the cause for such a bathochromic shift in the absorbance. As discussed earlier, lithium treated TiO₂ NFs consisted of two phases (anatase and rutile), compared to the single anatase phase in the control and lanthanum treated TiO₂ NFs. Since the anatase phase (3.2 eV) has a wider band gap in comparison to the rutile phase (3.0 eV), the presence of the latter phase was concluded to be the origin for the red shift. In addition, UV/Vis measurements were also performed for TiO₂ NF powders as shown in Figure 3.5b. From Tauc plots (the inset of Figure 3.5b), it was determined that no considerable changes occurred in the band gap values (Table 3.2) compared with the TiO₂ NF photoelectrodes, further confirming the trends discussed before. The band gaps of the TiO₂ NFs discussed herein are slightly lower than what is commonly reported for bulk TiO₂.^[114] The reason for this is related to the nanostructuring (surface effects and quantum confinement), and consequently, NPs and NFs have different surface energy.^[115]

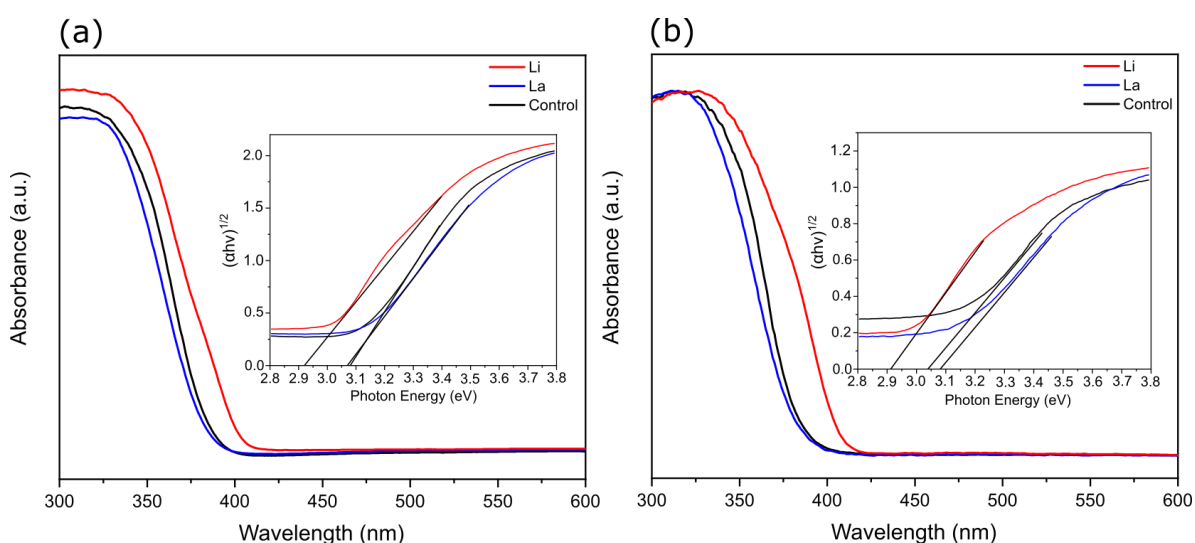


Figure 3.5. Graph showing the UV/Vis absorption spectrum of (a) control, lanthanum, and lithium treated TiO₂ NF photoelectrodes together with Tauc plots as inset that

were used for a band gap determination. (b) The same results as under (a) for TiO₂ NF powders.

Table 3.2. Band gap for control, lanthanum, and lithium treated TiO₂ NF photoelectrodes and powders as determined from Tauc plots in Figure 3.5.

Band gap	Control	Lanthanum treated TiO₂ NFs	Lithium treated TiO₂ NFs
Photoelectrodes	3.08	3.07	2.92
Powders	3.05	3.07	2.92

Furthermore, nanostructuring also affects other properties, for example, the BET surface area, where it is well known from literature that NFs exhibit lower values compared to NPs.^[116] Such characteristics of NFs are notoriously detrimental for their implementation in DSSCs due to the resulting poor dye absorption, which hinders optoelectronic performance. To resolve these drawbacks, doping was shown to be advantageous, since particular metal elements can enhance the BET surface area.^[117] To examine the influence on these values by lanthanum and lithium treatment of TiO₂ NFs, adsorption measurements were performed with nitrogen (N₂) being used as a carrier gas. Physisorption isotherms that were obtained from the nitrogen uptake under standard temperature and pressure (STP) conditions are illustrated in Figure 3.6. From them, BET surface area and porosity were determined, as presented in Table 3.3. Considering that TiO₂ P25 NPs are one of the most commonly used photoelectrode material for DSSCs, they were also included to serve as a comparison between control TiO₂ NFs and P25 NPs, which confirmed the assumptions of the BET surface area increase with NPs; they exhibited 17.4 m²/g higher values. The same finding was also identified for porosity, as the one of NPs was higher by more than 50%. Contrarily, a substantial increase in the BET surface area occurred for lanthanum treated TiO₂ NFs,

which notably surpassed the value for the control TiO₂ NFs and even exceeding that of P25 NPs. In contrast, such an increase did not evolve for the porosity, which was lower than that for P25 NPs. While the addition of La³⁺ ions proved to be beneficial, the same did not unfold for Li⁺ ions. Namely, lithium treated TiO₂ NFs had the lowest BET surface area and porosity among all candidates. The BET surface area decreased noticeably compared to the control TiO₂ NFs, and nearly 3-fold compared to lanthanum treated TiO₂ NFs. An even greater decline was recorded for porosity, as it was 19-fold lower than for the control, and 24-fold lower than for lanthanum treatment. Such high BET surface area enhancement for lanthanum treated TiO₂ NFs may be justified from the XRD results (Figure 3.4a), where it was shown that their crystallite size diminished, which consequently can result in particle aggregation leading to the formation of nanopores.^[118,119] Other explanations of such trends can also include the defective nature of nanocrystals, since imperfections can influence the BET surface area and porosity of the material.

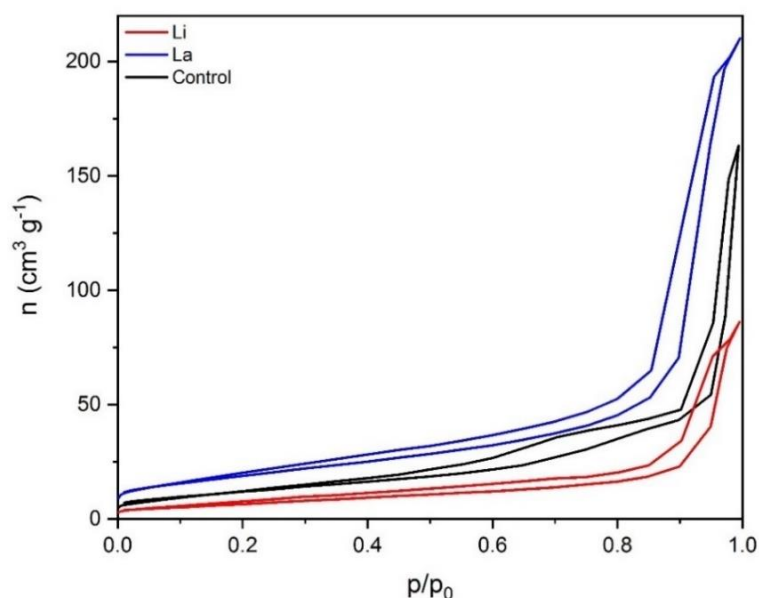


Figure 3.6. Nitrogen adsorption isotherms for control, lanthanum, and lithium treated TiO₂ NFs. (*n* indicates the quantity of nitrogen uptake at 0 °C and 101.325 kPa (standard temperature and pressure conditions)).

Table 3.3. The BET surface area and porosity for different types of TiO₂ NFs as determined from Figure 3.6. As a reference, P25 TiO₂ NPs are also given.

	BET surface area (m ² g ⁻¹)	Porosity (cm ³ g ⁻¹)
Control	45.6	0.252
Lanthanum treated TiO ₂ NFs	70.0	0.325
Lithium treated TiO ₂ NFs	25.0	0.0133
P25 TiO ₂ NPs	63.0	0.551

3.3.2 Photovoltaic characterisation

Synthesized TiO₂ NFs were additionally characterised for their optical characteristics, by implementing them in solar cells that were fabricated following the procedure described in the experimental section (3.2). Figure 3.7 shows an illustration of a DSSC that was fabricated for this study, with the main parts being labelled accordingly.

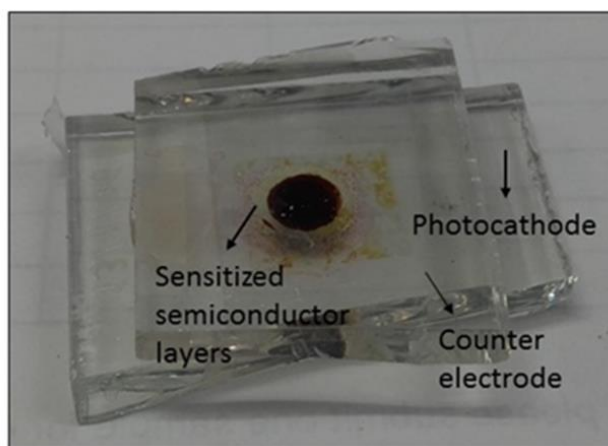


Figure 3.7. An illustration of a DSSC that was used for the purpose of this study. The main parts of the device are labelled on the figure.

In addition, PSCs were also assembled and characterised under one-sun solar conditions. Schematics of both types of solar cells were identified from their SEM cross-sections. Figure 3.8a shows a DSSC device configuration, which consisted of a

transparent layer and a light-scattering layer. The former layer included TiO₂ NPs, while the latter layer contained TiO₂ NFs. Both of them were measured, and it was determined that their thicknesses were $\approx 8 \mu\text{m}$ and $\approx 4 \mu\text{m}$, respectively. As reported by Gratzel et al.,^[120] such dimensions are optimal for DSSCs. In contrast, PSCs included thin layers, which can be seen in Figure 3.8b. Their thicknesses were determined as follows: the first layer of TiO₂ NPs $\approx 50 \text{ nm}$, the second layer of TiO₂ NFs $\approx 200 \text{ nm}$, a light-absorbing layer of perovskite (MAPbI₃) $\approx 400 \text{ nm}$, a p-type polymer layer of PTTA (poly(triaryl amine)) $\approx 80 \text{ nm}$, and a metal (gold) counter electrode $\approx 100 \text{ nm}$, respectively.

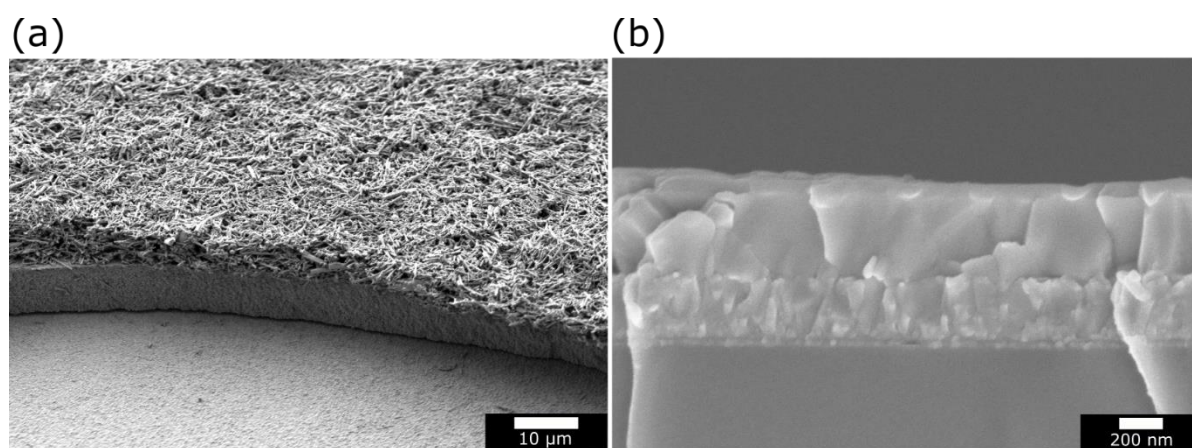


Figure 3.8. Cross-section SEM images of (a) a DSSC and (b) a PSC.

J-V curves of the best DSSCs implementing control, lanthanum, and lithium treated TiO₂ NFs can be seen in Figure 3.9, and their photovoltaic parameters are shown in Table 3.5. The parameters revealed that the highest performing DSSCs were obtained using lanthanum treated TiO₂ NFs with PCE of 6.4%. Compared to the control, an improvement of 17.2% was achieved. While lanthanum treatment increased all photovoltaic parameters, the main reason for such an improvement in PCE was due to the J_{sc} and fill factor (FF), which were 9% and 8% higher, respectively. To elaborate

such trends further, dye-desorption tests were performed, as illustrated in Table 3.4. As noted previously from the BET surface area measurements, lanthanum treated TiO₂ NFs produced the highest values, which is beneficial for the dye absorption characteristics. The relation between the BET surface area and dye absorption was further validated and the highest dye uptake was achieved for lanthanum treated TiO₂ NF photoelectrodes. While there have been reports about the beneficial impact of oxygen vacancies towards the dye uptake properties of photoelectrodes,^[97] it was concluded that the main explanation for such trends was the increased BET surface area. Additionally, dye uptake measurements for control and lithium treated TiO₂ NFs were performed, however, dye absorption was within a similar range (Table 3.4). Not surprisingly, the latter type of DSSCs also exhibited comparable J_{SC}, further supporting the dye uptake measurements. PCEs were dissimilar to DSSCs; implementing lithium treated TiO₂ NFs demonstrated slightly higher efficiency, due to the improved V_{OC} and FF as illustrated in Table 3.5.

Table 3.4. Dye absorption results for control, lanthanum, and lithium treated TiO₂ NFs. The characterisation was performed on glass substrates that consisted of a relevant layer of TiO₂ NFs. Their area was 1 x 1.5 cm².

Substrate type	Dye absorption (µg)
Control	53.9
Lanthanum treated TiO₂	66.6
Lithium treated TiO₂	55.7

As reported by other authors in the field,^[90] the rutile phase of TiO₂ is not favourable for solar cell use. Moreover, if two TiO₂ phases are present together, for instance the rutile and anatase phases, that is not advantageous because the result of their dissimilar band structures can cause charge recombination. From the XRD results

discussed above (Figure 3.4a), it was determined that lithium treatment of TiO₂ NFs has induced the rutile phase formation at lower temperatures than what is typically reported. Therefore, this was not beneficial for the current flow in DSSCs, since the J_{sc} parameter was lower compared to the control. Contrary to this, Wang et al.^[121] performed an investigation into lithium doping of different sized TiO₂ NPs and their influence on DSSCs. It was discovered that for NP sizes below 6 nm, the doping was beneficial, while for sizes above 14 nm the outcome was the opposite. The origin for such performance difference was attributed to the lithium insertion mechanism, where, in the case of small sized NPs, they were present on the surface as opposed to the bulk insertion for bigger sizes. Consequently, different lithium insertions influence the photovoltaic properties individually.^[121] However, as opposed to a negative impact on J_{sc}, lithium treatment notably improved V_{oc}, which was not observed for lanthanum treatment, as the values compared to the control remained very much alike. The reason for a V_{oc} improvement in DSSCs containing lithium treated TiO₂ NFs, was associated with the alterations of V_{FB} (flat-band potential) inducing an increase on E_F and CB.^[90] While metal ion modifications individually influenced J_{sc} and V_{oc}, they both caused an increase of FF, which agrees well with other reports in the literature.^[97,121] It should be noted that the trends in photovoltaic parameters for the highest performing DSSCs discussed herein, have been verified by fabricating separate batches of devices, as compiled in Table 3.6, where no changes were observed compared with Table 3.5.

Table 3.5. Photovoltaic parameters for the highest performing DSSCs extracted from the J-V curves in Figure 3.9.

	Jsc (mA cm⁻²)	Voc (mV)	FF (%)	PCE (%)
Control	12.8	735	56.8	5.3
Lanthanum treated TiO₂ NFs	14.1	737.5	61.6	6.4
Lithium treated TiO₂ NFs	12.3	749.4	61.3	5.6

Table 3.6. Average solar cell parameters for 5 separate batches of DSSCs with their standard deviations in brackets.

	Jsc (mA cm⁻²)	Voc (mV)	FF (%)	PCE (%)
Control	12.8 (± 0.3)	738.1 (± 3.3)	56.2 (± 1.0)	5.3 (± 0.07)
Lanthanum treated TiO₂ NFs	13.8 (± 0.2)	739.4 (± 2.8)	60.4 (± 1.3)	6.3 (± 0.2)
Lithium treated TiO₂ NFs	12.4 (± 0.2)	749.4 (± 4.8)	61.3 (± 1.5)	5.6 (± 0.2)

Further characterisation on the DSSC performance trends between different types of TiO₂ NFs was performed by analysing the average resistance measurements. Table 3.7 shows values determined for R_s measurements, where lower R_s are favourable for obtaining high FF. As the results illustrate, the lowest R_s were obtained for DSSCs containing lanthanum treated TiO₂ NFs, which supports their highest FF (Table 3.5 and 3.6). Furthermore, the same finding also applies for lithium treated TiO₂ NFs where, compared to the control, lower R_s indicates higher FF. As reported by other researchers,^[122] lanthanum doping can result in photocatalytic hydrogen and oxygen evolution. Hence, lanthanum treatment of TiO₂ NFs could also influence the oxidation rate of iodine ions from the electrolyte at the photoelectrode, where the regeneration of N719 molecules occurs, resulting in a decrease of R_s. However, to expose such interactions, additional characterisation would have to be performed. As opposed to low R_s resulting in lower FF, high R_{SH} typically results in higher FF. As the results in

Table 3.7 indicate, the same trends were also observed where the control TiO₂ NF DSSCs exhibited the lowest R_{SH} and consequently the lowest FF. Moreover, R_{SH} can also give an indication of power losses in DSSCs, which occur because of an alternate current path for the light-generated current; thus, low R_{SH} causes high power losses. Accordingly, high R_{SH} are required for DSSCs since this indicates low current leakage. Ideally, the value should exceed that of 6 x 10³ Ω cm², since that would indicate that the impact of R_{SH} on FF can be ignored.^[123] According to the results of this study, R_{SH} values were always below 6 x 10³ Ω cm² indicating the presence of the current leakage in fabricated DSSCs.

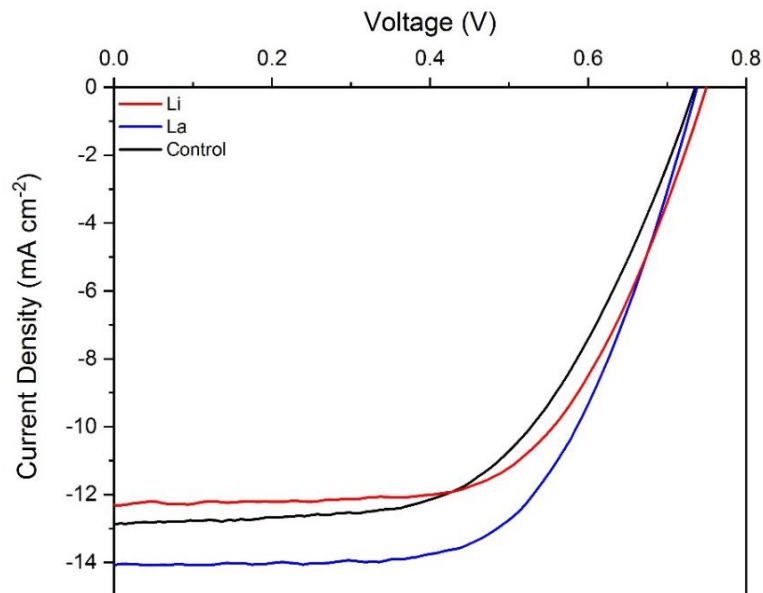


Figure 3.9. Control (black), lithium treated (red), and lanthanum treated (blue) TiO₂ NF based DSSCs. J-V curves were collected under AM 1.5 solar irradiation.

Table 3.7. Mean R_{SH} and R_s for control, lanthanum treated, and lithium treated TiO_2 NF based DSSCs. The values were determined from the corresponding J-V curves.

	R_{SH} ($\Omega\text{ cm}^{-2}$)	R_s ($\Omega\text{ cm}^{-2}$)
Control	1147	16.8
Lanthanum treated TiO_2 NFs	3387	13.4
Lithium treated TiO_2 NFs	2351	16.5

Since there are many drawbacks related to the use of aqueous components in solar cells, efforts were aimed towards developing all solid-state photovoltaic devices.^[124] Recently, PSCs have attracted immense attention as they showed promise of high efficiency in combination with the use of all solid-state components.^[125] Therefore, TiO_2 NFs that were produced in this study were also implemented for a PSC configuration as a mesoporous layer. It is noteworthy that as opposed to a mesoporous layer of TiO_2 NPs, obtaining the same quality layer for TiO_2 NFs is not straightforward. To achieve a uniform layer that can be suitable for device fabrication, many steps are required, which, among others, include the dispersion of NFs in a paste at the right concentration and optimization of the deposition parameters for a glass substrate. How different parameters affected the coverage characteristics of TiO_2 NFs is shown in Figure 3.10. Figure 3.11 demonstrates the coverage that was considered as optimal, and which was used for the device fabrication.

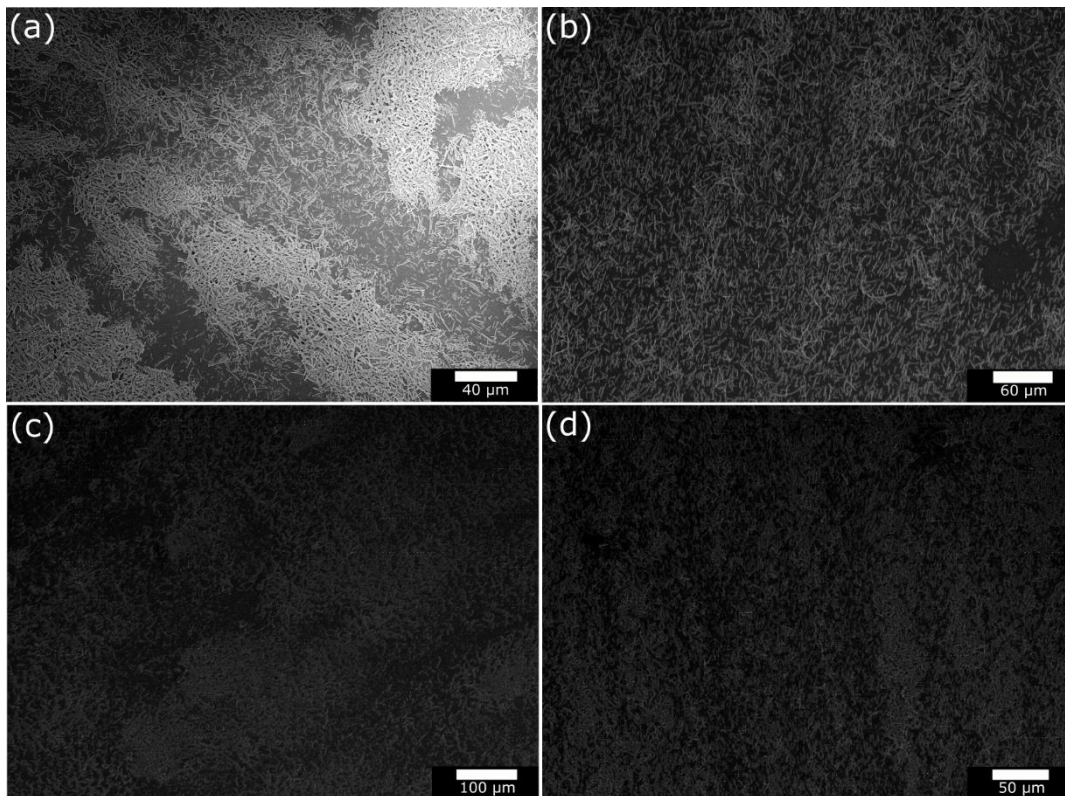


Figure 3.10. SEM images showing surface coverage characteristics for control TiO_2 NFs that were spin coated on substrates under the following conditions; (a) 1000 RPM for 20 sec and 2000 RPM for 5 sec (60 mg/mL), (b) 3000 RPM for 30 sec (30 mg/mL), (c) 5000 RPM for 30 sec (30 mg/mL), and (d) 6000 RPM for 30 sec (30 mg/mL).

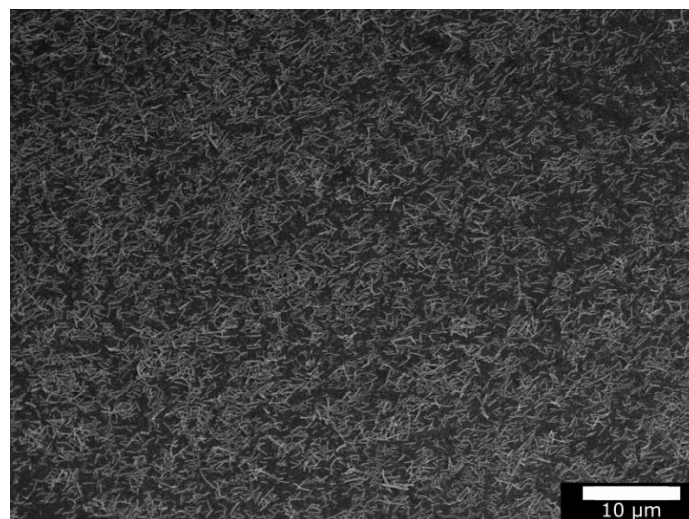


Figure 3.11. SEM image of control TiO_2 NFs that were spin coated at 4000 RPM for 30 sec (30 mg/mL).

Figure 3.12 demonstrates J-V curves for PSCs that delivered the best performance. From these results, photovoltaic parameters were determined, as seen in Table 3.8. As already observed for DSSCs, the best performing devices implemented lanthanum treated TiO₂ NFs. In comparison to PSCs that implemented control TiO₂ NFs, PCE notably improved, as a result of significantly enhanced J_{sc}, which increased by approximately 10%. Such a big J_{sc} increase can be attributed to better charge transport due to the presence of lanthanum treated TiO₂ NFs. As discussed above, lanthanum treatment induced the formation of oxygen vacancies (Figure 3.4b), which are known to be advantageous against charge recombination.^[126] Therefore, these point defects trapped electrons, which in turn inhibited the recombination between electrons and holes in the mesoporous layer. In addition, oxygen vacancies can minimize the aggregation of injected electrons in the n-type layer, thus further hindering charge recombination. With the accumulation of electrons in defects, the electron concentration increases, which consequently influences the material's conductivity.^[126] Thus, the effect can also be recognized as n-type doping of the material. Together with J_{sc}, lanthanum treated TiO₂ NFs also influenced V_{oc}, where the parameter increased by roughly 4% (Table 3.8). In contrast, the same trend was not identified for DSSCs. Since the changes in V_{oc} are related to Fermi energy alterations, it appeared that the effect was more pronounced in PSCs. To examine the reproducibility of PSCs assembled in this study, five separate batches of devices were fabricated, and the average performance parameters are illustrated in Table 3.9. It should be noted that the trends discussed above did not change between different batches of PSCs.

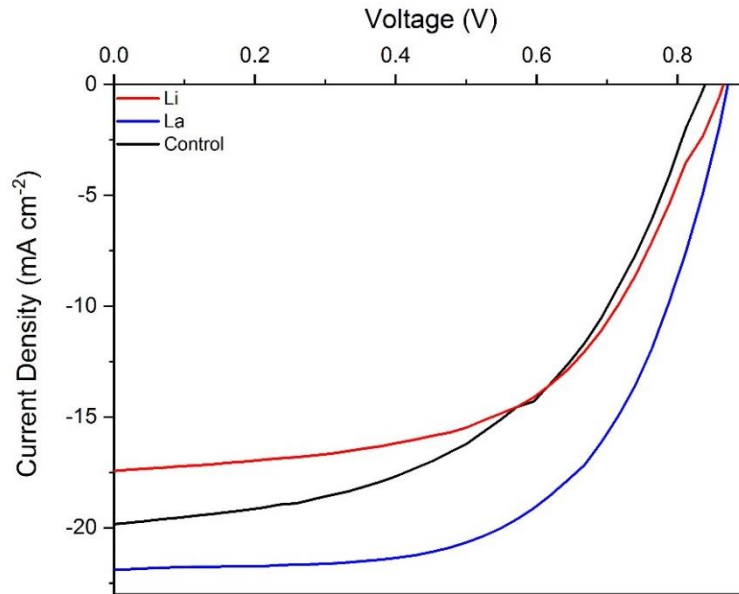


Figure 3.12. Control (black), lithium treated (red), and lanthanum treated (blue) TiO₂ NF based PSC. J-V curves were collected under AM 1.5 solar irradiation.

Table 3.8. Photovoltaic parameters for the highest performing PSCs extracted from the J-V curves in Figure 3.12.

	J_{sc} (mA cm⁻²)	V_{oc} (mV)	FF (%)	PCE (%)
Control	19.8	839	51.2	8.5
Lanthanum treated TiO₂ NFs	21.9	871.7	60.2	11.5
Lithium treated TiO₂ NFs	17.4	865.3	55.8	8.4

Table 3.9. Average solar cell parameters for 5 separate batches of PSCs with their standard deviations in brackets.

	J_{sc} (mA cm⁻²)	V_{oc} (mV)	FF (%)	PCE (%)
Control TiO₂	19.8 (± 0.2)	801.1 (± 24.6)	54.6 (± 3.85)	8.8 (± 0.5)
Lanthanum treated TiO₂ NFs	21.6 (± 0.7)	850.8 (± 15.7)	62.0 (± 1.9)	11.4 (± 0.4)
Lithium treated TiO₂ NFs	17.4 (± 0.6)	842.7 (± 15.0)	50.8 (± 2.7)	7.5 (± 0.7)

The beneficial influence of lanthanum treatment on PSC parameters also resulted for FF, which was correlated with R_s and R_{SH} as shown in Table 3.10. PSCs with lanthanum treated TiO_2 NFs exhibited the lowest R_s and the highest R_{SH} , which supports the trends of the highest FF. Since the R_{SH} did not exceed $6 \times 10^3 \Omega \text{ cm}^2$, current leakage caused by the pinholes in the devices was present. However, compared with PSCs with control or lithium treated TiO_2 NFs, the current leakage was reduced in the devices implementing lanthanum treated TiO_2 NFs, resulting in improved performance. Since control PSCs exhibited the lowest FF, R_{SH} was the highest. While the R_s values did not support the trends of FF, it was concluded that their impact was reduced, which was already noted by others.^[73]

Table 3.10. Average R_{SH} and R_s for control, lanthanum treated, and lithium treated TiO_2 NF based PSCs. The values were determined from the corresponding J-V curves.

	$R_{SH} (\Omega \text{ cm}^2)$	$R_s (\Omega \text{ cm}^2)$
Control TiO_2	206	11.1
Lanthanum treated TiO_2 NFs	289	15.7
Lithium treated TiO_2 NFs	1392	8.8

PSCs with lanthanum treated TiO_2 NFs exhibited superior photovoltaic parameters (J_{sc} , V_{oc} and FF) when compared to the devices with control or lithium treated TiO_2 NFs. Consequently, their total PCE was markedly higher. However, if TiO_2 NP based PSCs are taken into account and compared to PSCs of this study, the performance of the former type is significantly better.^[127] This can mainly be attributed to the surface characteristics, because the coverage with TiO_2 NFs is more uneven and saturated with defects, which in turn influences the perovskite crystal formation and charge

recombination level.^[128] Therefore, the parameters, such as J_{sc} , V_{oc} , and FF are negatively altered resulting in lower PCEs. To further validate these statements, PSCs with TiO_2 NPs as a mesoporous layer were fabricated and compared to the highest performing photovoltaic solar cells in this study. The results revealed (Figure 3.13) that the photovoltaic parameters notably increased, yielding a PCE of 17.6%, which is comparable to other reports in the literature.^[106] Nevertheless, compared to NPs, cell configurations with NFs can also be high-performing as a result of their various beneficial properties.^[129] Therefore, it is expected that the performance of NF based photovoltaic cells can be improved further.

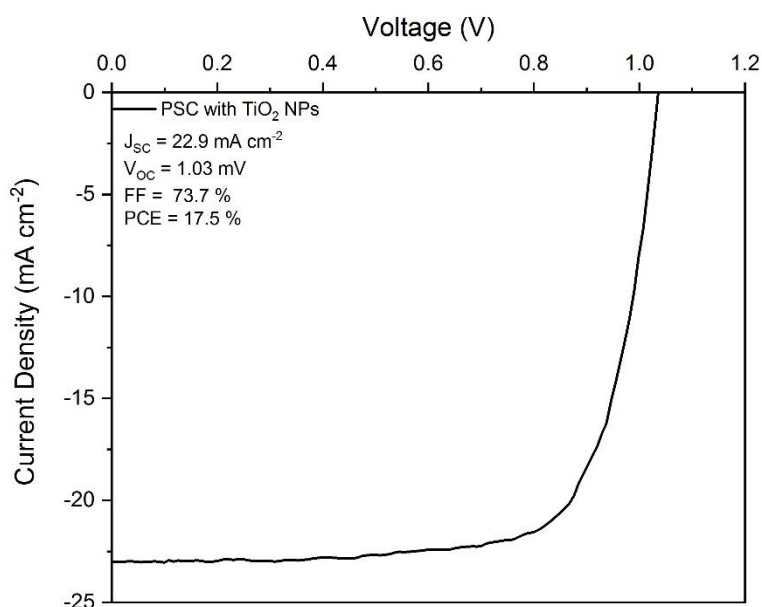


Figure 3.13. A TiO_2 NP based PSC.

Based on the results of this study, it was revealed that lithium treated TiO_2 NFs, when implemented for DSSCs and PSCs, show detrimental or very similar performance metrics compared to the control. However, the addition of lithium, specifically its salt named lithium bistrifluoromethanesulfonimide (Li-TFSI), which is extensively used in the field of PSCs for n-type^[130] and p-type^[131,132] layers, is known to be advantageous.

It's effects are related to the downshifting of the CB, which consequently improves photovoltaic parameters.^[98] While it has been shown here that the addition of lithium to TiO₂ NFs facilitated the development of the rutile phase, which is unfavourable for the use in solar cells, the same outcome does not arise through the incorporation of Li-TFSI. As opposed to the direct addition of lithium salt (in this work lithium acetate) to the precursor sol-gel solution for TiO₂, Li-TFSI is spin coated on the already formed TiO₂ material.^[130,133,134] For PSCs, there have not been any reports about detrimental effects of lithium addition on photovoltaic performance, as opposed to DSSCs where both favourable and negative effects were reported.^[98,121,135] When beneficial outcomes were claimed for lithium treatment, they were typically related to the improved conductivities and charge densities, both of which can be associated with a p-type dopant (Li-TFSI).^[136] Therefore, Li-TFSI is typically added to p-type layers. However, beneficial outcomes were also reported for n-type layers but only when lithium was present together with a TFSI⁻ anion (Figure 3.14). Such findings point towards the anion having the main significance on the improvement, possibly due to its conductivity.^[136] Since the lithium salt that was used in this work did not contain such anions, a detrimental impact was recorded.

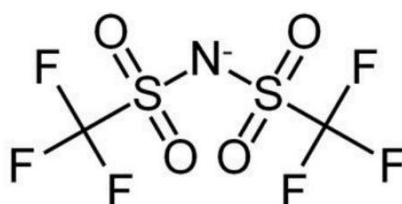


Figure 3.14. Structural formula of bis(trifluoromethanesulfonyl)imide (TFSI) anion.

3.4 Conclusion

As opposed to the two-step TiO₂ NF modification method in chapter 2, a one-step approach is shown in chapter 3, where TiO₂ NFs were separately treated with lanthanum and lithium salts that were directly added to the precursor sol-gel solution for electrospinning. Based on the characterisation results, it was concluded that neither lanthanum or lithium induced any notable substitutional or interstitial defects of the TiO₂ material. This was attributed to their ionic radii, which are bigger compared to Ti⁴⁺. On the other hand, structural modifications were observed for lithium treated TiO₂ NFs, with the detection of the rutile phase at lower temperatures than typically reported. While potential crystal structural changes were not identified for lanthanum treated TiO₂ NFs, their crystallite sizes were reduced, which consequently increased their BET surface area. However, lithium treatment conversely influenced the crystallite sizes whereby the BET surface area for lithium treated TiO₂ NFs decreased. In addition, lanthanum treatment induced the formation of oxygen vacancies, wherein such a phenomenon was not detected for lithium treatment. To examine the applications of synthesized materials, TiO₂ NFs were used for solar cells as a n-type layer and two different types were fabricated, namely DSSCs and PSCs. Photovoltaic results revealed that lanthanum treated TiO₂ NFs improved the performance of both types of solar cells, while the same outcomes were not observed for lithium treated TiO₂ NFs. Compared to the control DSSCs, lanthanum treated TiO₂ NFs showed a performance improvement of ≈17%, while within PSCs the improvement was in the range of ≈35%. In the former type, the enhancement in PCE was mostly attributed to higher BET surface area, which improved dye absorption, whereas in the latter type, improvement was associated with the presence of oxygen vacancies, which are beneficial for the charge transport characteristics of the material. While chapter 3

covered the additive interactions on the performance of n-i-p solar cells, in chapter 4, the study is extended towards material synthesis of other classes of nanomaterials.

Chapter 4

Room temperature synthesis of perovskite nanocrystals via phosphine-based chemistry

4. Room temperature synthesis of perovskite nanocrystals via phosphine-based chemistry

4.1 Introduction

In recent years, perovskite materials have attracted enormous research interests worldwide.^[137] The original mineral was discovered in the 19th century and composed of a CaTiO_3 crystal structure, known as perovskite.^[138] While this specific material is non-conductive, perovskite materials that share the same structure (ABX_3), where typically, but not exclusively, A-site cations are caesium, methylammonium, or formamidinium, B-site cations are lead, or tin, and X-site anions are chlorine, bromide or iodide, exhibit entirely the opposite characteristics.^[139] Therefore, these type of materials emerged as a novel class of semiconductors and have been extensively used for various types of optoelectronic applications.^[140] Perovskites were initially used as light absorbing layers for DSSCs. In such photoelectrochemical cells, a liquid electrolyte is typically employed as a hole-transport layer, however, it disintegrated the perovskite material, which resulted in very unstable DSSCs. In contrast, when liquid electrolytes were replaced with a solid-state alternatives (p-type layer), the performance of all solid-state PSCs significantly increased, and within a few years reached PCEs above 20%.^[141,142] As a result of such exceptional material characteristics, perovskites were also used for other applications, for instance LEDs,^[143] photodetectors,^[144] catalysis,^[145] and lasers.^[146] While for solar cells the most frequently employed form of perovskites are thin films, these films without passivation exhibit low PLQYs, which is a requirement for high performing LEDs and similar type of devices.^[147,148] On the other hand, high PLQYs (near unity) without the

necessity for extensive passivation can be obtained with QDNCs.^[149] Perovskite materials in a colloidal form were first synthesized in 2014.^[150] The first type reported was $\text{CH}_3\text{NH}_3\text{PbBr}_3$ QDNCs, then followed by other variations.^[151] Compared to thin films, QDNCs typically achieve high PLQY values. Moreover, they exhibit many other advantages, and many of their favourable characteristics cannot be obtained with bulk materials.^[152] For instance, the quantum-confinement regime, where the light emission of QDNCs can be manoeuvred via different NP sizes.^[153] Other methods of tunable light emission include compositional changes, nanostructuring, post-synthesis anion exchange, or exfoliation.^[154,155] Another advantage of QDNCs is the possible generation of multiple excitons, which for solar cells can result in overcoming the Shockley-Queisser efficiency limit.^[156] Furthermore, in the form of colloidal QDNCs, specific perovskite phases can be obtained at RT conditions, for example cubic CsPbI_3 phase, which in the form of thin films transforms into the optically inactive orthorhombic phase.^[157]

In the past few decades, the most widely explored quantum dots were metal chalcogenides-based, such as binary type II-VI, III-V, and IV-VI.^[158] With the emergence of perovskite QDNCs, a new type of semiconducting colloids was discovered, which possesses different characteristics compared to the former type. While binary quantum dots are defect-intolerant, meaning that extensive passivation of the core is required to achieve high performance, perovskite QDNCs are defect-tolerant and can be bright emitters without the necessity for passivation.^[159] However, this does not mean that no charge recombination (non-radiative) centres are present, where the opposite was reported,^[160] but rather that the high-performance characteristics can be obtained at a significantly lower price (no need for surface passivation).

Since the performance characteristics of perovskite QDNCs are advancing towards the values required for commercialisation, a lot of research has been aimed towards achieving synthesis conditions that will allow cheap, large-scale production. The most popular and widely employed synthesis method is performed in non-coordinating solvents with a combination of carboxylic acid and primary amines at high temperatures between 120 - 200 °C (depending of the required size). This is a costly approach that can be problematic for upscaling.^[161,162] Furthermore, this synthesis method requires conditions excluding moisture or oxygen, which additionally affects the total price. Therefore, it is a prerequisite to develop new synthesis pathways that can solve the aforementioned drawbacks. While efforts were aimed towards RT and inert, atmosphere-free conditions, such synthesis routes (ligand-assisted reprecipitation approach - LARP), typically require the use of coordinating solvents, for example, dimethylformamide (DMF).^[163] Since these solvents are toxic, the LARP approach has several disadvantages that render it unfeasible for large scale employment. Together with toxicity, there are further shortcomings from the use of polar solvents, for example, a high solubility characteristic of DMF is that it can dissolve or harm perovskite QDNCs.^[154] Moreover, it was also reported that the interactions caused by polar solvents can lead to the creation of flawed perovskite QDNCs.^[164] While DMF can be typically removed from the compounds via high temperature treatment, such conditions would result in perovskite phase transition, indicating that the approach is unsuitable. Therefore, the objective is to perform syntheses at low temperatures and in industrially compatible solvents. Although particular groups reported on some synthesis approaches that meet the criteria, their techniques require either the use of long chain ligand combinations (oleic acid/oleylamine), or individual preparation of precursors at elevated temperatures.^[165,166]

Herein, a new synthesis route is presented where high-quality perovskite QDNCs are formed at RT, in air, without the use of a commonly employed ligand combination (oleic acid/oleylamine) and using an industry compatible solvent (octadecene). For that reason, phosphine-based ligands were employed, which allowed the synthesis of an organic cation free perovskite (CsPbBr_3) and an organic-inorganic combination (FAPbBr_3) of QDNCs. The characterisation revealed that this simple synthesis approach yields high-quality QDNCs, which exhibit cubic phase structure with a high degree of crystallinity. Furthermore, optical properties of QDNCs were of high-performance, with the fwhm values below 20 nm for both types and the emission for RT- FAPbBr_3 (room temperature formamidinium lead tribromide) QDNCs centred between 530 – 535 nm. Such a region is in line with the Rec. 2020 colour gamut.^[167] To investigate how capping ligands interact with the NC core, spectroscopic methods were used, which revealed that the surrounding phosphine ligands bind to the core via a Pb-O-P bond. Since one of the main disadvantages for the use of QDNCs in optoelectronic applications is the presence of insulating ligands, their binding strength and the possibility of removal was further investigated. The results revealed that compared to the reference combination of ligands (oleic acid/oleylamine), the phosphine-based alternative was easier to remove. Therefore, the number of organics was significantly reduced, which is a beneficial outcome for the use of phosphine capped QDNCs in applications, for example LEDs, solar cells, and photodetectors.

4.2 Experimental section

All chemicals that were used for this work, were purchased from Sigma Aldrich (UK). No further purification was employed for the obtained chemicals.

4.2.1 Synthesis of RT-FAPbBr₃ quantum dot nanocrystals

RT-FAPbBr₃ QDNCs were synthesized by adding 0.052 g of formamidine acetate salt into a vial, together with 4 mL of octadecene and 1 mL of diisooctylphosphinic acid (DiOPA) resulting in 0.1 mol/L concentration (solution 1). In another vial of the same size, 0.023 g of lead(II) bromide, 0.333 g of trioctylphosphine oxide (TOPO), 1.7 mL of octadecene, and 0.333 mL of DiOPA were added together (solution 2). To completely dissolve the compounds, both vials were placed on a magnetic stirrer until the solutions turned clear. Subsequently, 0.833 mL of solution 1 was quickly injected into the vial of the solution 2, which resulted in an immediate formation of RT-FAPbBr₃ QDNCs. They were separated from the reaction solution via centrifugation (7500 RPM for 10 min), where the supernatant was disposed of, and the precipitates were dissolved in 4 mL of non-polar solvent (toluene). Any excess organic compounds from QDNCs were removed via purification treatment. The process of purification was performed with the addition of an antisolvent (acetonitrile) to the solution of QDNCs in the ratio of 3:1. Afterwards, the solution was centrifuged (7500 RPM for 10 min) and the precipitates dispersed in toluene (4 mL). When syntheses were performed at elevated temperatures, the required compounds were added to 3-neck flasks that were in heating mantles and connected to the Schlenk line. Further steps were repeated as described above.

4.2.2 Synthesis of Con-FAPbBr₃ quantum dot nanocrystals

Con-FAPbBr₃ (control formamidinium lead tribromide) QDNCs were synthesized by loading 0.261 g of formamidine acetate salt into a 3-neck flask, together with 10 mL of

oleic acid. The flask was then connected to the Schlenk line and heated under nitrogen to 130 °C until the solution turned clear, without any solid agglomerates left. Subsequently, the flask was cooled to 50 °C and dried for 30 min, followed by an increase in temperature to 100 °C under nitrogen (solution 1).

In another 3-neck flask of the same size, 0.069 g of lead(II) bromide was loaded together with 5 mL of octadecene and heated under nitrogen to 120 °C, at which point the solution was dried for 1 hour. The flask was then purged with nitrogen, followed by the addition of 0.5 mL of dried oleylamine and 0.5 mL of dried oleic acid to solubilize the lead salt. From this point onwards, the flask was always kept under nitrogen (solution 2). After approximately 15 min, 2.5 mL of solution 1 was quickly injected into solution 2, and after 5 sec the reaction solution was cooled by immersing the flask in an ice-water bath to quench the nucleation of con-FAPbBr₃ QDNCs. These were separated from the reaction solution via centrifugation at 12500 RPM for 10 min. The supernatant was discarded, and the precipitates dissolved in 4 mL of toluene. To remove excess organics, 1.25 mL of an antisolvent (acetonitrile) was added to the solution, followed by another centrifugation at 12500 RPM for 10 min. Finally, the supernatant was discarded, and the precipitates dissolved in 5 mL of toluene.

4.2.3 Synthesis of RT-CsPbBr₃ quantum dot nanocrystals

RT-CsPbBr₃ (room temperature caesium lead tribromide) QDNCs were synthesized by adding 0.0407 g of caesium carbonate into a vial together with 2 mL of octadecene and 0.2 mL of DiOPA (solution 1). In a different vial of the same size, the same quantities of lead(II) bromide, TOPO, octadecene, and DiOPA as for RT-FAPbBr₃ QDNCs were loaded (solution 2). To completely solubilize the compounds, both vials

were placed on a magnetic stirrer and left there until both solutions turned clear. To form RT-CsPbBr₃ QDNCs, 0.133 mL of solution 1 was quickly injected into solution 2. They were purified via the addition of methyl acetate in the volume ratio of reaction solution : antisolvent = 1 : 2.3. This solution was then centrifuged at 7500 RPM for 10 min. The supernatant was discarded, and the precipitates dissolved in a polar solvent (4 mL of toluene), forming a colloidal solution of RT-CsPbBr₃ QDNCs. Where QDNCs were not subject to purification, the reaction solution was centrifuged without the addition of an antisolvent and the precipitates were dissolved as described above.

4.2.4 Synthesis of Con-CsPbBr₃ quantum dot nanocrystals

Con-CsPbBr₃ (control caesium lead tribromide) QDNCs were synthesized by loading 0.204 g of caesium carbonate into a 3-neck flask together with 10 mL of octadecene and 0.625 mL of oleic acid. The flask, which was connected to the Schlenk line, was heated to 120 °C and dried under nitrogen conditions for 1 h. The temperature was then raised to 150 °C until all caesium carbonate was completely dissolved, followed by decreasing the temperature to 100 °C (solution 1).

In an additional 3-neck flask of the same size, 0.069 g of lead(II) bromide was loaded together with 5 mL of octadecene. This solution was dried at 120 °C for 1 h. Subsequently, 0.5 mL of dried oleylamine and 0.5 mL of dried oleic acid were added under nitrogen so that the lead(II) bromide salt completely dissolved. The temperature of the solution was then raised to 140 °C (solution 2). To form con-CsPbBr₃ QDNCs, 0.4 mL of solution 1 was quickly injected and after 5 sec the reaction solution was cooled by immersion of the flask into an ice-water bath. To purify QDNCs, methyl acetate was directly added in the volume ratio of reaction solution : antisolvent = 1 :

2.3, followed by centrifugation (7500 RPM for 10 min). Afterwards, the supernatant was discarded, and the precipitates dissolved in 4 mL of toluene. Where QDNCs were not purified, the procedure was identical as described above.

4.2.5 Details of instrumentation used

TEM, XRD, and XPS were performed with the equipment and using the methods that are described in section 2.2.5.

UV/Vis characterisation was performed using the Perkin Elmer Lambda 950, where, during the measurements, an interval of 1 nm was used. The colloidal solutions of QDNCs in toluene were measured with quartz cuvettes that had a 1 cm path length.

PL measurements were performed using the Horiba FluoroMax-4 spectrofluorometer. Fwhm values were determined using a Gaussian fit function, in Origin. PLQY characterisation was performed using quartz cuvettes with a colloidal solution of QDNCs, in an integrating sphere. To prevent saturation of the detector, and to have the number of counts in the range of $\approx 1 \cdot 10^6$ a.u., a neutral-density filter and different types of slit widths were used, together with the concentration manipulation of the colloidal solution in quartz cuvettes. To calculate the values, the following equation was used:

$$\varphi = (E_c - E_a) / (L_b - L_c) \quad (1.1)$$

In this equation, L_b (solvent – toluene) and L_c (QDNC solution) correspond to the scattering data, and E_a (solvent – toluene) and E_c (QDNC solution) correspond to the fluorescence emission data. The absorption of photons was determined from the scattering peaks of a solvent and a QDNC solution, where the emission of photons was in turn determined from the emission data of QDNCs. PLQY measurements for FAPbBr₃ QDNCs were performed on the same day as the synthesis, while for CsPbBr₃ QDNCs measurements were performed one day after. For the measurements, the excitation of 400 nm was used, and the data was collected in the region between 450 – 600 nm.

For photoluminescence decay measurements, a Delta Flex system (Horiba Scientific) was employed. For excitation, a laser with a wavelength of 404 nm was used and the signal was collected by PPD-900 (Horiba Scientific) detector. Quartz cuvettes with a 1 cm path length were used for colloidal solutions of QDNCs.

FTIR characterisation was carried out using a Bruker Spectrometer Alpha II with an attenuated total reflection (ATR) accessory. The FTIR spectra were recorded between the 4000 – 400 cm⁻¹ region and the samples were in a powder form. To obtain enough material (QDNCs) for the measurements, the synthesis was scaled up by a factor of 9. For RT-FAPbBr₃ QDNCs, the concentration of solution 1 (see section 4.2.1) was increased to 0.25 mol/L and the injection was performed at an elevated temperature (100 °C). The colloidal reaction solution of QDNCs was centrifuged at 7500 RPM for 10 min and the precipitates were dried for 24 h in a desiccator.

Thermal gravimetric analysis (TGA) was performed on a Perkin Elmer 7 Thermogravimetric Analyzer under nitrogen gas with a flowrate of 20 mL/min. The heating rate used during the measurements was 5 °C/min in the region between 30

°C and 800 °C. For the analysis, 7 – 10 mg of powder QDNCs were used, where the synthesis was significantly scaled up, as discussed above.

4.3 Results and discussion

4.3.1 Synthesis of quantum dot nanocrystals and their characteristics

In this section, a novel synthesis route consisting of a ligand combination that includes TOPO and DiOPA is presented, which replaces the use of oleic acid and oleylamine. In a typical method reported by Kovalenko et al.,^[151] a ligand combination of oleic acid/oleylamine is employed for the synthesis of perovskite QDNCs. The purpose of the used ligands is to dissolve the precursor salts in octadecene, which is only viable at elevated temperatures and is essential for the successful synthesis of nanomaterials. For instance, to dissolve the cation (Cs^+ or FA^+) precursor compounds (Cs_2CO_3 or formamidinium acetate) in non-polar solvents, a fatty acid such as oleic acid is used, and the solvation only occurs at temperatures above 100 °C. On the other hand, for the solvation of anions of the perovskite crystal structure (Pb^{2+} and halogens $\rightarrow \text{Cl}^-$, Br^- or I^-) in octadecene, where the precursor compound is usually a lead salt, a combination of two types of ligands (oleic acid/oleylamine) is necessary along with temperatures of around ≈ 110 °C.^[151] While there were attempts to decrease the synthesis temperatures, for example, an amine-free route made the reaction feasible at ≈ 75 °C,^[168] efforts aiming at RT conditions were unsuccessful. In this work, with the employment of a DiOPA ligand as an alternative to oleic acid, the solvation of a compound that serves as a cation source (Cs^+ or FA^+) was made possible at RT

conditions and in non-polar solvents. In addition, an oleic acid/oleylamine ligand combination was replaced by TOPO and DiOPA, which allowed the solvation of a lead salt (the source for both cations) and the formation of a clear solution at RT, in octadecene. It is noteworthy that the addition of DiOPA is not required for the solvation purposes as TOPO alone can dissolve the lead salt in octadecene. However, experiments have shown that a combination of TOPO and DiOPA yields QDNCs of better quality, which can possibly be related to a better surface coverage of the QDNC core.

By using an alternative ligand combination, two types of perovskite QDNCs were successfully synthesized, i.e. FAPbBr₃ (labelled in this chapter as RT-FAPbBr₃) and CsPbBr₃ (labelled in this chapter as RT-CsPbBr₃) QDNCs at RT, in air, without the protective inert gas environment and in non-coordinating solvents. While these reactions occurred rapidly, the nucleation rates for particular type of QDNCs were different. Specifically, when a precursor solution of formamidinium acetate was injected into a precursor solution containing the lead salt, the formation of RT-FAPbBr₃ QDNCs was instantaneous, as opposed to the injection of a precursor solution containing Cs₂CO₃, where a slightly delayed nucleation was observed (formation of RT-CsPbBr₃ QDNCs). As reported by other researchers in the field,^[168] the nucleation rate of nanomaterials is generally associated with their capping ligands. Since in this study, the same type and quantity of ligands were used independently of the class of QDNCs, different nucleation rates suggest that their growth dynamics were influenced by the cation size. In particular, a smaller Cs⁺ size was responsible for the delayed formation of RT-CsPbBr₃ QDNCs, as opposed to the immediate formation of RT-FAPbBr₃ QDNCs, where the FA⁺ size is bigger. The origin behind such a facile formation of high-quality QDNCs can be related to their ionic bonding.^[169] Their shape

and size characteristics were identified using TEM, as seen in Figures 4.1 and 4.2. The average edge-length of cubes of RT-CsPbBr₃ QDNCs (Figure 4.1) was determined to be ≈ 14 nm with a moderate standard deviation ($\approx 12\%$), which indicates the range of size variation among particular cubes. Furthermore, HR-TEM images showed that RT-CsPbBr₃ QDNCs were highly crystalline with a separation between lattice planes of ≈ 5.8 Å (Figure 4.1c). This value is in line with the (100) crystal plane of the perovskite cubic arrangement.^[161] While TEM characterisation of RT-CsPbBr₃ QDNCs was relatively straightforward, imaging RT-FAPbBr₃ QDNCs proved to be challenging as they were unstable under the beam of electrons. Nevertheless, Figure 4.2 shows resultant TEM images, which reveal that compared with RT-CsPbBr₃ QDNCs, RT-FAPbBr₃ QDNCs were bigger. Their average size was ≈ 38 nm with a slightly higher standard deviation ($\approx 16\%$) and identical lattice spacing (≈ 5.8 Å) (Figure 4.2c).

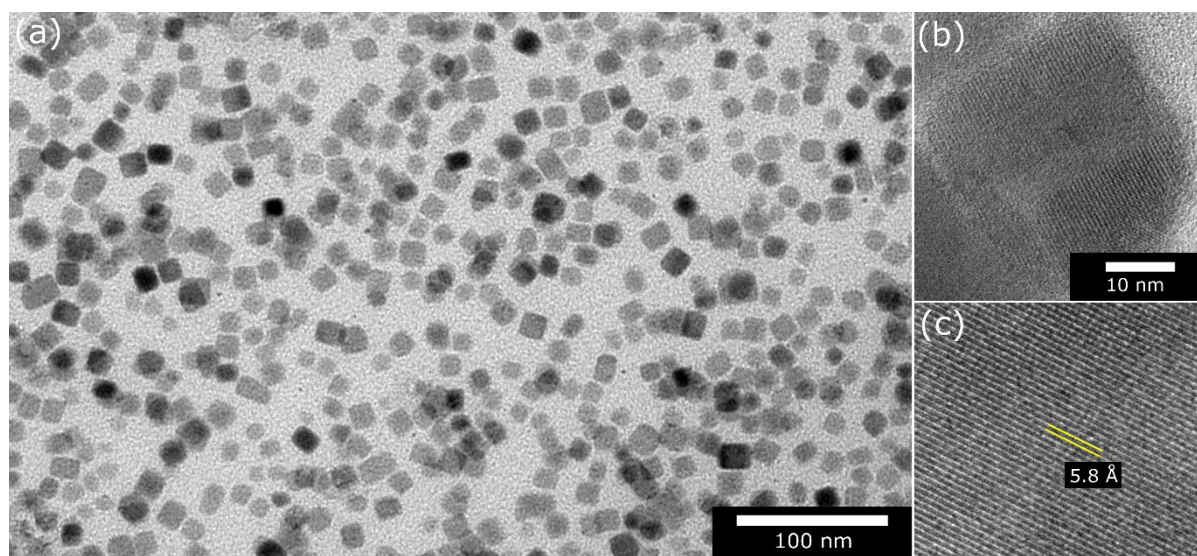


Figure 4.1. TEM images of RT-CsPbBr₃ QDNCs. (a, b) Top-view revealing their size distribution and shape. (c) HR-TEM image showing the separation between lattice planes in a cube structure.

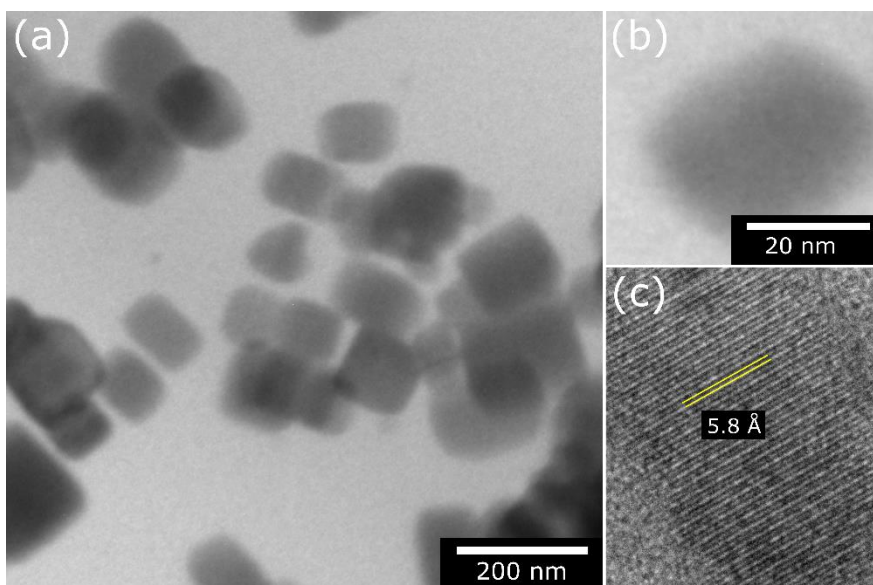


Figure 4.2. TEM images of RT-FAPbBr₃ QDNCs. (a, b) Top-view revealing their size distribution and shape. (c) HR-TEM image showing the separation between lattice planes in a cube structure.

Furthermore, XRD was also implemented for their characterisation, and the results were compared with their corresponding control QDNCs (labelled herein as con-CsPbBr₃ and con-FAPbBr₃ QDNCs), which were synthesized at elevated temperatures via the hot-injection approach (oleic acid/oleylamine ligand combination).^[151] Figure 4.3 illustrates XRD patterns that show the cubic perovskite phases for both inorganic and organic-inorganic type. Compared to the control, RT synthesized QDNCs have better-defined peak intensities. This finding indicates that the level of crystallinity was higher.

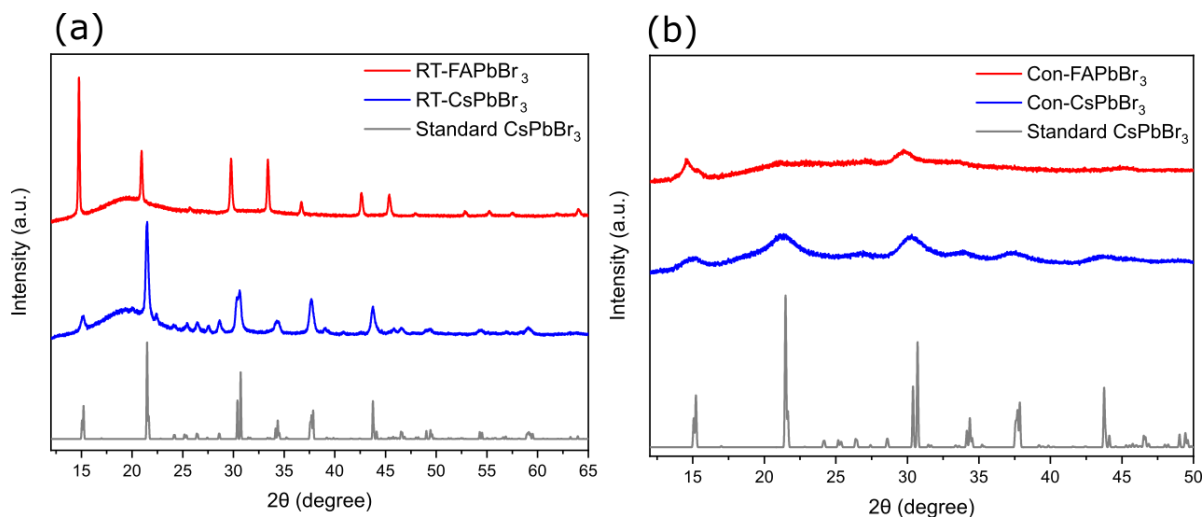


Figure 4.3. XRD patterns for (a) RT-FAPbBr₃ and RT-CsPbBr₃ QDNCs. (b) con-FAPbBr₃ and con-CsPbBr₃ QDNCs. The standard perovskite phase for FAPbBr₃ can be seen in reference.^[170]

4.3.2 Optical characteristics of quantum dot nanocrystals

The absorption properties of QDNCs were investigated using absorption spectroscopy. Figures 4.4a and b illustrate UV/Vis absorption spectra for RT-FAPbBr₃ and RT-CsPbBr₃ QDNCs. While for both types, a peak at the first excitonic transition (around 500 nm) can be observed, RT-CsPbBr₃ QDNCs exhibited an additional electronic transition located at around 375 nm, which is a characteristic of high-quality nanomaterials.^[171] The same feature was already observed for CsPbBr₃ QDNCs by other researchers in the field,^[151] however, it has not yet been reported for FAPbBr₃ QDNCs, which is in line with the results presented herein. This phenomenon can be related to bigger sizes of the latter type of QDNCs, which hinder the possibility of other transitions being observed.^[172] In addition, as already noted from the TEM characterisation, RT-CsPbBr₃ QDNCs exhibited a more uniform size distribution, which could be an additional factor causing the second transition to be more

defined.^[173] Light emission characteristics of QDNCs were examined with a fluorometer, as illustrated in Figure 4.4. Compared to the control (energy intensive approach), RT synthesized QDNCs exhibited similar fwhm values, with emission line widths of ≈ 19 nm for RT-FAPbBr₃ QDNCs, and ≈ 14 nm for RT-CsPbBr₃ QDNCs. However, the cation type (size difference) affected the wavelength of light emission with RT-CsPbBr₃ QDNCs emitting at 519 nm, and RT-FAPbBr₃ QDNCs exhibiting a bathochromic shift in the emission spectrum (532 nm). According to the International Commission on Illumination (CIE) and the International Telecommunication Union (ITU), there are three main emission peaks for display applications, which are located at 467 nm, 532 nm, and at 630 nm.^[174] As the results here indicate, the emission peak for RT-FAPbBr₃ QDNCs is explicitly in line with one of these three emission peaks, which renders this type promising for future applications.

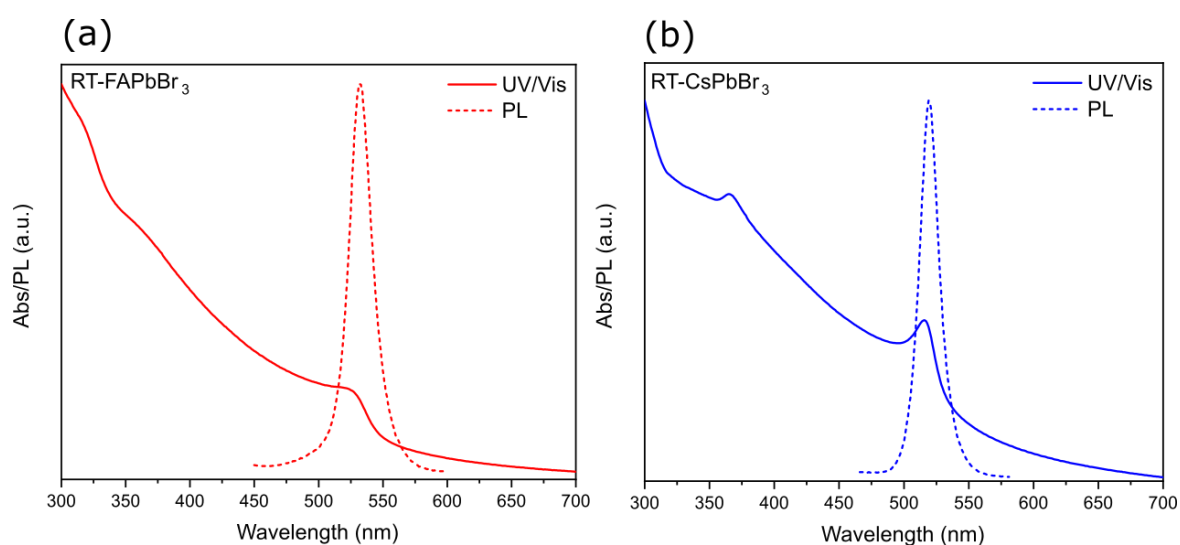


Figure 4.4. UV/Vis (solid line) and PL (dotted line) characteristics of (a) RT-FAPbBr₃ and (b) CsPbBr₃ QDNCs.

The quantum-confinement properties of QDNCs were investigated by performing syntheses at various temperatures (between RT to 130 °C) to obtain different sizes. It

is noteworthy to mention that both precursor solutions were at the same temperature at the time of injection. Different sizes of QDNCs have different values of energy gap (bandgap), which is a fundamental principle behind quantum confinement.^[175] Bigger sizes of QDNCs exhibit lower bandgaps compared with their smaller sizes with blue-shifted emission. The extent of quantum confinement in perovskite QDNCs is related to their cation type. For instance, light tuning in con-FAPbBr₃ QDNCs can be achieved in the wavelength range of ≈ 65 nm, as opposed to the range of ≈ 35 nm for con-CsPbBr₃ QDNCs.^[176] However, RT-FAPbBr₃ and RT-CsPbBr₃ QDNCs did not show any noticeable light emission variations at synthesis temperatures ranging from RT to 100 °C (Figure 4.5). This anomaly can be explained by their large sizes, where despite being synthesized at low temperatures, the size was still higher than the exciton Bohr radius. The requirement to access the quantum confinement regime is that the size of a QDNC is within the same order as the size of the exciton Bohr radius, which via this synthesis pathway was not possible to achieve.^[154]

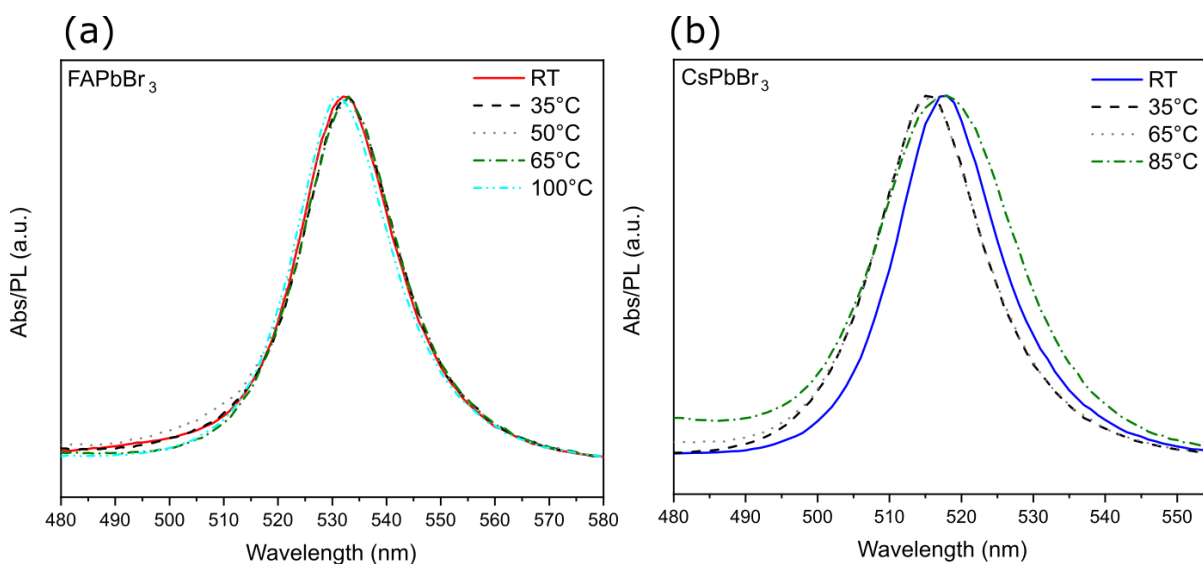


Figure 4.5. PL spectra for (a) FAPbBr₃ and (b) CsPbBr₃ QDNCs synthesized at different temperatures.

Nevertheless, different synthesis temperatures influenced PLQYs for both types of QDNCs, as shown in Figure 4.6. It was revealed that the high temperature conditions negatively influenced PLQYs, as higher values were obtained under RT. In addition, a phosphine-based ligand combination resulted in being more favourable for RT-FAPbBr₃ QDNCs, since the values of up to 50% were obtained, as opposed to RT-CsPbBr₃ QDNCs, where the highest PLQYs were in the range < 25%. When these nanomaterials were synthesized at elevated temperatures of up to 100 °C, PLQYs were significantly lower. Since the emission characteristics of QDNCs are closely related, with the ability of capping ligands to passivate their surfaces, the results suggest that elevated temperatures generate the creation of in-gap trap states, which are known to induce non-radiative recombination processes and thus low PLQYs.^[177]

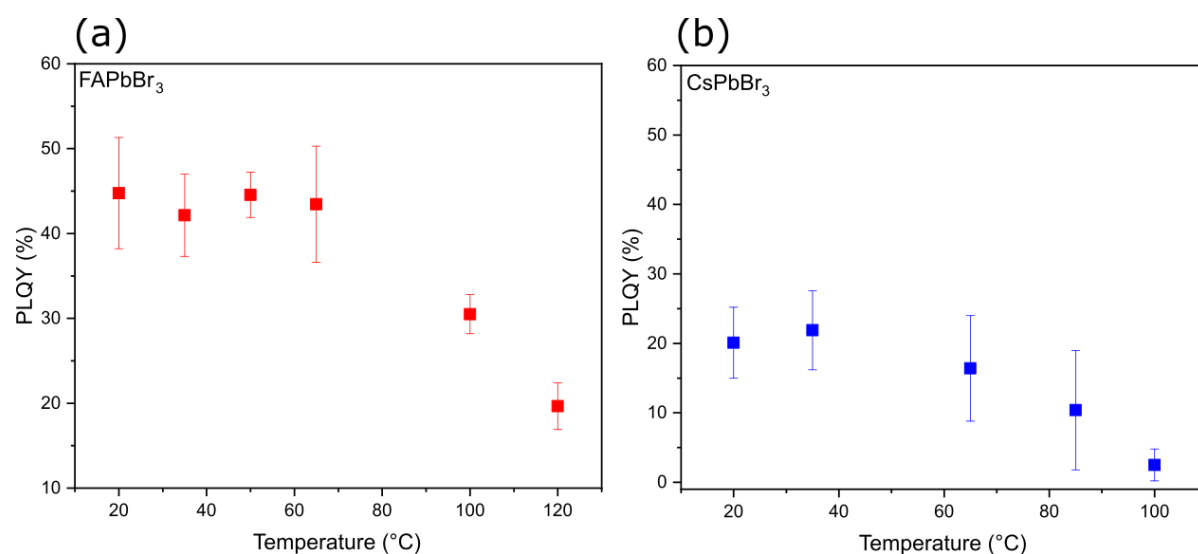


Figure 4.6. Trends in PLQYs as a function of the synthesis temperatures for (a) FAPbBr₃ and (b) CsPbBr₃ QDNCs.

To visualize the trends discussed above, Figure 4.7 shows the photographs for both types of QDNCs synthesized at various different temperatures, under the excitation of 365 nm (Figures 4.7a and b) and without light excitation (Figures 4.7c and d). The

resulting colloidal solutions turned out to be dissimilar, as an orange colloidal solution formed for RT-FAPbBr₃ and a lime green colloidal solution for RT-CsPbBr₃ QDNCs.

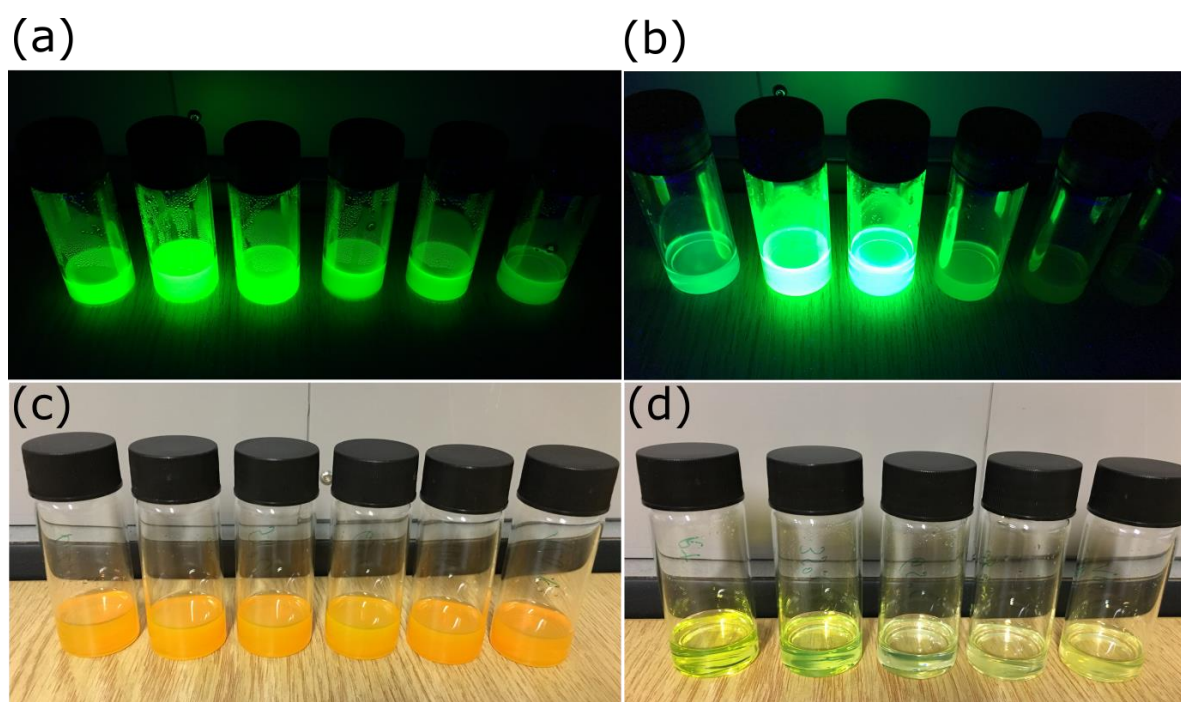


Figure 4.7. Photographs of (a, c) FAPbBr₃ and (b, d) CsPbBr₃ QDNCs synthesized at different reaction temperatures, as illustrated in Figures 4.6. (a) and (b) show colloidal solutions under light excitation (365 nm) and (c, d) without light excitation.

As reported by Manna et al.,^[177] there is an influence of the concentration gradient of the cation precursor solution on the QDNC surface ligand capping. Therefore, similar experiments were performed herein, and Figure 4.8 shows how different concentrations of the formamidinium acetate solution influenced PLQYs of RT-FAPbBr₃ QDNCs. The results revealed that the concentration increase hindered PLQYs and that the best performance was obtained with a 0.1 mol/L concentration. The same measurements were also performed for RT-CsPbBr₃ QDNCs, however, as Cs₂CO₃ is not highly soluble at low temperatures, clear agglomerate traces of the undissolved powder were noticed at the bottom of the vials. Therefore, such synthesis

conditions proved unreliable for observing possible concentration effects on PLQYs and so the results are not presented in this work. Moreover, the influence of different DiOPA concentrations in the anion precursor solution were also investigated, but no trends in PLQYs were observed. Since other researchers in the field reported on PLQYs of con-FAPbBr₃ and con-CsPbBr₃ QDNCs approaching near unity (high temperature approach), values discussed in this report appear to be low.^[178] This can be attributed to non-ideal interactions between the surface ligands and the NC core, which leads to poor passivation, and as such, the results are not surprising. As reported by Milliron et al.^[179] for MgO NCs, TOPO as a capping ligand leads to lower PLQYs when compared to other alternatives, for example benzyl ether.

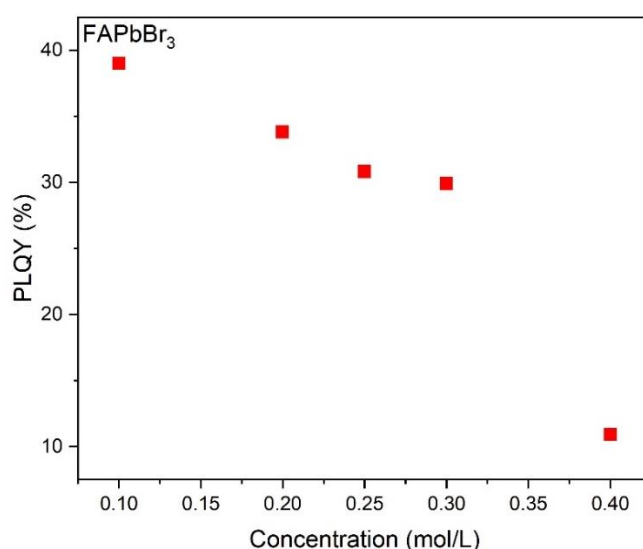


Figure 4.8. PLQYs as a function of the concentration of the formamidinium acetate precursor solution for FAPbBr₃ QDNCs.

To explore the dynamic processes in QDNCs, time-resolved spectroscopy was employed. In order to present data, tri-exponential and bi-exponential decay fittings were used for RT and con-FAPbBr₃ and con-CsPbBr₃ QDNCs, respectively. Figure 4.9 illustrates the decay dynamics, and Tables 4.1 and 4.2 show time-resolved PL

data. As reported by other authors,^[180] the size range of QDNCs can influence their emission decay lifetimes and for bigger sizes, higher lifetimes are obtained (small sizes → lower lifetimes). This can be attributed to charge diffusion lengths, where longer lengths exhibit slower bimolecular recombination and thus larger QDNCs will have longer lifetimes.^[180,181] The results of this study did not show any exceptions, since both types of perovskite QDNCs synthesized at RT had longer average emission decay lifetimes, as opposed to control QDNCs that exhibited shorter lifetimes. Their size differences were determined from the XRD patterns (Figure 4.3) using the Scherrer equation, which showed that RT-FAPbBr₃ QDNCs were ≈2.4 times larger compared with their respective control, while RT-CsPbBr₃ QDNCs were ≈3.1 times larger in comparison with con-CsPbBr₃ QDNCs. Therefore, average PL decay lifetimes for the former type were 28.5 ns for RT and 12.2 ns for control, while for the latter type they were 34.8 ns for RT and 9.7 ns for control. Since the synthetic procedure to make RT QDNCs is undoubtedly easier and cheaper than a hot-injection approach, and while having larger PL lifetimes is beneficial for optoelectronic applications, they can be a good alternative for use in various applications.

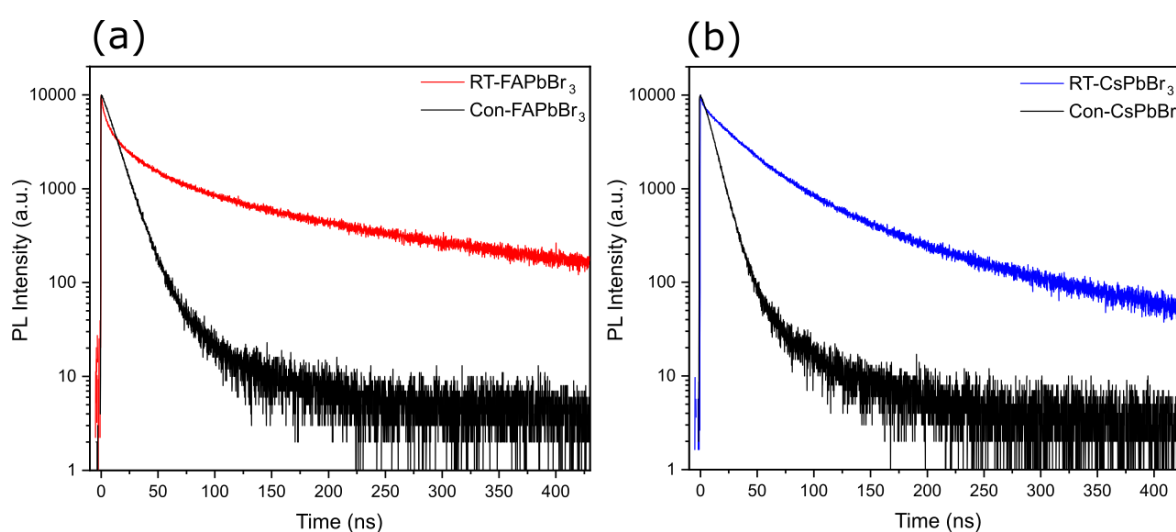


Figure 4.9. PL emission lifetimes for colloidal solutions of (a) FAPbBr₃ and (b) CsPbBr₃ QDNCs.

Table 4.1. Time-resolved PL results for colloids of RT-FAPbBr₃ and RT-CsPbBr₃ QDNCs. To fit the results, the following equation was used: $(y = y_0 + A_1e^{-x/\tau_1} + A_2e^{-x/\tau_2} + A_3e^{-x/\tau_3})$ and the average lifetimes were determined via: $\sum(a_i\tau_i)$.

	A ₁	τ ₁ (ns)	A ₂	τ ₂ (ns)	A ₃	τ ₃ (ns)	T _{avg} (ns)
RT-FAPbBr ₃	4189.0	2.8	3478.9	18.7	1720.5	110.9	28.5
RT-CsPbBr ₃	2084.9	1.8	6066.2	29.4	1803.9	90.9	34.8

Table 4.2. Time-resolved PL results for colloids of con-FAPbBr₃ and con-CsPbBr₃ QDNCs. To fit the results, the following equation was used: $(y = y_0 + A_1e^{-x/\tau_1} + A_2e^{-x/\tau_2})$ and the average lifetimes were determined via: $\sum(a_i\tau_i)$.

	A ₁	τ ₁ (ns)	A ₂	τ ₂ (ns)	T _{avg} (ns)
Con-FAPbBr ₃	10206.7	11.8	96.9	52.5	12.1
Con-CsPbBr ₃	11001.1	9.3	90.9	50.8	9.7

4.3.3 Composition and ligand binding of quantum dot nanocrystals

To investigate the surface characteristics of QDNCs, XPS was used, which allowed the determination of the elements present. Figures 4.10 and 4.12 illustrate elements that were identified for RT-FAPbBr₃ QDNCs, and Figures 4.11 and 4.12, show similar elements on the surface of RT-CsPbBr₃ QDNCs. Elements, for instance carbon, nitrogen, oxygen, lead, bromine, caesium, and phosphorous were identified and correlated with the capping ligands and the particular nanocrystal core.

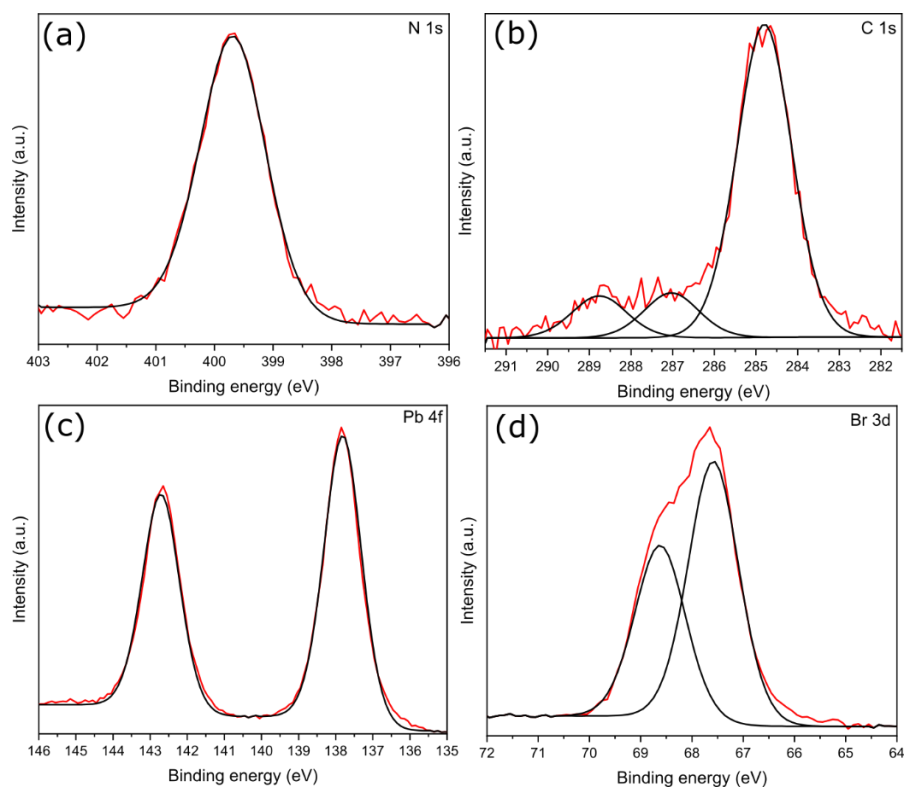


Figure 4.10. High-resolution XPS spectra of elements (a) N 1s, (b) C 1s, (c) Pb 4f, and (d) Br 3rd, which were identified on the surface of RT-FAPbBr₃ QDNCs.

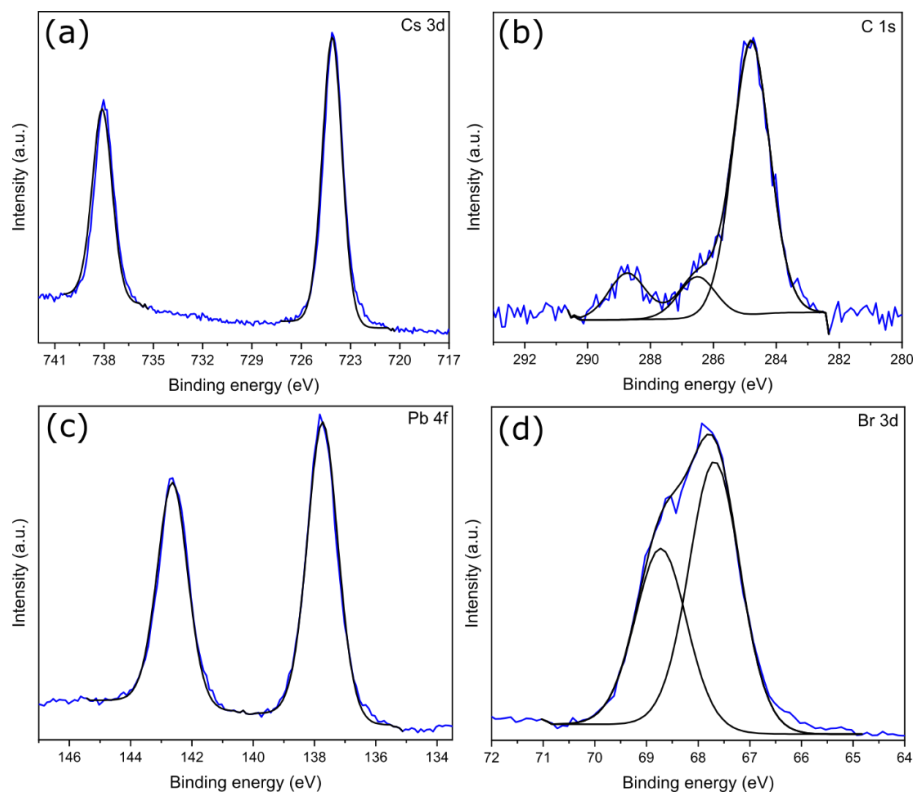


Figure 4.11. High-resolution XPS spectra of elements (a) Cs 3d, (b) C 1s, (c) Pb 4f and (d) Br 3rd, which were identified on the surface of RT-CsPbBr₃ QDNCs.

Interactions between the capping ligands and the perovskite core were further analysed using P 2p and O 1s spectra (Figure 4.12). P 2p spectra revealed that no phosphorous in zero oxidation state was present, since no peaks were observed in the range between 129 – 131 eV for both types of QDNCs. Nevertheless, a broad band can be seen at higher binding energies (131 – 135 eV), which is an indication of phosphorous being in a higher oxidation state. This broad band was deconvoluted into two separate peaks, where each corresponds to a particular bonding. To obtain information about the bonding mechanism, an O 1s spectrum was used, which was likewise deconvoluted into two separate peaks (Figures 4.12b and d). The first peak present at lower binding energies (at 531 eV for RT-FAPbBr₃, and at 532 eV for RT-CsPbBr₃ QDNCs), was identified as oxygen that did not participate in the bonding between the capping ligands and the NC core, and was thus part of the P = O ligand bond.^[182] On the other hand, the second deconvoluted peak, present at 532 eV for RT-FAPbBr₃ and at 533 eV for RT-CsPbBr₃ QDNCs, was determined to be part of the bonding that was formed on the QDNC surfaces and was thus identified as the Pb-O-P bond.^[183] Therefore, these results suggest that the P=O group (present on both types of ligands) is the binding centre for the attachment of ligands on the nanocrystal core, on the lead element of the QDNC structure. These interactions were further investigated by implementing FTIR, as discussed in the sections below.

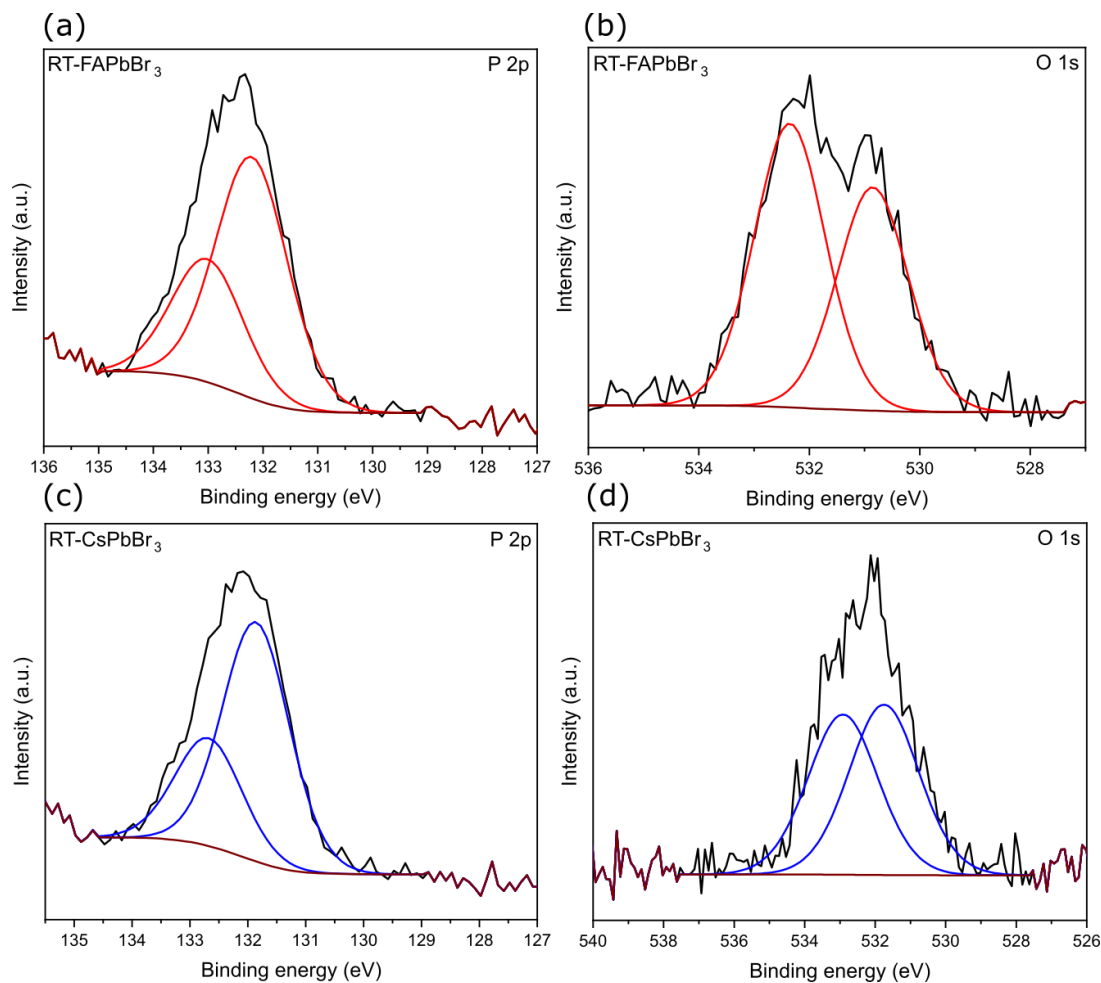


Figure 4.12. High-resolution XPS spectra of elements (a) P 2p, (b) O 1s for RT-FAPbBr₃ and (c) P 2p, (d) O 1s for RT-CsPbBr₃ QDNCs.

As previously discussed, PLQYs for RT synthesized QDNCs were shown to be temperature dependent. Therefore, XPS was used to investigate possible changes on their surfaces at different synthesis temperatures. Elemental ratios between N:Pb and Br:Pb on the surface of RT-FAPbBr₃ QDNCs can be seen in Figure 4.13. By increasing the synthesis temperature, both elemental ratios increased, indicating that a higher temperature reduced the amount of Pb that was present. These trends were further examined via the atomic ratios of Pb:P. As opposed to the synthesis performed at 100 °C (Pb:P = 1:20), RT synthesis resulted in atomic ratios of 1:(2.9-3.9). Such results indicate that the atomic ratios of the constituent elements of the perovskite crystal

structure were modified as a function of temperature, which most likely influenced the trends that were observed for PLQYs.

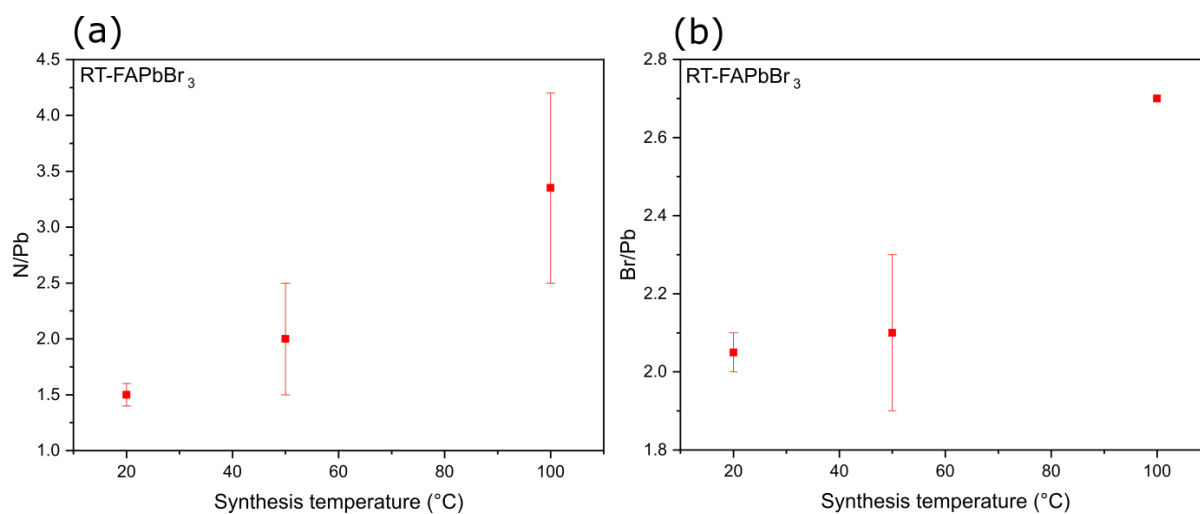


Figure 4.13. Atomic ratios of (a) N/Pb and (b) Br/Pb for RT-FAPbBr₃ QDNCs.

In contrast to, the atomic ratios of Br:Pb for RT-CsPbBr₃ QDNCs did not follow the same pattern as above, meaning that a temperature dependency cannot be expanded towards all types of perovskite QDNCs (Figure 4.14).

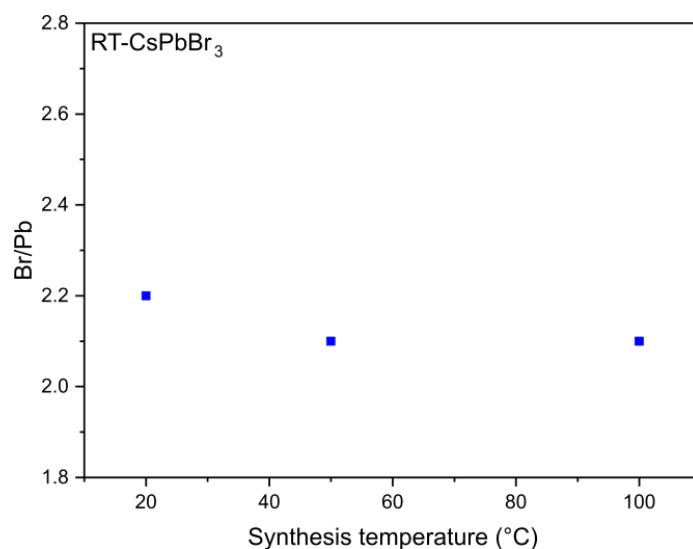


Figure 4.14. Br:Pb atomic ratios for RT-CsPbBr₃ QDNCs.

The strength of the ligand binding and the nature of the ligand removal after the purification procedures, were both investigated by determining the atomic ratios of Pb:P before and after the addition of an antisolvent. The atomic ratio (Pb:P) determined for RT-FAPbBr₃ was (1.2-1.7):1, and for RT-CsPbBr₃ QDNCs was (1.8-2.2):1. Compared to the ratios before the antisolvent treatment (see above), the amount of organic ligands notably decreased on the surface of QDNCs after the purification, indicating that the Pb-O-P bond can be considered highly dynamic and easy to remove from the QDNC shell.

4.3.4 Interactions between quantum dot nanocrystals and their ligands

In addition to XPS, interactions between the phosphine-based surfactants and the QDNC core were also studied by implementing FTIR. Figure 4.15 shows the structural formulas for both ligands that were used (TOPO and DiOPA), and their FTIR spectra can be seen in Figures 4.16 and 4.17.

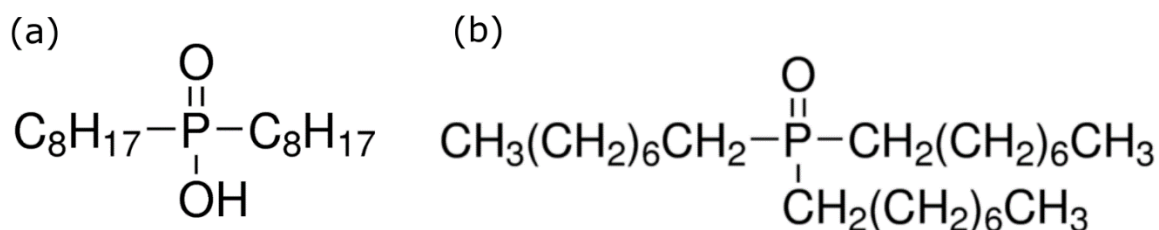


Figure 4.15. Structures of (a) DiOPA and (b) TOPO molecules.

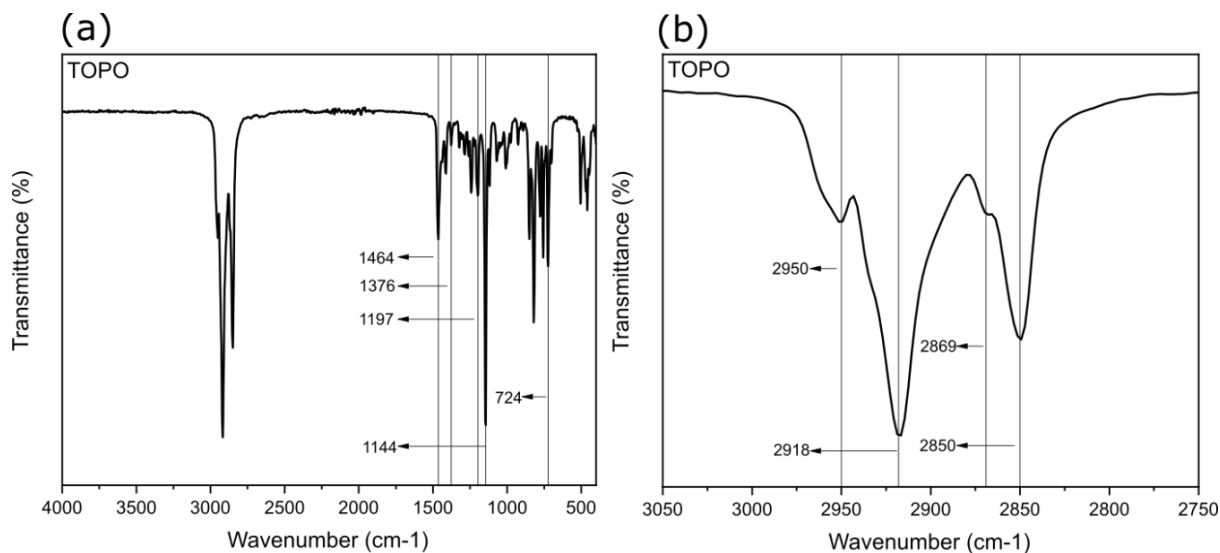


Figure 4.16. FTIR spectra for TOPO in the wavelength range (a) between 4000 – 500 cm^{-1} and (b) between 3050 – 2750 cm^{-1} .

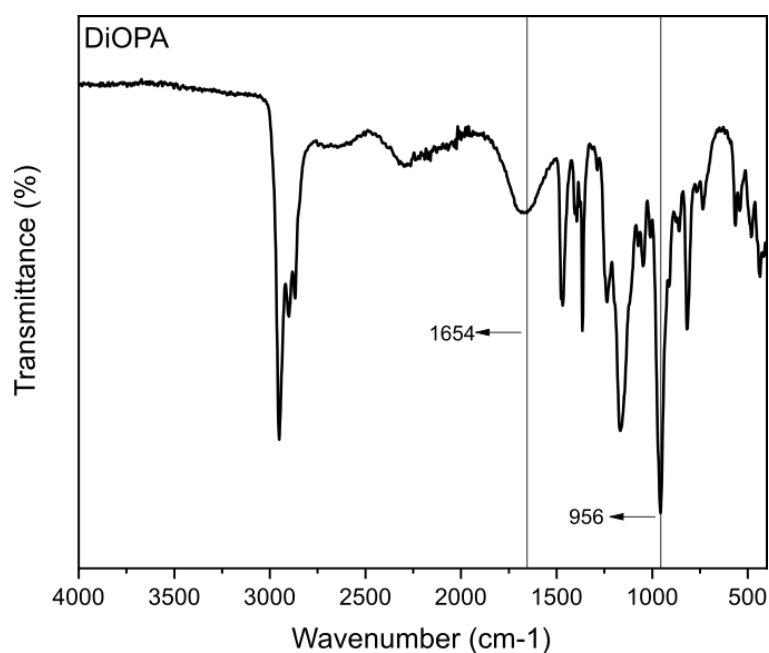


Figure 4.17. FTIR spectra for DiOPA in the wavelength range between 4000 – 500 cm^{-1} .

The main signals were successfully identified, and the spectral assignments at particular wavelengths can be seen in Table 4.3 for TOPO and Table 4.4 for DiOPA.

Table 4.3. Identified FTIR characteristic absorption peaks from the spectrum of TOPO, where the symbols ν , δ , and γ refer to stretching, in-plane deformation, and out-of-plane deformation, respectively. The subscripts “as” and “s” are related to asymmetric or symmetric stretching, respectively.

Wavenumber (cm ⁻¹)	2950	2918	2869	2850	1464	1376	1197	1144	724
Group	$\nu_{\text{as}}(\text{CH}_3)$	$\nu_{\text{as}}(\text{CH}_2)$	$\nu_{\text{s}}(\text{CH}_3)$	$\nu_{\text{s}}(\text{CH}_2)$	$\delta(\text{CH}_2)$	$\delta_{\text{s}}(\text{CH}_3)$	$\delta(\text{CH}_2)$	$\nu(\text{P}=\text{O})$	$\gamma(\text{CH}_2)$

Table 4.4. Identified FTIR characteristic absorption peaks from the spectrum of DiOPA that cannot be observed on the spectrum of TOPO.

Wavenumber (cm ⁻¹)	1654	956
Group	$\nu(\text{P-OH})$	P-OH

Further evaluation of the ligand binding to the perovskite core was performed by analysing FTIR spectra for RT-FAPbBr₃ and RT-CsPbBr₃ QDNCs, as illustrated in Figure 4.18. The results revealed that the main changes between the FTIR spectra of ligands and FTIR spectra of QDNCs occurred for the signal assigned to the P=O stretching vibration, which is located around the region between 1100 – 1200 cm⁻¹. As reported in other studies,^[184] where TOPO was used as a binding molecule, the formation of coordination composites from its P=O functional group, results in the alterations of the position for this signal; in particular, the position for the P=O stretching vibration spans to lower wavenumbers. Such a red shift indicates that a bond is formed through a TOPO functional group.^[179] The explanation for this shift is related to the transfer of electron density from phosphorous to a more electronegative element, such as oxygen. Based on the data from the FTIR spectra for ligands and QDNCs, it has been determined that the P=O stretching peak has broadened and altered from 1144 cm⁻¹ (TOPO and DiOPA) to 1120 cm⁻¹ (QDNCs). This indicates that

a bond was formed between them; specifically, a P=O functional group was broken and a new Pb-O-P bond was formed that attached a ligand to the QDNC core.^[185] While reports of such interactions are novel for perovskite QDNCs, a similar mechanism had already been observed previously for cadmium-based quantum dots, for instance, CdSe^[186,187] and CdS^[184] quantum dots.

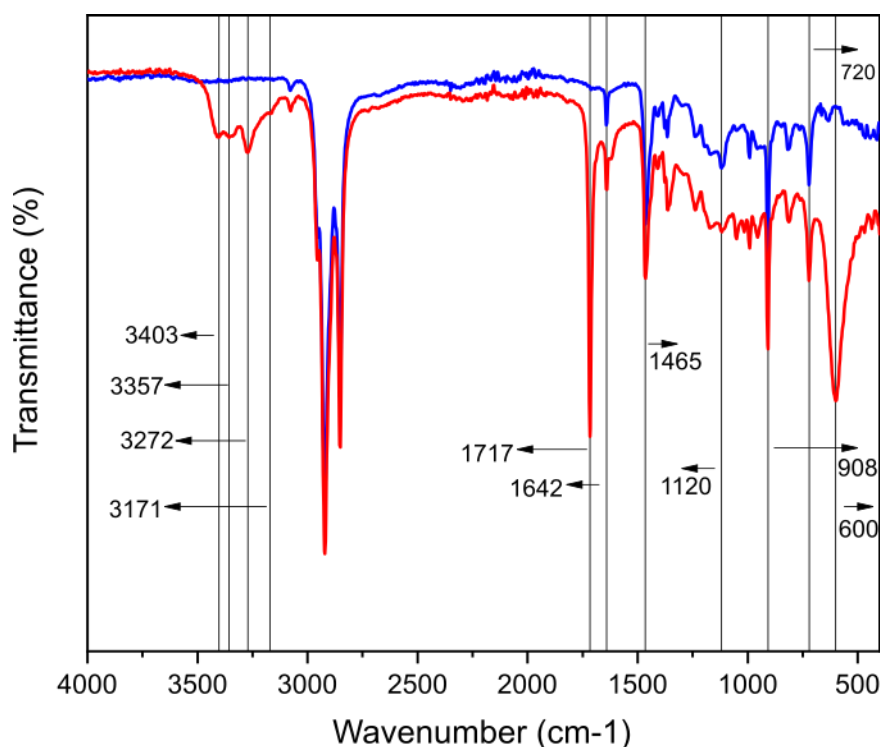


Figure 4.18. FTIR spectra for RT-CsPbBr₃ (blue lines) and RT-FAPbBr₃ (red lines) QDNCs in the wavelength range 4000 – 500 cm⁻¹.

Compared to TOPO, the structural formula for a DiOPA ligand differs by having an additional functional group (P-OH) attached to the phosphorous element. The interaction of this group with the surface of QDNCs was further examined based on their FTIR spectra. As illustrated in Table 4.4, two peaks (at 1654 cm⁻¹ and 956 cm⁻¹) that are additionally located on the FTIR spectrum of DiOPA (Figure 4.17), became altered on the spectrum of QDNCs (Figure 4.18). Specifically, they red-shifted and

were identified at 1642 cm^{-1} for the P-OH stretching and at 908 cm^{-1} for the P-OH bending (Figure 4.18). A DiOPA ligand has previously been used for other applications, for instance, in the field of supercritical fluids, where interactions with copper complex compounds were reported (i.e. a shift of wavenumbers to lower frequencies).^[188] Since similar shifts have been seen in this work, it is concluded that they are a result of the binding to QDNCs via lead. Furthermore, other peaks that can be seen in Figure 4.18 were also investigated. For example, strong absorption occurred slightly below 3000 cm^{-1} , which was determined to be the result of C-H absorption bands and bonding between sp^3 carbon and hydrogen. Figure 4.19 shows a closer view of the FTIR spectrum range around that region. It can be seen that the absorption bands present are very similar between the spectra of ligands and QDNCs and were assigned to the stretching vibrations of $-\text{CH}_2$ and $-\text{CH}_3$, respectively. The absorption around 2954 cm^{-1} and 2921 cm^{-1} was related to the dissymmetric stretching vibrations of $-\text{CH}_3$ and $-\text{CH}_2$, and the absorption band at 2852 cm^{-1} was a result of the symmetric stretching vibrations of $-\text{CH}_2$.

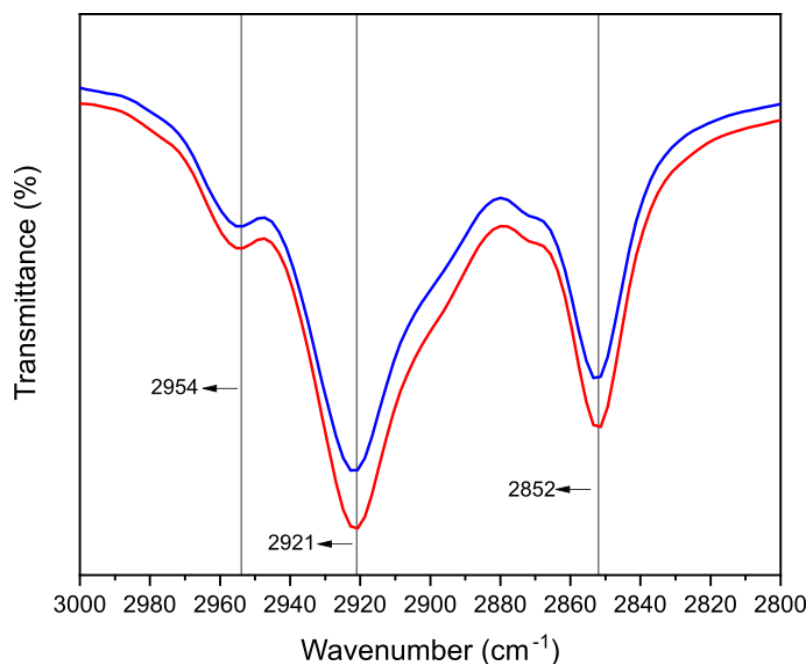


Figure 4.19. FTIR spectra for RT-CsPbBr₃ (blue lines) and RT-FAPbBr₃ (red lines) QDNCs in the wavelength range between 3000 – 2800 cm⁻¹.

The peak at 1465 cm⁻¹ (Figure 4.18) was attributed to the scissoring band of -CH₂.^[184] FTIR analysis further revealed that the capping ligands consisted of at least four-carbon chains, shown by the observation of an absorption peak at 720 cm⁻¹. This can be attributed to the presence of octyl groups from the ligands, which bind to the QDNC core.

Since the hybrid organic-inorganic type of QDNCs (FAPbBr₃) consists of an organic cation group, as can be seen in Figure 4.20, extra signals were observed on the FTIR spectrum of RT-FAPbBr₃ QDNCs (Figure 4.18). However, it should be noted that a different cation type did not have any influence on the position of absorption peaks assigned to the organic ligands. In the frequency range 3400 – 3100 cm⁻¹, four signals appeared that cannot be observed on the spectrum of RT-CsPbBr₃ QDNCs. They were assigned to the quadruple N-H stretching vibrations of the FA⁺ cation. Moreover, a strong absorption band appeared at 1717 cm⁻¹, which, as reported by Chaykovsky

et al.,^[189] can be attributed to the symmetric stretching vibrations of C=N. Nevertheless, in a recent computational study performed by Oliver et al.,^[190] the same peak was identified to be the C-N antisymmetric stretching vibration. Additionally, an absorption band located at approximately 600 cm⁻¹ was associated with the N-H wagging and C-H rocking of bonds.^[191]

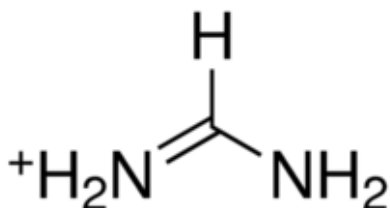


Figure 4.20. A structural formula of the formamimidinium cation.

To determine the affinity of ligand binding to the QDNC core, FTIR spectra of non-purified and purified (the addition of polar solvents) QDNCs were obtained, as illustrated in Figure 4.21. The results revealed that RT-FAPbBr₃ QDNCs signals previously assigned to the -CH₃ groups at wavenumbers of ≈3000 cm⁻¹ and to the -CH₂ groups at ≈1460 cm⁻¹, significantly decreased after the purification treatment. Moreover, a signal at the absorption band of 720 cm⁻¹, which was a result of the long chain organic compounds, essentially disappeared, which is an indication that the amount of organics significantly decreased. The same was also noted for the P-OH stretching peak at around 1640 cm⁻¹; however, the absorption band located at 908 cm⁻¹ (P-OH bending) can still be observed. Therefore, results indicate that the phosphine-based ligands can be removed from the RT-FAPbBr₃ QDNC surfaces without difficulty, and that their binding is highly dynamic.

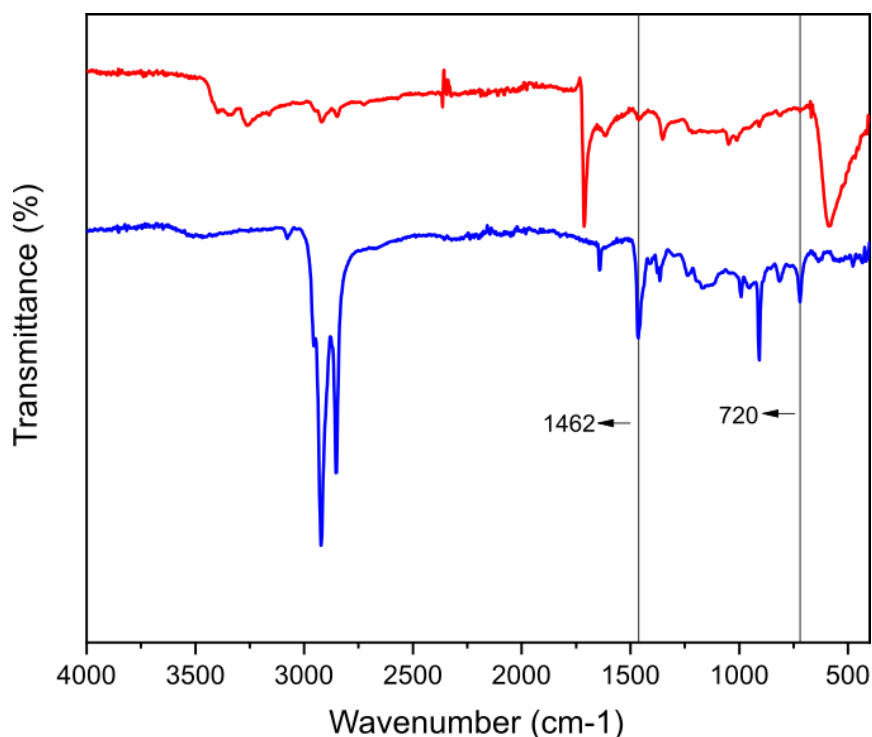


Figure 4.21. FTIR spectra for RT-CsPbBr₃ (blue lines) and RT-FAPbBr₃ (red lines) QDNCs in the wavelength range between 4000 – 500 cm⁻¹ after the purification treatment (the addition of polar solvents).

As opposed to the organic-inorganic hybrid, ligands capped on all-inorganic (RT-CsPbBr₃) QDNCs were not removed to such a large extent after the addition of polar solvents. Figure 4.22 shows the comparison between non-purified and purified RT-CsPbBr₃ QDNCs. A slight decrease of peak intensities that were previously assigned to the organic ligands can be observed, however all of them were still considerable. This is the opposite to what was observed for RT-FAPbBr₃ QDNCs.

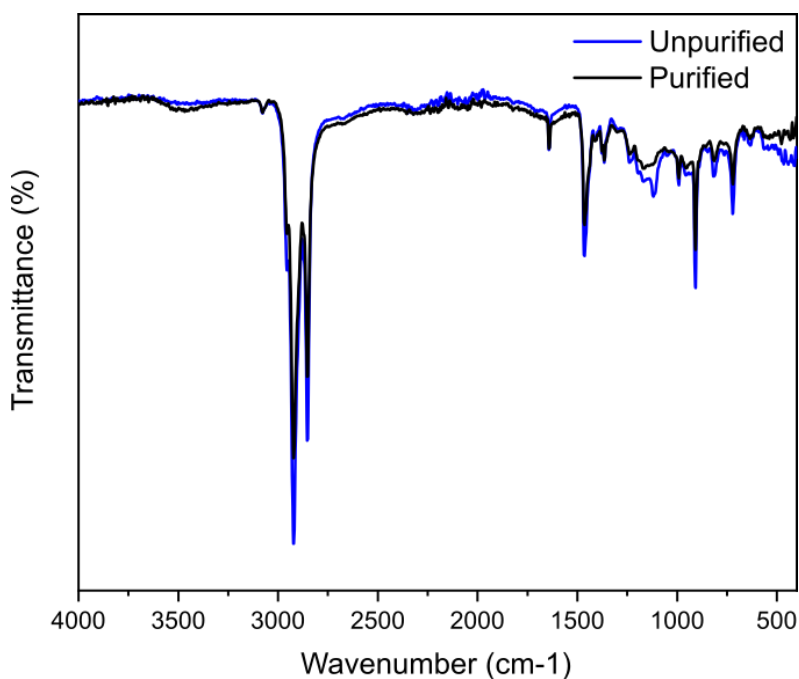


Figure 4.22. FTIR spectra of RT-CsPbBr₃ QDNCs that were not subject to purification (blue lines) and the spectra of QDNCs that were purified (black lines).

In addition to the FTIR measurements, thermal gravimetric analysis (TGA) was performed to investigate the removal characteristics of phosphine-based ligands after the addition of polar solvents. Therefore, purified control (oleic acid/oleylamine) and phosphine-capped QDNCs were compared (Figure 4.23). Both types of QDNCs were purified using the same quantities and types of polar solvents, as described in the experimental section. As can be seen in the TGA curves in Figure 4.23, there is a noticeable mass difference between them in the temperature related profile, and phosphine-based ligands were easier to remove. Up to approximately 450 °C, only organic ligands disintegrate; whereas a temperature increase above 550 °C causes the decomposition of the perovskite structure. As the results indicate, con-FAPbBr₃ and con-CsPbBr₃ QDNCs lost noticeably more weight than the same type of QDNCs capped with the phosphine-based ligands. Specifically, for FAPbBr₃ QDNCs there was a mass difference of 12.5%, while for CsPbBr₃ QDNCs it was 12.9%. Therefore, an

oleic acid/oleylamine ligand combination is more potent in antisolvent washing compared to the combination of TOPO/DiOPA. Such observations are in line with the findings obtained by implementing the XRD technique, where a higher level of crystallinity was observed for the phosphine capped QDNCs. While the removal of insulating ligands from the surface of QDNCs can be an advantage in terms of charge transport properties for optoelectronic applications, it is only beneficial if the performance metrics do not diminish. Since PLQYs for both types, namely control and RT synthesized QDNCs, decreased after the ligand removal, this suggests that there is a need to find alternative ligand combinations that will allow good charge conductivity, together with retaining high optoelectronic performance. Nevertheless, the findings presented here can be valuable for future work in the field of QDNC ligand exchange studies, which will aim towards having total control of the surface ligand binding in QDNCs.

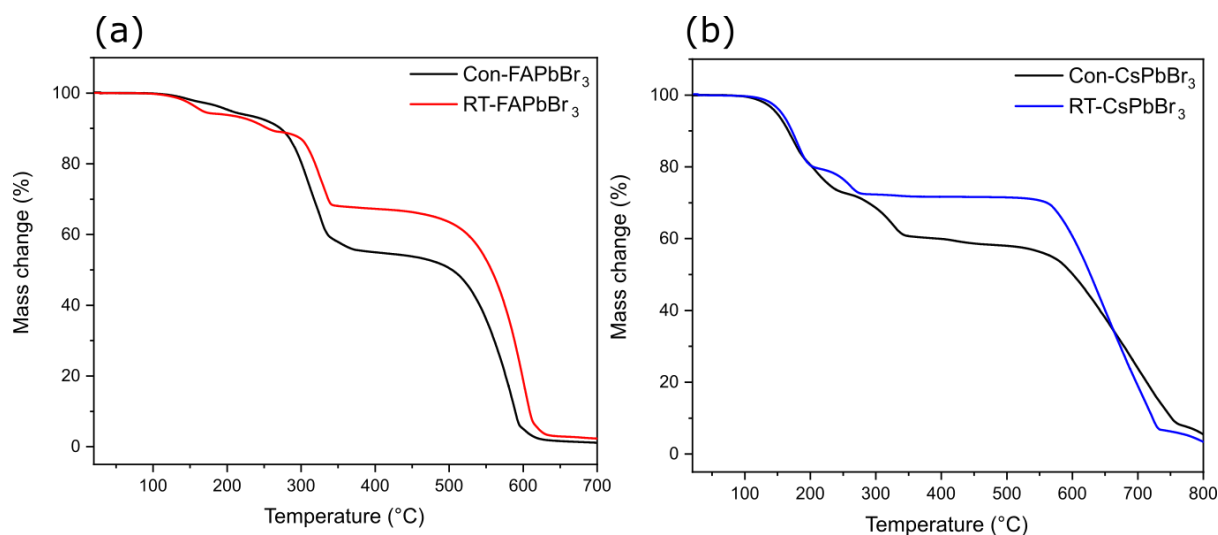


Figure 4.23. TGA graphs for purified (a) con-FAPbBr₃ and RT-FAPbBr₃ QDNCs, together with (b) con-CsPbBr₃ and RT-CsPbBr₃ QDNCs.

4.4 Conclusion

In summary of this section, a new synthesis approach was developed to allow FAPbBr_3 and CsPbBr_3 QDNCs to be synthesized at RT using a ligand combination of TOPO/DiOPA, instead of typically employed amines and carboxylic acids. Moreover, phosphine-based ligands enabled the solvation of precursor compounds in an industrially compatible solvent, for instance, octadecene. While RT synthesis routes already exist (LARP approach), they typically require the use of toxic polar solvents (DMF), preventing them from being used in the production of large batches of QDNCs. Experiments have revealed that it is also possible to synthesize phosphine capped QDNCs at elevated temperatures; however, compared to the RT approach optoelectronic performance metrics deteriorate and thus RT synthesis is considered more beneficial. Furthermore, phosphine-based ligand interactions with the QDNC core were investigated using various types of characterisation techniques, which revealed that a Pb-O-P bond was formed, attaching ligands to the perovskite core. When RT synthesized QDNCs were purified with polar solvents, their PLQYs decreased. However, as opposed to the approach that uses a ligand combination of carboxylic acids and amines, phosphine-based ligands are easier to remove from the QDNC surfaces, indicating that their binding is highly dynamic. Overall, the possibility to synthesize such high-quality QDNCs at RT offers several advantages over the traditional hot-injection approach.

Chapter 5

Conclusion

5. Conclusion

5.1 Summary of results

To tackle greenhouse gas emissions, converting solar energy into electricity to replace fossil fuel combustion is a mandatory approach that will have to take place imminently. Since this is a clean and environmentally friendly method of energy generation, using it to replace the consumption of oil or coal can solve many ecological problems worldwide. With the discovery of DSSCs approximately 30 years ago, many researchers at that time predicted that, by now, this type of solar cells would have already been commercialized and widely employed to generate clean energy. As a result of their low-cost fabrication, it was expected that DSSCs could compete with other solar technologies. However, despite more than a thousand scientific publications and extensive research funding, their progress has not been as expected, and thus there are still severe limitations that impede their commercial employment. Over the last decade, silicon or CIGS solar cells were further improved and became more efficient at a decreased cost of fabrication. Therefore, the performance of DSSCs in comparison with other technologies became even more inferior. Currently, the main disadvantages preventing their further development are low efficiency and lack of long-term outdoor stability. While the theoretical efficiency limit is predicted to be around 30%, in reality the highest that has been obtained is significantly lower, i.e. $\approx 13\%$. On the other hand, factors that have an influence on low stability are related to technological components. For instance, as a hole transport material, an iodine-based liquid electrolyte is normally used, which is known for its high volatility and affects the design of a cell (it has to be properly encapsulated to prevent leakage). This can consequently lead to the decrease of the operational performance.

For these reasons, research in this thesis was aimed at improving efficiency by employing specifically designed nanomaterials, decorated with other compounds that are known to exhibit favorable properties in photovoltaic performance.

In chapter 2, research focused on a n-type material that is used in the course of device configuration. The purpose of the n-type layer is charge extraction and transfer of the electrons that are generated by a photoactive dye. Normally, TiO₂ NPs are used for that purpose, specifically two layers of different sized NPs. The aim of the first layer is the attachment of dye molecules (small NPs → high BET surface area), while the second layer consists of bigger sized NPs (light-scattering effect). TiO₂ NPs were replaced with an alternative material of TiO₂ NFs, which are 1D nanostructures. As such, they offer direct transport of charge carriers since their morphology does not involve any grain boundaries; the resulting amount of defects is notably lower. Therefore, it was expected that due to the decrease in charge recombination level, J_{sc} will increase, yielding higher efficiency. On the other hand, gold NPs are noble metal nanostructures that possess many favorable characteristics (light-scattering, fluorescence, and facilitation of charge separation and transfer) and have previously been used for solar cells to enhance their efficiency. However, as with many other nanomaterials, their characteristics are size dependent. To combine the advantages of both nanomaterials (NFs and gold NPs) and make a composite containing the superior properties from each one, TiO₂ NFs were used together with gold NPs as a n-type layer for DSSCs. However, as different sized gold NPs do not exhibit the same properties, a size dependent study was performed to investigate their effects on DSSCs. For that purpose, 5, 8, 10, and 12 nm sizes of gold NPs were synthesized and embedded in TiO₂ NFs. Characterisation revealed that NPs were present in NFs in zero oxidation state (metallic gold), and that they did not cause any phase

transformation, since the anatase phase of TiO_2 was observed for all types of samples. In addition, there were no changes in absorbance and the band gap remained the same, independently of the presence of gold NPs. However, when such a composite material was used for DSSCs, a notable difference in the performance was observed, influenced by the size change. Results revealed that the most beneficial size range of gold NPs was 8 nm. Compared to the control devices, efficiency of the DSSCs that included 8 nm gold NPs, increased by 20%. While particular sizes of gold NPs had a detrimental effect on the device's J_{sc} and V_{oc} , they all had higher FF compared to the control. This was attributed to the decrease in R_s as obtained from the J-V curves. Overall, results of this study have revealed that precise control over the size of gold NPs is required when being used for solar photovoltaic technology. If the size is too large, their presence will have a detrimental effect on the efficiency and thus the optimal size should be around 8 nm.

In chapter 3, research was extended towards other types of solar cells. Specifically, in addition to DSSCs, PSCs were fabricated. PSCs are the latest generation of photovoltaic technology, which have, in the last decade, attracted substantial research interest within the photovoltaic community. Their efficiencies were subject to a remarkable increase, especially in the last five years, reaching values at least as high as 20%. While PSCs can offer an ideal combination of low cost and high performance, they suffer from other issues, for instance, poor stability, use of lead, and I-V hysteresis, all of which have influenced the prospects for commercialization. Since they evolved from DSSCs, their device configuration and operation are comparable. Therefore, similarly to chapter 2, TiO_2 NFs were used as a n-type layer, replacing commonly used TiO_2 NPs. As opposed to chapter 2, gold NPs were replaced with lanthanum and lithium ions, which were individually added directly to the precursor

solution for electrospinning, and yielded NFs with metal ions already embedded. Prior to using this material for a device configuration, the NFs were first characterised. It was revealed that the metal ions (lanthanum and lithium) did not cause any substantial doping, since they were present on the surface and did not enter the TiO₂ crystal structure. This was attributed to the large difference in ionic radius when compared with the cation in TiO₂. However, the addition of lithium caused the formation of the rutile phase of TiO₂ at lower temperatures (500 °C), which would otherwise typically take place between 600-800°C. On the other hand, with the addition of lanthanum, no difference in crystal structure compared to the control was observed. Nevertheless, both metal ions influenced the sizes of TiO₂ crystallites. It was determined that the addition of lanthanum ions caused their sizes to be smaller, as opposed to adding lithium ions where the impact was the opposite. Hence, the size of crystallites affected the BET surface area and lanthanum treated TiO₂ NFs exhibited the highest one, even higher than the one measured for P25 NPs. On the other hand, the lowest BET surface area was measured for lithium treated TiO₂ NFs, which can be explained by their large crystallite size. When nanomaterials were used for solar cells, the trends between DSSCs and PSCs did not change. Specifically, photovoltaic parameters revealed that the best performing devices consisted of lanthanum treated TiO₂ NFs, because the main source of the efficiency improvement was high J_{sc}. For PSCs, the improvement was considerable, and the efficiency increased by ≈35% compared with the control. As anticipated, PSCs proved to be better performing and the highest efficiency obtained was 11.5%. In addition, and as already noted for gold NPs, the presence of lanthanum and lithium ions was favorable in terms of FF, which can be associated with the trends of R_{SH}. While the efficiencies reported in this study are far below 20%, the results and materials/device characterisation are of importance, as new fundamental

understanding has been acquired, and the role of lanthanum and lithium has been illustrated for two types of solar cells.

Typically, perovskite materials employed for photovoltaics are in the form of bulk thin films. However, they can also be in the form of QDNCs, which possess particular characteristics that cannot be achieved in bulk. The most relevant properties for solar energy conversion include: a high molar extinction coefficient, the quantum confinement effect, improved thermal stability, and the possibility of multiple exciton generation that can theoretically result in highly efficient solar cells. Therefore, QDNCs can be an appealing choice for a light absorbing material, and as such they have been widely used for solar cells. Moreover, there were reports regarding tandem devices consisting of both perovskite bulk material and QDNCs. Nevertheless, the main applications for QDNCs are based around light emission, for instance, LEDs, since PLQYs can reach values near unity. These materials are generally synthesized via the hot injection approach at elevated temperatures. While synthesis can be performed at RT, such routes mostly employ the use of toxic polar solvents.

In chapter 4, a novel synthesis approach for QDNCs was explored. They were synthesized, (CsPbBr_3 and FAPbBr_3) at RT, in non-polar and industrially feasible solvents, and without the need of an inert environment (oxygen and water vapor free). Ligands (carboxylic acid and amine) were replaced with a phosphine-based alternative (TOPO and DiOPA), which allowed the solvation of lead salt and caesium carbonate without the need for heating. Furthermore, characterisation revealed that both types exhibited a cube-like structure, where RT- FAPbBr_3 QDNCs were notably bigger. The crystal structure was identified as the cubic perovskite type. Their photoluminescence emission peaks were in the green portion of the electromagnetic spectrum and RT- FAPbBr_3 QDNCs featured a particular bathochromic shift in emission, not seen in RT-

CsPbBr₃ QDNCs. The level of color purity was very high, with fwhm values between 14 – 19 nm, which is in line with the range that resulted from synthesis performed at high temperatures. Moreover, in terms of PLQYs, the synthesis performed at RT (using TOPO and DiOPA) is more beneficial, as there is a decrease in the quality and brightness of QDNCs if they are synthesized at elevated temperatures. It was determined that the average PL lifetime of phosphine-capped QDNCs was considerably higher than the control, which was attributed to their bigger sizes. Therefore, they did not show any quantum confinement effects, since the size was reasonably bigger than the exciton Bohr radius. The investigation on the surface ligands and nanocrystal core interactions showed that organic ligands bind via a Pb-O-P bond, and that their P=O group acts as a binding center to attach to the lead element of a perovskite structure. However, the strength of the bond is not very high, and ligands can be easily removed from the NC core after the addition of polar solvents (purification). While this can be advantageous in the use of such materials for optoelectronic applications (i.e. better charge transport), the light emission should not decrease.

Nevertheless, the results discussed in chapter 4 may be helpful for future ligand exchange studies, and investigation into how to manipulate the ligand interactions with the NC core.

5.2 Novel findings

Work discussed in chapters 2 and 3 focused on improving the efficiency of solar cells via nanostructuring, metal addition (ions, NPs), or the combination of both.

While the addition of gold NPs to the n-type layer of DSSCs is known to improve the performance, the influence of the addition on the performance metrics had not been investigated prior to the start of this project. In addition, gold NPs have not been combined yet with TiO₂ NFs to exploit the advantages of both in a composite material (chapter 2).

In chapter 3, novelty can be found in the one-step modification of TiO₂ NFs by the direct addition of lanthanum and lithium ions to the precursor solution, which is a cost effective and industrially feasible approach. Furthermore, characterisation revealed that metal ions did not cause any substantial interstitial or substitutional doping of TiO₂, which has not previously been reported for 1D nanostructures. In addition, results showed that lanthanum treatment influenced the BET surface area of NFs and that the values even exceeded the ones for P25 TiO₂ NPs. Finally, both types of NFs were used for two types of solar cells (DSSCs and PSCs), where it was shown that they influenced the device's performance metrics.

In chapter 4, two types of QDNCs were synthesized for the first time in RT conditions, without the use of polar solvents or the need for an inert atmosphere. To achieve this, phosphine-based ligands were employed instead of carboxylic acids or amines. Surface ligand interactions were investigated, and it was revealed that the Pb-O-P bond was formed, binding ligands to the NC core. Additionally, when syntheses were performed at elevated temperatures this influenced PLQYs, as the values decreased with increasing temperature.

5.3 Future outlooks

The main drawbacks preventing DSSCs being commercially viable are related to low efficiency and poor long-term stability. Future research should therefore focus on developing new dyes with extended absorption profiles that would enable better light harvesting. Since the use of volatile liquid electrolytes is related to long-term stability issues, new alternatives, ideally in a solid-state form, need to be discovered. Furthermore, efficiencies of $\approx 16\%$ must be obtained across large area modules for the technology to be competitive with other alternatives.

In contrast to DSSCs, PSCs were shown to be highly efficient. However, they exhibit significant stability issues that prevent them from becoming an important player on the solar energy market. Once modules with stabilities of ≈ 20 years can be obtained, the technology can notably disrupt the market.

As with PSCs, QDNCs also suffer from stability issues. However, remarkable optoelectronic performance has been illustrated with PLQYs approaching near unity. Nonetheless, due to their highly ionic nature, the emission decreases with time. The stability of bright emitters, particularly LEDs, is currently far from commercial standard. Future research should target ligand alternatives that can bind strongly to the NC core and would not detach over time.

Nanotechnology can play an important role in progressing the field of solar and light display technology. The implementation of nanomaterials has opened the path towards more efficient and stable solar cells. Considering the progress that has been achieved in the last decades, aspirations towards a more sustainable future are promising. The developments presented in this thesis advance the field of photovoltaics by elucidating fundamental properties of nanomaterials that can improve

the PCE of solar cells. Their size limit was optimised where for particular elements it was shown that their effect was detrimental. Contrarily, other candidates proved to be beneficial, which can be helpful for further development of this field.

6. Bibliography

- [1] P. E. Brockway, A. Owen, L. I. Brand-Correa, L. Hardt, *Nat. Energy* **2019**, *4*, 612–621.
- [2] U. K. Rout, K. Akimoto, F. Sano, J. Oda, T. Homma, T. Tomoda, *Energy Policy* **2008**, *36*, 3477–3484.
- [3] C. Dong, X. Dong, Q. Jiang, K. Dong, G. Liu, *Sci. Total Environ.* **2018**, *622–623*, 1294–1303.
- [4] S. Strunz, *Nat. Sustain.* **2018**, *1*, 390–391.
- [5] G. Mete, *Energy Transitions and the Future of Gas in the EU: Subsidise or Decarbonise*, Springer Nature, **2019**.
- [6] R. York, S. E. Bell, *Energy Res. Soc. Sci.* **2019**, *51*, 40–43.
- [7] S. Fedoseeva, R. Zeidan, *Nat. Sustain.* **2018**, *1*, 436–440.
- [8] T. Bradford, *Solar Energy: A BIT of Solar Revolution*, MIT Press, **2014**.
- [9] P. R. Wolfe, *The Solar Generation: Childhood and Adolescence of Terrestrial Photovoltaics*, John Wiley & Sons, **2018**.
- [10] M. Portnoi, P. A. Haigh, T. J. Macdonald, F. Ambroz, I. P. Parkin, I. Darwazeh, I. Papakonstantinou, *Light Sci. Appl.* **2021**, *10*, 3.
- [11] V. V. Quaschnig, *Renewable Energy and Climate Change*, John Wiley & Sons, **2009**.
- [12] G. W. Crabtree, N. S. Lewis, *Phys. Today* **2007**, *60*, 37–42.
- [13] G. Verhoeven, *AARGNEWS* **2017**, *55*, 13–18.
- [14] S. Siddiquee, G. J. H. Melvin, M. M. Rahman, *Nanotechnology: Applications in Energy, Drug and Food*, Springer, **2019**.
- [15] B. O'Regan, M. Grätzel, *Nature* **1991**, *353*, 737–740.
- [16] S. Mathew, A. Yella, P. Gao, R. Humphry-Baker, B. F. E. Curchod, N. Ashari-Astani, I. Tavernelli, U. Rothlisberger, M. K. Nazeeruddin, M. Grätzel, *Nat. Chem.* **2014**, *6*, 242–247.
- [17] Y. Rong, G. Liu, H. Wang, X. Li, H. Han, *Front. Optoelectron.* **2013**, *6*, 359–372.
- [18] S. Mozaffari, M. R. Nateghi, M. B. Zarandi, *Renew. Sustain. Energy Rev.* **2017**, *71*, 675–686.
- [19] R. Singh, G. F. Alapatt, A. Lakhtakia, *IEEE J. Electron Devices Soc.* **2013**, *1*, 129–144.
- [20] M. Berginc, U. O. Krašovec, M. Topič, *Sol. Energy Mater. Sol. Cells* **2014**, *120*, 491–499.
- [21] M. Chen, L.-L. Shao, *Chem. Eng. J.* **2016**, *304*, 629–645.
- [22] I. Benesperi, H. Michaels, M. Freitag, *J. Mater. Chem. C* **2018**, *6*, 11903–11942.
- [23] F. Xie, C.-C. Chen, Y. Wu, X. Li, M. Cai, X. Liu, X. Yang, L. Han, *Energy Environ. Sci.* **2017**, *10*, 1942–1949.
- [24] T. Bu, X. Liu, J. Li, W. Huang, Z. Wu, F. Huang, Y.-B. Cheng, J. Zhong, *Sol. RRL* **2020**, *4*, 1900263.
- [25] L. Meng, J. You, Y. Yang, *Nat. Commun.* **2018**, *9*, 1–4.
- [26] J.-P. Correa-Baena, M. Saliba, T. Buonassisi, M. Grätzel, A. Abate, W. Tress, A. Hagfeldt, *Science* **2017**, *358*, 739–744.
- [27] H. Chen, S. Yang, *Adv. Mater.* **2017**, *29*, 1603994.
- [28] M. I. Asghar, J. Zhang, H. Wang, P. D. Lund, *Renew. Sustain. Energy Rev.* **2017**, *77*, 131–146.
- [29] P. Tyagi, T. W. David, V. D. Stoichkov, J. Kettle, *Sol. Energy* **2019**, *193*, 12–19.
- [30] H. J. Jung, D. Kim, S. Kim, J. Park, V. P. Dravid, B. Shin, *Adv. Mater.* **2018**, *30*, 1802769.
- [31] Y. Yu, P. Zhang, L. Guo, Z. Chen, Q. Wu, Y. Ding, W. Zheng, Y. Cao, *J. Phys. Chem. C* **2014**, *118*, 12727–12733.
- [32] S. Kumar, M. Nehra, A. Deep, D. Kedia, N. Dilbaghi, K.-H. Kim, *Renew. Sustain. Energy Rev.* **2017**, *73*, 821–839.
- [33] S. Li, X. Zhu, B. Wang, Y. Qiao, W. Liu, H. Yang, N. Liu, M. Chen, H. Lu, Y. Yang, *Nanoscale Res. Lett.* **2018**, *13*, 210.
- [34] F. Sordello, G. Zeb, K. Hu, P. Calza, C. Minero, T. Szkopek, M. Cerruti, *Nanoscale* **2014**, *6*, 6710–6719.
- [35] X. Bi, G. Du, A. Kalam, D. Sun, Y. Yu, Q. Su, B. Xu, A. G. Al-Sehemi, *Chem. Eng. Sci.* **2021**, *234*, 116440.

- [36] K. Fan, J. Yu, W. Ho, *Mater. Horiz.* **2017**, *4*, 319–344.
- [37] M. Ge, C. Cao, J. Huang, S. Li, Z. Chen, K.-Q. Zhang, S. S. Al-Deyab, Y. Lai, *J. Mater. Chem. A* **2016**, *4*, 6772–6801.
- [38] P. Joshi, L. Zhang, D. Davoux, Z. Zhu, D. Galipeau, H. Fong, Q. Qiao, *Energy Environ. Sci.* **2010**, *3*, 1507–1510.
- [39] S. A. Kulkarni, S. G. Mhaisalkar, N. Mathews, P. P. Boix, *Small Methods* **2019**, *3*, 1800231.
- [40] N. Wang, W. Liu, Q. Zhang, *Small Methods* **2018**, *2*, 1700380.
- [41] A. Manzi, Y. Tong, J. Feucht, E.-P. Yao, L. Polavarapu, A. S. Urban, J. Feldmann, *Nat. Commun.* **2018**, *9*, 1–6.
- [42] H. Fu, *J. Mater. Chem. A* **2019**, *7*, 14357–14379.
- [43] F. Ambroz, T. J. Macdonald, V. Martis, I. P. Parkin, *Small Methods* **2018**, *2*, 1800173.
- [44] A. M. Alotaibi, S. Sathasivam, B. A. D. Williamson, A. Kafizas, C. Sotelo-Vazquez, A. Taylor, D. O. Scanlon, I. P. Parkin, *Chem. Mater.* **2018**, *30*, 1353–1361.
- [45] A. Fujishima, K. Honda, *Nature* **1972**, *238*, 37.
- [46] M. R. Hoffmann, S. T. Martin, Wonyong. Choi, D. W. Bahnemann, *Chem. Rev.* **1995**, *95*, 69–96.
- [47] M. Grätzel, *Nature* **2001**, *414*, 338.
- [48] J. Tao, T. Luttrell, M. Batzill, *Nat. Chem.* **2011**, *3*, 296–300.
- [49] S. Elmas, F. Ambroz, D. Chugh, T. Nann, *Langmuir* **2016**, *32*, 4952–4958.
- [50] Y. Wang, H. Yang, Y. Liu, H. Wang, H. Shen, J. Yan, H. Xu, *Prog. Photovolt. Res. Appl.* **2010**, *18*, 285–290.
- [51] A. Hagfeldt, G. Boschloo, L. Sun, L. Kloo, H. Pettersson, *Chem. Rev.* **2010**, *110*, 6595–6663.
- [52] A. Kojima, K. Teshima, Y. Shirai, T. Miyasaka, *J. Am. Chem. Soc.* **2009**, *131*, 6050–6051.
- [53] S. Lee, I.-S. Cho, J. H. Lee, D. H. Kim, D. W. Kim, J. Y. Kim, H. Shin, J.-K. Lee, H. S. Jung, N.-G. Park, K. Kim, M. J. Ko, K. S. Hong, *Chem. Mater.* **2010**, *22*, 1958–1965.
- [54] G. K. Mor, K. Shankar, M. Paulose, O. K. Varghese, C. A. Grimes, *Nano Lett.* **2006**, *6*, 215–218.
- [55] T. J. Macdonald, D. D. Tune, M. R. Dewi, C. T. Gibson, J. G. Shapter, T. Nann, *ChemSusChem* **2015**, *8*, 3396–3400.
- [56] J. I. Kim, T. I. Hwang, L. E. Aguilar, C. H. Park, C. S. Kim, *Sci. Rep.* **2016**, *6*, 23761.
- [57] P. Du, L. Song, J. Xiong, N. Li, Z. Xi, L. Wang, D. Jin, S. Guo, Y. Yuan, *Electrochimica Acta* **2012**, *78*, 392–397.
- [58] X. Wang, M. Xi, H. Fong, Z. Zhu, *ACS Appl. Mater. Interfaces* **2014**, *6*, 15925–15932.
- [59] N. M. Tikekar, J. J. Lannutti, *Ceram. Int.* **2012**, *38*, 4057–4064.
- [60] J. Wu, G. Xie, J. Lin, Z. Lan, M. Huang, Y. Huang, *J. Power Sources* **2010**, *195*, 6937–6940.
- [61] S. Muduli, O. Game, V. Dhas, K. Vijayamohanan, K. A. Bogle, N. Valanoor, S. B. Ogale, *Sol. Energy* **2012**, *86*, 1428–1434.
- [62] Q. Wang, T. Butburee, X. Wu, H. Chen, G. Liu, L. Wang, *J. Mater. Chem. A* **2013**, *1*, 13524–13531.
- [63] M. Batmunkh, T. J. Macdonald, W. J. Peveler, A. S. R. Bati, C. J. Carmalt, I. P. Parkin, J. G. Shapter, *ChemSusChem* **2017**, *10*, 3750–3753.
- [64] J. Du, J. Qi, D. Wang, Z. Tang, *Energy Environ. Sci.* **2012**, *5*, 6914–6918.
- [65] M. D. Brown, T. Suteewong, R. S. S. Kumar, V. D’Innocenzo, A. Petrozza, M. M. Lee, U. Wiesner, H. J. Snaith, *Nano Lett.* **2011**, *11*, 438–445.
- [66] H.-Y. Kim, D. H. Song, H. Yoon, J. S. Suh, *RSC Adv.* **2015**, *5*, 27464–27469.
- [67] F. Ambroz, J. L. Donnelly, J. D. Wilden, T. J. Macdonald, I. P. Parkin, *Nanomaterials* **2019**, *9*, 1346.
- [68] C. Yogi, K. Kojima, T. Hashishin, N. Wada, Y. Inada, E. Della Gaspera, M. Bersani, A. Martucci, L. Liu, T.-K. Sham, *J. Phys. Chem. C* **2011**, *115*, 6554–6560.
- [69] W. P. Wuelfing, S. M. Gross, D. T. Miles, R. W. Murray, *J. Am. Chem. Soc.* **1998**, *120*, 12696–12697.
- [70] I. Hussain, S. Graham, Z. Wang, B. Tan, D. C. Sherrington, S. P. Rannard, A. I. Cooper, M. Brust, *J. Am. Chem. Soc.* **2005**, *127*, 16398–16399.
- [71] T. J. Macdonald, K. Wu, S. K. Sehmi, S. Noimark, W. J. Peveler, H. du Toit, N. H. Voelcker, E. Allan, A. J. MacRobert, A. Gavrilidis, I. P. Parkin, *Sci. Rep.* **2016**, *6*, 39272.

- [72] J. Piella, N. G. Bastús, V. Puntès, *Chem. Mater.* **2016**, *28*, 1066–1075.
- [73] T. J. Macdonald, F. Ambroz, M. Batmunkh, Y. Li, D. Kim, C. Contini, R. Poduval, H. Liu, J. G. Shapter, I. Papakonstantinou, I. P. Parkin, *Mater. Today Energy* **2018**, *9*, 254–263.
- [74] R. Torres-Mendieta, D. Ventura-Espinosa, S. Sabater, J. Lancis, G. Mínguez-Vega, J. A. Mata, *Sci. Rep.* **2016**, *6*, 30478.
- [75] M. P. Casaletto, A. Longo, A. Martorana, A. Prestianni, A. M. Venezia, *Surf. Interface Anal.* **2006**, *38*, 215–218.
- [76] H. Li, Z. Bian, J. Zhu, Y. Huo, H. Li, Y. Lu, *J. Am. Chem. Soc.* **2007**, *129*, 4538–4539.
- [77] G. Cheng, F. Xu, F. J. Stadler, R. Chen, *RSC Adv.* **2015**, *5*, 64293–64298.
- [78] J. Xu, K. Wang, S.-Z. Zu, B.-H. Han, Z. Wei, *ACS Nano* **2010**, *4*, 5019–5026.
- [79] Y. Li, H. Wang, Q. Feng, G. Zhou, Z.-S. Wang, *Energy Environ. Sci.* **2013**, *6*, 2156–2165.
- [80] R. A. Naphade, M. Tathavadekar, J. P. Jog, S. Agarkar, S. Ogale, *J. Mater. Chem. A* **2013**, *2*, 975–984.
- [81] P. Zhu, A. S. Nair, S. Yang, S. Peng, S. Ramakrishna, *J. Mater. Chem.* **2011**, *21*, 12210–12212.
- [82] S. Borbón, S. Lugo, D. Pourjafari, N. Pineda Aguilar, G. Oskam, I. López, *ACS Omega* **2020**, *5*, 10977–10986.
- [83] S. Chang, Q. Li, X. Xiao, K. Y. Wong, T. Chen, *Energy Environ. Sci.* **2012**, *5*, 9444–9448.
- [84] B. Hvolbæk, T. V. W. Janssens, B. S. Clausen, H. Falsig, C. H. Christensen, J. K. Nørskov, *Nano Today* **2007**, *2*, 14–18.
- [85] R. Jin, S. Sun, Y. Yang, Y. Xing, D. Yu, X. Yu, S. Song, *Dalton Trans.* **2013**, *42*, 7888–7893.
- [86] S. Chuangchote, T. Sagawa, S. Yoshikawa, *Appl. Phys. Lett.* **2008**, *93*, 033310.
- [87] Y. Lu, S. Sathasivam, J. Song, C. R. Crick, C. J. Carmalt, I. P. Parkin, *Science* **2015**, *347*, 1132–1135.
- [88] X. Lu, G. Wang, T. Zhai, M. Yu, J. Gan, Y. Tong, Y. Li, *Nano Lett.* **2012**, *12*, 1690–1696.
- [89] F. Ambroz, T. J. Macdonald, T. Nann, *Adv. Energy Mater.* **2017**, *7*, 1602093.
- [90] B. Roose, S. Pathak, U. Steiner, *Chem. Soc. Rev.* **2015**, *44*, 8326–8349.
- [91] X. Liu, J. Iocozzia, Y. Wang, X. Cui, Y. Chen, S. Zhao, Z. Li, Z. Lin, *Energy Environ. Sci.* **2017**, *10*, 402–434.
- [92] I. K. Konstantinou, T. A. Albanis, *Appl. Catal. B Environ.* **2004**, *49*, 1–14.
- [93] L. Yang, W. W.-F. Leung, *Adv. Mater.* **2011**, *23*, 4559–4562.
- [94] S. Cavaliere, S. Subianto, I. Savych, D. J. Jones, J. Rozière, *Energy Environ. Sci.* **2011**, *4*, 4761–4785.
- [95] F. Ambroz, S. Sathasivam, R. Lee, S. Gadipelli, C.-T. Lin, S. Xu, R. K. Poduval, M. A. McLachlan, I. Papakonstantinou, I. P. Parkin, T. J. Macdonald, *ChemElectroChem* **2019**, *6*, 3529–3529.
- [96] J. Liqiang, S. Xiaojun, X. Baifu, W. Baiqi, C. Weimin, F. Honggang, *J. Solid State Chem.* **2004**, *177*, 3375–3382.
- [97] J. Zhang, Z. Zhao, X. Wang, T. Yu, J. Guan, Z. Yu, Z. Li, Z. Zou, *J. Phys. Chem. C* **2010**, *114*, 18396–18400.
- [98] F. Giordano, A. Abate, J. P. C. Baena, M. Saliba, T. Matsui, S. H. Im, S. M. Zakeeruddin, M. K. Nazeeruddin, A. Hagfeldt, M. Graetzel, *Nat. Commun.* **2016**, *7*, 1–6.
- [99] M. M. Lee, J. Teuscher, T. Miyasaka, T. N. Murakami, H. J. Snaith, *Science* **2012**, *338*, 643–647.
- [100] X. Yu, T. J. Marks, A. Facchetti, *Nat. Mater.* **2016**, *15*, 383–396.
- [101] S. Dharani, H. K. Mulmudi, N. Yantara, P. T. T. Trang, N. G. Park, M. Graetzel, S. Mhaisalkar, N. Mathews, P. P. Boix, *Nanoscale* **2014**, *6*, 1675–1679.
- [102] Y. Xiao, G. Han, Y. Li, M. Li, J. Wu, *J. Mater. Chem. A* **2014**, *2*, 16856–16862.
- [103] S. S. Mali, C. S. Shim, H. Kim, P. S. Patil, C. K. Hong, *Nanoscale* **2016**, *8*, 2664–2677.
- [104] M. Batmunkh, T. J. Macdonald, C. J. Shearer, M. Bat-Erdene, Y. Wang, M. J. Biggs, I. P. Parkin, T. Nann, J. G. Shapter, *Adv. Sci.* **2017**, *4*, 1600504.
- [105] T. J. Macdonald, M. Batmunkh, C.-T. Lin, J. Kim, D. D. Tune, F. Ambroz, X. Li, S. Xu, C. Sol, I. Papakonstantinou, M. A. McLachlan, I. P. Parkin, J. G. Shapter, J. R. Durrant, *Small Methods* **2019**, *3*, 1900164.

- [106] N. Ahn, D.-Y. Son, I.-H. Jang, S. M. Kang, M. Choi, N.-G. Park, *J. Am. Chem. Soc.* **2015**, *137*, 8696–8699.
- [107] Y.-T. Ma, S.-D. Li, *J. Chin. Chem. Soc.* **2015**, *62*, 380–384.
- [108] H. Hou, M. Shang, L. Wang, W. Li, B. Tang, W. Yang, *Sci. Rep.* **2015**, *5*, 15228.
- [109] A. R. Tanyi, A. I. Rafieh, P. Ekaneyaka, A. L. Tan, D. J. Young, Z. Zheng, V. Chellappan, G. S. Subramanian, R. L. N. Chandrakanthi, *Electrochimica Acta* **2015**, *178*, 240–248.
- [110] Y. Zhou, C. Chen, N. Wang, Y. Li, H. Ding, *J. Phys. Chem. C* **2016**, *120*, 6116–6124.
- [111] K. P. Priyanka, V. R. Revathy, P. Rosmin, B. Thrivedu, K. M. Elsa, J. Nimmymol, K. M. Balakrishna, T. Varghese, *Mater. Charact.* **2016**, *113*, 144–151.
- [112] F. Rossella, P. Galinetto, M. C. Mozzati, L. Malavasi, Y. D. Fernandez, G. Drera, L. Sangaletti, *J. Raman Spectrosc.* **2010**, *41*, 558–565.
- [113] T. Umabayashi, T. Yamaki, H. Itoh, K. Asai, *Appl. Phys. Lett.* **2002**, *81*, 454–456.
- [114] D. Reyes-Coronado, G. Rodríguez-Gattorno, M. E. Espinosa-Pesqueira, C. Cab, R. de Coss, G. Oskam, *Nanotechnology* **2008**, *19*, 145605.
- [115] A. Kumar, R. Jose, K. Fujihara, J. Wang, S. Ramakrishna, *Chem. Mater.* **2007**, *19*, 6536–6542.
- [116] M. Motlak, N. A. M. Barakat, M. S. Akhtar, A. G. El-Deen, M. Obaid, C. S. Kim, K. A. Khalil, A. A. Almajid, *Chem. Eng. J.* **2015**, *268*, 153–161.
- [117] H. Imahori, S. Hayashi, T. Umeyama, S. Eu, A. Oguro, S. Kang, Y. Matano, T. Shishido, S. Ngamsinlapasathian, S. Yoshikawa, *Langmuir* **2006**, *22*, 11405–11411.
- [118] S. Gadipelli, W. Travis, W. Zhou, Z. Guo, *Energy Environ. Sci.* **2014**, *7*, 2232–2238.
- [119] S. Gadipelli, Z. X. Guo, *ChemSusChem* **2015**, *8*, 2123–2132.
- [120] S. Ito, T. N. Murakami, P. Comte, P. Liska, C. Grätzel, M. K. Nazeeruddin, M. Grätzel, *Thin Solid Films* **2008**, *516*, 4613–4619.
- [121] A. Subramanian, J.-S. Bow, H.-W. Wang, *Thin Solid Films* **2012**, *520*, 7011–7017.
- [122] I. Ivanova, T. A. Kandiel, Y.-J. Cho, W. Choi, D. Bahnemann, *ACS Catal.* **2018**, *8*, 2313–2325.
- [123] B. Qi, J. Wang, *Phys. Chem. Chem. Phys.* **2013**, *15*, 8972–8982.
- [124] Y. Guo, H. Liu, W. Li, L. Zhu, H. Chen, *Sol. RRL* **2020**, *4*, 2000380.
- [125] W. Nie, H. Tsai, R. Asadpour, J.-C. Blancon, A. J. Neukirch, G. Gupta, J. J. Crochet, M. Chhowalla, S. Tretiak, M. A. Alam, H.-L. Wang, A. D. Mohite, *Science* **2015**, *347*, 522–525.
- [126] H. Li, B. Zheng, Y. Xue, S. Liu, C. Gao, X. Liu, *Sol. Energy Mater. Sol. Cells* **2017**, *168*, 85–90.
- [127] M. A. Green, A. Ho-Baillie, H. J. Snaith, *Nat. Photonics* **2014**, *8*, 506–514.
- [128] X. Wang, S. Karanjit, L. Zhang, H. Fong, Q. Qiao, Z. Zhu, *Appl. Phys. Lett.* **2011**, *98*, 082114.
- [129] A. A. Madhavan, S. Kalluri, D. K. Chacko, T. A. Arun, S. Nagarajan, K. R. V. Subramanian, A. S. Nair, S. V. Nair, A. Balakrishnan, *RSC Adv.* **2012**, *2*, 13032–13037.
- [130] J. H. Heo, M. S. You, M. H. Chang, W. Yin, T. K. Ahn, S.-J. Lee, S.-J. Sung, D. H. Kim, S. H. Im, *Nano Energy* **2015**, *15*, 530–539.
- [131] S. Wang, Z. Huang, X. Wang, Y. Li, M. Günther, S. Valenzuela, P. Parikh, A. Cabrerros, W. Xiong, Y. S. Meng, *J. Am. Chem. Soc.* **2018**, *140*, 16720–16730.
- [132] S. Mabrouk, B. Bahrami, A. Gurung, K. M. Reza, N. Adhikari, A. Dubey, R. Pathak, S. Yang, Q. Qiao, *Sustain. Energy Fuels* **2017**, *1*, 2162–2171.
- [133] D. Liu, S. Li, P. Zhang, Y. Wang, R. Zhang, H. Sarvari, F. Wang, J. Wu, Z. Wang, Z. D. Chen, *Nano Energy* **2017**, *31*, 462–468.
- [134] C. Lan, J. Luo, H. Lan, B. Fan, H. Peng, J. Zhao, H. Sun, Z. Zheng, G. Liang, P. Fan, *Materials* **2018**, *11*, 355.
- [135] M. Nada, T. Gonda, Q. Shen, H. Shimada, T. Toyoda, N. Kobayashi, *Jpn. J. Appl. Phys.* **2009**, *48*, 025505.
- [136] J. R. Jennings, Q. Wang, *J. Phys. Chem. C* **2010**, *114*, 1715–1724.
- [137] N.-G. Park, K. Zhu, *Nat. Rev. Mater.* **2020**, *5*, 333–350.
- [138] F. Enrichi, G. Righini, *Solar Cells and Light Management: Materials, Strategies and Sustainability*, Elsevier, **2019**.
- [139] M. Liu, M. B. Johnston, H. J. Snaith, *Nature* **2013**, *501*, 395–398.

- [140] Y. Fu, H. Zhu, J. Chen, M. P. Hautzinger, X.-Y. Zhu, S. Jin, *Nat. Rev. Mater.* **2019**, *4*, 169–188.
- [141] A. K. Jena, A. Kulkarni, T. Miyasaka, *Chem. Rev.* **2019**, *119*, 3036–3103.
- [142] Y. Zhang, A. Kirs, F. Ambroz, C.-T. Lin, A. S. R. Bati, I. P. Parkin, J. G. Shapter, M. Batmunkh, T. J. Macdonald, *Small Methods* **2020**, 2000744.
- [143] H. Kim, L. Zhao, J. S. Price, A. J. Grede, K. Roh, A. N. Brigeman, M. Lopez, B. P. Rand, N. C. Giebink, *Nat. Commun.* **2018**, *9*, 1–9.
- [144] M. Zhang, F. Zhang, Y. Wang, L. Zhu, Y. Hu, Z. Lou, Y. Hou, F. Teng, *Sci. Rep.* **2018**, *8*, 1–9.
- [145] M. Capdevila-Cortada, *Nat. Catal.* **2018**, *1*, 737–737.
- [146] Y. Mi, Y. Zhong, Q. Zhang, X. Liu, *Adv. Opt. Mater.* **2019**, *7*, 1900544.
- [147] M. Abdi-Jalebi, Z. Andaji-Garmaroudi, S. Cacovich, C. Stavrakas, B. Philippe, J. M. Richter, M. Alsari, E. P. Booker, E. M. Hutter, A. J. Pearson, S. Lilliu, T. J. Savenije, H. Rensmo, G. Divitini, C. Ducati, R. H. Friend, S. D. Stranks, *Nature* **2018**, *555*, 497–501.
- [148] Q. Shan, J. Song, Y. Zou, J. Li, L. Xu, J. Xue, Y. Dong, B. Han, J. Chen, H. Zeng, *Small* **2017**, *13*, 1701770.
- [149] A. Dutta, R. K. Behera, P. Pal, S. Baitalik, N. Pradhan, *Angew. Chem. Int. Ed.* **2019**, *58*, 5552–5556.
- [150] L. C. Schmidt, A. Pertegás, S. González-Carrero, O. Malinkiewicz, S. Agouram, G. Mínguez Espallargas, H. J. Bolink, R. E. Galian, J. Pérez-Prieto, *J. Am. Chem. Soc.* **2014**, *136*, 850–853.
- [151] L. Protesescu, S. Yakunin, M. I. Bodnarchuk, F. Krieg, R. Caputo, C. H. Hendon, R. X. Yang, A. Walsh, M. V. Kovalenko, *Nano Lett.* **2015**, *15*, 3692–3696.
- [152] H. Yang, Y. Zhang, K. Hills-Kimball, Y. Zhou, O. Chen, *Sustain. Energy Fuels* **2018**, *2*, 2381–2397.
- [153] J. Butkus, P. Vashishtha, K. Chen, J. K. Gallaher, S. K. K. Prasad, D. Z. Metin, G. Laufersky, N. Gaston, J. E. Halpert, J. M. Hodgkiss, *Chem. Mater.* **2017**, *29*, 3644–3652.
- [154] J. Shamsi, A. S. Urban, M. Imran, L. De Trizio, L. Manna, *Chem. Rev.* **2019**, *119*, 3296–3348.
- [155] S. E. Creutz, E. N. Crites, M. C. De Siena, D. R. Gamelin, *Chem. Mater.* **2018**, *30*, 4887–4891.
- [156] M. Li, R. Begum, J. Fu, Q. Xu, T. M. Koh, S. A. Veldhuis, M. Grätzel, N. Mathews, S. Mhaisalkar, T. C. Sum, *Nat. Commun.* **2018**, *9*, 1–7.
- [157] A. Swarnkar, A. R. Marshall, E. M. Sanehira, B. D. Chernomordik, D. T. Moore, J. A. Christians, T. Chakrabarti, J. M. Luther, *Science* **2016**, *354*, 92–95.
- [158] Y. Shirasaki, G. J. Supran, M. G. Bawendi, V. Bulović, *Nat. Photonics* **2013**, *7*, 13–23.
- [159] S. Seth, T. Ahmed, A. De, A. Samanta, *ACS Energy Lett.* **2019**, *4*, 1610–1618.
- [160] H. Huang, M. I. Bodnarchuk, S. V. Kershaw, M. V. Kovalenko, A. L. Rogach, *ACS Energy Lett.* **2017**, *2*, 2071–2083.
- [161] F. Ambroz, W. Xu, S. Gadipelli, D. J. L. Brett, C.-T. Lin, C. Contini, M. A. McLachlan, J. R. Durrant, I. P. Parkin, T. J. Macdonald, *Part. Part. Syst. Charact.* **2020**, *37*, 1900391.
- [162] D. Yang, M. Cao, Q. Zhong, P. Li, X. Zhang, Q. Zhang, *J. Mater. Chem. C* **2019**, *7*, 757–789.
- [163] Y.-F. Li, J. Feng, H.-B. Sun, *Nanoscale* **2019**, *11*, 19119–19139.
- [164] F. Zhang, S. Huang, P. Wang, X. Chen, S. Zhao, Y. Dong, H. Zhong, *Chem. Mater.* **2017**, *29*, 3793–3799.
- [165] S. Wei, Y. Yang, X. Kang, L. Wang, L. Huang, D. Pan, *Chem. Commun.* **2016**, *52*, 7265–7268.
- [166] O. Vybornyi, S. Yakunin, M. V. Kovalenko, *Nanoscale* **2016**, *8*, 6278–6283.
- [167] D. Yu, F. Cao, Y. Gao, Y. Xiong, H. Zeng, *Adv. Funct. Mater.* **2018**, *28*, 1800248.
- [168] E. Yassitepe, Z. Yang, O. Voznyy, Y. Kim, G. Walters, J. A. Castañeda, P. Kanjanaboos, M. Yuan, X. Gong, F. Fan, J. Pan, S. Hoogland, R. Comin, O. M. Bakr, L. A. Padilha, A. F. Nogueira, E. H. Sargent, *Adv. Funct. Mater.* **2016**, *26*, 8757–8763.
- [169] Y. Dong, Y. Zhao, S. Zhang, Y. Dai, L. Liu, Y. Li, Q. Chen, *J. Mater. Chem. A* **2018**, *6*, 21729–21746.
- [170] L. Protesescu, S. Yakunin, M. I. Bodnarchuk, F. Bertolotti, N. Masciocchi, A. Guagliardi, M. V. Kovalenko, *J. Am. Chem. Soc.* **2016**, *138*, 14202–14205.
- [171] D. J. Norris, M. G. Bawendi, *Phys. Rev. B* **1996**, *53*, 16338–16346.

- [172] A. I. Ekimov, F. Hache, M. C. Schanne-Klein, D. Ricard, C. Flytzanis, I. A. Kudryavtsev, T. V. Yazeva, A. V. Rodina, A. L. Efros, *JOSA B* **1993**, *10*, 100–107.
- [173] O. Chen, J. Zhao, V. P. Chauhan, J. Cui, C. Wong, D. K. Harris, H. Wei, H.-S. Han, D. Fukumura, R. K. Jain, M. G. Bawendi, *Nat. Mater.* **2013**, *12*, 445–451.
- [174] R. Zhu, Z. Luo, H. Chen, Y. Dong, S.-T. Wu, *Opt. Express* **2015**, *23*, 23680–23693.
- [175] R. Parker, *Quantum Confinement: Effects, Observations and Insights*, Nova Science Publishers, Incorporated, **2017**.
- [176] A. Dutta, S. K. Dutta, S. Das Adhikari, N. Pradhan, *ACS Energy Lett.* **2018**, *3*, 329–334.
- [177] G. Almeida, O. J. Ashton, L. Goldoni, D. Maggioni, U. Petralanda, N. Mishra, Q. A. Akkerman, I. Infante, H. J. Snaith, L. Manna, *J. Am. Chem. Soc.* **2018**, *140*, 14878–14886.
- [178] Y. Zu, J. Dai, L. Li, F. Yuan, X. Chen, Z. Feng, K. Li, X. Song, F. Yun, Y. Yu, B. Jiao, H. Dong, X. Hou, M. Ju, Z. Wu, *J. Mater. Chem. A* **2019**, *7*, 26116–26122.
- [179] H. R. Moon, J. J. Urban, D. J. Milliron, *Angew. Chem. Int. Ed.* **2009**, *48*, 6278–6281.
- [180] V. K. Ravi, A. Swarnkar, R. Chakraborty, A. Nag, *Nanotechnology* **2016**, *27*, 325708.
- [181] D. N. Minh, J. Kim, J. Hyon, J. H. Sim, H. H. Sowlih, C. Seo, J. Nam, S. Eom, S. Suk, S. Lee, E. Kim, Y. Kang, *Chem. Mater.* **2017**, *29*, 5713–5719.
- [182] B. Tian, B. Tian, B. Smith, M. Scott, Q. Lei, R. Hua, Y. Tian, Y. Liu, *Proc. Natl. Acad. Sci.* **2018**, *115*, 201800069.
- [183] H. S. Liu, T. S. Chin, S. W. Yung, *Mater. Chem. Phys.* **1997**, *50*, 1–10.
- [184] A. G. Young, N. Al-Salim, D. P. Green, A. J. McQuillan, *Langmuir* **2008**, *24*, 3841–3849.
- [185] J. K. Lorenz, A. B. Ellis, *J. Am. Chem. Soc.* **1998**, *120*, 10970–10975.
- [186] N. Al-Salim, A. G. Young, R. D. Tilley, A. J. McQuillan, J. Xia, *Chem. Mater.* **2007**, *19*, 5185–5193.
- [187] J. E. B. Katari, V. L. Colvin, A. P. Alivisatos, *J. Phys. Chem.* **1994**, *98*, 4109–4117.
- [188] J. R. D. la Rosa, P. Elizondo-Martínez, B. N. Martínez, N. P. Rodríguez, J. R. Díaz, *Mater. Manuf. Process.* **2011**, *26*, 304–310.
- [189] K. Hills-Kimball, Y. Nagaoka, C. Cao, E. Chaykovsky, O. Chen, *J. Mater. Chem. C* **2017**, *5*, 5680–5684.
- [190] V. C. A. Taylor, D. Tiwari, M. Duchi, P. M. Donaldson, I. P. Clark, D. J. Fermin, T. A. A. Oliver, *J. Phys. Chem. Lett.* **2018**, *9*, 895–901.
- [191] L. Dimesso, A. Quintilla, Y.-M. Kim, U. Lemmer, W. Jaegermann, *Mater. Sci. Eng. B* **2016**, *204*, 27–33.

7. Supporting Information

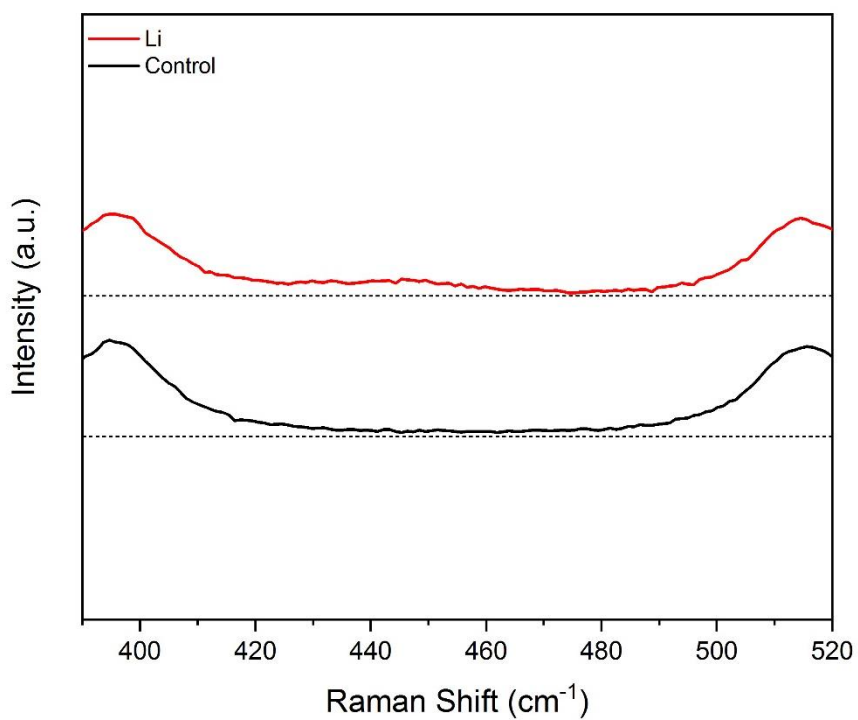


Figure S11. Inset of the Raman spectra between 390 - 520 cm⁻¹ for lithium (red) and control (black) TiO₂ NFs.